Università degli Studi di Padova

Department of Industrial Engineering

Master Thesis in Aerospace Engineering

Aeroacoustics of maneuvering drones

Supervisor
Prof. De Vanna Francesco
Università degli Studi di Padova

Advisors
Prof. Christope Schram
Dr. Alessandro Zarri, Dr. Julien Christophe
The von Karman Institute for Fluid Dynamics

Master Candidate
Filippo Peron

Student ID
2039057

Academic Year
2022-2023

von Karman Institute for Fluid Dynamics
Sint-Genesius-Rode Belgium

Short Training Program Report

Aeroacousitcs investigation of a maneuvering drone

Filippo Peron

Supervisors
Prof. Christope Schram
Dr. Alessandro Zarri
Dr. Julien Christope

Abstract

In recent years, UAVs have gained interest across applications from e-commerce to search and rescue missions. However, their noise generation is still one of their main limits. While existing research mainly focuses on aeroacoustic noise during forward flight or hovering, the annoyance importance of transition maneuvers for humans is recognized.

This thesis presents a numerical methodology using Simcenter StarCCM+ to study aeroacoustic in maneuvering drones, specifically the transition from hovering to forward flight. The methodology starts with isolated propeller fluid dynamics, extending to the full drone after validation. An analytical model is used to validate propeller thrust variation due to a lack of material in literature.
The overset mesh method is crucial due to the problem's nature. This research dedicates a relevant portion to the mesh approach's peculiarities.
The study continues with the acoustic analysis. Acoustic pressure evaluation employs a time domain solution of FW-H equations with an impermeable surface approach. This investigation focused on the isolated propeller due to time constraints. Defining the maneuver has been challenging thus, a detailed analysis is required for real-case maneuver implementation.

Comparing thrust history graphs for the isolated propeller and full case reveals distinct behavior. Additionally, SPL variation during the isolated propeller's maneuver is observed.

Contents

Listing of figures

Listing of tables

Listing of acronyms

UAVs . . . . . Unmanned Aerial Vehicles

UAM . . . . . Urban air Mobility

SPL . . . . . Sound Pressure Levels

BPF . . . . . Blade Passing Frequency

BEM . . . . . Blade Element Method

BS . . . . . Base Size

CAA . . . . . Computational AeroAcoustic

CCW . . . . . Counterclockwise

CW . . . . . Clockwise

CFD . . . . . Computational Fluid Dynamics

DNS . . . . . Direct Numerical Simulation

FFT . . . . . Fast Fourier Transform

LES . . . . . Large Eddy Simulation

PSD . . . . . Power Spectral Density

RANS . . . . . Reynolds-Averaged Navier–Stokes

RBM . . . . . Rigid Body Motion

TKE . . . . . Turbulent Kinetic Energy

uRANS . . . . . unsteady Reynolds-Averaged Navier–Stokes

Listing of symbols

c . . . . . Speed of sound

B . . . . . blade number

D . . . . . Doppler factor

e_t . . . . . total energy

G(·) . . . . . Green's function

h . . . . . enthalpy

k . . . . . specific turbulence kinetic energy

M . . . . . Mach number

Mr . . . . . source Mach number

N . . . . . rotor speed

p . . . . . pressure

p' . . . . . acoustic pressure fluctuation

q . . . . . heat flux

R . . . . . source-observer distance

r . . . . . receiver radial position

Re . . . . . Reynolds number

s . . . . . entropy

T . . . . . temperature

T_{ij} . . . . . Lighthill stress tensor

v . . . . . velocity

x . . . . . observer distance

$\mathbf{y}$ . . . . . source distance

μ . . . . . dynamic viscosity

ρ . . . . . density

τ . . . . . retarded time

1 Introduction

In recent years we are facing continuous and remarkable growth in the use of UAVs. The choice of such devices is mainly related to their ability to vertically take off and maintain a hovering position. These vehicles are supposed to reduce air pollution and traffic congestion deriving from a more traditional approach towards urban mobility. For all these reasons drones may be employed in different working environments and conditions such as military applications, construction, medical filed as well as search and find missions or delivery applications [6]. All these applications require a careful design to guarantee reduced take-off and landing areas along with noise reduction [7]. The first problem has been solved with the use of vehicles able to vertically take off as mentioned before [8]. On the other hand, the noise pollution phenomenon for propeller-driven vehicles is mainly caused by both propulsion engines and propellers. The propulsion noise source can be easily avoided by operating with electric motors [9]. By contrast, the second source of noise is still the subject of studies and research.

Multiple efforts have been applied in order to reduce the noise pollution because this is still one of the main concerns related to a extensive diffusion of UAVs in residential areas [10]. The aeroacoustics characterization of a propeller can be divided into two main components: Tone noise and Broadband noise. The former is due to the variation of the aerodynamic loads caused by sources that repeat constantly over time. The latter is related to random variation caused by turbulence. Usually, the broadband noise is less annoying thus relevant efforts in the research is focused on tonal noise modeling

and characterization. A lot of studies have been conducted on drones or single propeller in hovering configuration. On the other hand, noise associated to a maneuvering or a transition from hovering to forward flight still needs to be tackled. However, it has been measured that maneuvers and transition of drones are responsible for higher annoyance level with respect to hovering [11].

There have been a number of studies aimed at describing both numerically and experimentally the effects of the forward motion of a single propeller on aeroacoustics. In addition, there have been experimental results concerning the transition from hovering to forward flight of a single propeller. Nevertheless, there is an absence of a numerical methodology that simulates the aeroacoustics of a complete drone in the overall process from hovering to a maneuver configuration. To simulate such a phenomenon from a numerical point of view it is necessary to accurately describe the motion of the propeller/-drone during the process. In numerical simulations of moving bodies it has often been applied the overset mesh approach [12, 13, 14]. Indeed, with this method, it is possible to describe the rotation, attitude change, and translation of the propeller/drone. On the other hand, using a more classical sliding mesh approach it is not possible to describe these three rigid body motions.

Usually, an aeroacoustics simulation of periodic loads consists of two main steps. First, it is necessary to obtain the aerodynamic forces present on the desired surface or body. Secondly, the forces obtained are used to simulate the acoustic propagation of pressure waves [15, 16]. This approach is accounting for the influence that the flow has on the sound propagation, but not the opposite effect. Indeed, these two mechanisms have been decoupled. However, this characteristic is not limiting the simulation for most of the applications [17].

1.1 Research questions

The present work is intended to answer the following questions that arise from the transition description of a drone:

- Is it possible to create a methodology to numerically simulate the transition from hovering to forward flight of a single propeller or a complete drone?
- What are the driving phenomena responsible for the noise of a maneuvering propeller?

- How is it possible to handle the transient from an acoustic point of view?

1.2 Research objective

The objective of this research is to create a methodology able to answer to the above mentioned questions. Therefore, it is intended to simulate the transition from hovering to forward flight in the case of a single propeller and ideally of a complete drone. Eventually, the final objective is to create a methodology for the acoustic analysis of maneuvering propellers.

2

Theoretical Background on Sound

In this chapter, the theoretical background concerning aeroacoustics will be presented. Initially, there will be a very quick introduction to the governing equation of the flow. This will be followed by a more precise description of the different approaches for aeroacoustics handling. In the end, there will be a detailed analysis of the current literature concerning the aeroacoustics analysis of maneuvering propellers. In this way it will be easier to understand the objective of the thesis. A final remark is necessary, in this whole chapter the workflow and the notations used in the book [1] will be followed if not otherwise specified.

2.1 Governing equations

The governing equations of a fluid flow are the Navier-Stokes equations [1]. They are obtained from the conservation of mass, momentum, and energy. Indeed, it is possible to

write the three equations as follows [1]:

$$\frac{\partial \rho}{\partial t} + \frac{\partial (\rho u_j)}{\partial x_j} = 0 \tag{2.1}$$

$$\frac{\partial \rho u_i}{\partial t} + \frac{\partial (\rho u_i u_j + p\delta_{ij} - \tau_{ij})}{\partial x_j} = f_i \tag{2.2}$$

$$\frac{\partial \rho e_t}{\partial t} + \frac{\partial (\rho u_j e_t + p u_j + q_j - u_i \tau_{ij})}{\partial x_j} = 0 \tag{2.3}$$

With $i,j = 1,2,3$. In this way, $\mathbf{v} = (u_1, u_2, u_3)$, ρ is the density p the pressure, e_t is the total energy, q the heat flux, τ the stress tensor and f the body forces.
In order to complete the equations above mentioned it is necessary to define the stress tensor and the heat flux:

1. The stress tensor can be written as:

$$\tau_{ij} = \mu \left(\frac{\partial u_j}{\partial x_i} + \frac{\partial u_i}{\partial x_j} \right) - \frac{1}{3} \frac{\partial u_k}{\partial x_k} \delta_{ij} \tag{2.4}$$

2. The heat flux can be expressed as:

$$q_j = -\kappa \left(\frac{\partial T}{\partial x_j} \right) \tag{2.5}$$

where, μ is the dynamic viscosity, while, κ is the thermal conductivity of the fluid. In order to obtain the Navier-Stokes equation it is necessary to substitute (2.4) into (2.2) and obtain:

$$\frac{D\rho u_i}{Dt} = -\frac{\partial p}{\partial x_j} + \left[\mu \left(\frac{\partial u_j}{\partial x_i} + \frac{\partial u_i}{\partial x_j} \right) - \frac{1}{3} \frac{\partial u_k}{\partial x_k} \delta_{ij} \right] + f_i \tag{2.6}$$

At this point, the governing equations of a flow are (2.6), (2.1) and (2.3). These are commonly referred to as Navier-Stokes equations. It is clear that there are six unknowns and five equations. Therefore, in order to close the set of equations it is necessary to introduce the ideal gas equation:

$$p = \rho R T \tag{2.7}$$

In this way it is possible to have a closed system of PDEs.

2.2 Linear acoustics

In order to study linear acoustics, it is possible to follow different literature sources. In this thesis it has been used the book by Glegg and W. Devenport [1].

2.2.1 The acoustic wave equation

Let us consider a flow in which there is no relevant mean flow [1]. Furthermore, assume the sound propagates isentropically and the perturbations of density are very small compared to the mean value. Finally, it is possible to write [1] :

$$p(x_i,t) = p_0 + p'(x_i,t) \tag{2.8}$$

$$\rho(x_i,t) = \rho_0 + \rho'(x_i,t) \tag{2.9}$$

$$u_i(x_i,t) = u_0 + u'(x_i,t) = u'(x_i,t) = v(x_i,t) \tag{2.10}$$

The last change of variable has been made for a simpler treatment of the terms. Subsequently, considering $\rho' \ll \rho_0$ where ρ_0 is constant in time and along the medium. Therefore, substituting equations (2.8), (2.10), (2.9) into the conservation equations and neglecting viscous stresses [1], it is possible to obtain:

$$\frac{\partial \rho'}{\partial t} + \rho_0 \frac{\partial v_i}{\partial x_i} = 0 \tag{2.11}$$

$$\rho_0 \frac{\partial v_i}{\partial t} + \frac{\partial (p_0 + p')}{\partial x_i} + \rho_0 \frac{\partial v_i v_j}{\partial x_j} = 0 \tag{2.12}$$

Continuing to manipulate the equation (2.12) it is possible to obtain a more compact form. Moreover, if the velocity of the perturbations is small compared to the speed of sound then (2.12) becomes [1]:

$$\rho_0 \frac{\partial v_i}{\partial t} + \frac{\partial p'}{\partial x_i} = 0 \tag{2.13}$$

The hypotheses introduced above is not limiting the validity of the equation [1]. In order to arrive at the final wave equation it is possible to derive in time equation (2.11) and subtract (2.13). The final result is:

$$\frac{1}{c_0^2} \frac{\partial^2 p'}{\partial t^2} - \frac{\partial^2 p'}{\partial x_i^2} = 0 \tag{2.14}$$

2.2.2 Monopole and multipoles sources

Starting from the wave equation (2.14) and applying initial and boundary conditions, it is possible to derive the pressure fluctuations caused by a certain source. To better clarify this concept let us consider different cases.

Monopole sources

The monopole source is a source of sound with pressure fluctuations function of the distance from the source itself [1] and omnidirectional. An example is the sound generated by a small sphere [1]. This is obtained from equation (2.14) in case of a pulsating sphere of radius a with normal surface velocity $u_0 e^{-i\omega t}$. In this case, imposing the boundary condition (and no initial ones because it is harmonic) [1] it is possible to obtain:

$$\hat{p} = -\frac{\omega \rho_0 Q e^{ikr}}{4\pi r}; \qquad Q e^{-i\omega t} = u_0 S e^{-i\omega t} \tag{2.15}$$

Where $k = \omega / c_0$ is the wave number and S the surface of the sphere.

Superposition of effects

At this point it is fundamental to consider the case in which there are several monopole sources Figure 2.1. The acoustic field at $\mathbf{x}$ is done by the superimposition of each source's field. In this way it is possible to obtain:

$$\sum_{n=1}^{N} \frac{\hat{A}_n e^{ik|\mathbf{x}-\mathbf{y}^{(n)}|}}{|\mathbf{x}-\mathbf{y}^{(n)}|} \tag{2.16}$$

Where $\hat{A}_n$ represents the contribution of each source (it would be as above in case of pulsating sphere). At large distances and applying the Taylor series expansion at the denominator, it possible to derive:

$$\hat{p}(\mathbf{x}) \approx \frac{e^{ik|\mathbf{x}|}}{|\mathbf{x}|} \sum_{n=1}^{N} \hat{A}_n e^{-ik|\mathbf{y}^{(n)}| \cdot \mathbf{x}/|\mathbf{x}|} \qquad \mathbf{x}/|\mathbf{x}| \gg |\mathbf{y}^{(n)}| \tag{2.17}$$

From this result it is possible to understand an important characteristic of the acosutic far-field. Indeed, the directionality is determined by the relative position and strengths of

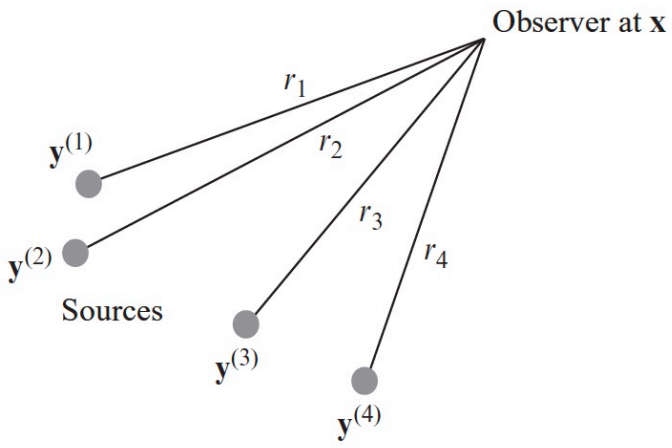

Figure 2.1: Sources distributed over a region, each source is located at $\mathbf{y}^{(n)}$ and the observer is at $\mathbf{x}$. The propagation distances are $r_n = |\mathbf{x} - \mathbf{y}^{(n)}|$. [1]

the sources.

Dipole

The dipole is defined as two monopole sources of equal strength and opposite phase at small distance d apart, where $kd \ll 1$ [1]. Considering the far field approximation it is possible to obtain:

$$\hat{p}(\mathbf{x}) \approx ikdcos(\theta) \left(\frac{i\omega\rho_0 Q e^{ik|\mathbf{x}|}}{4\pi|\mathbf{x}|} \right) \left(1 - \frac{1}{ik|\mathbf{x}|} + ... \right) \tag{2.18}$$

The sources where chosen such as: $\hat{A}_1 = i\omega\rho_0 Q/4\pi$, $\hat{A}_2 = -i\omega\rho_0 Q/4\pi$ and they were at $(0, -d/2)$, $(0, +d/2)$ in the plane. From (2.18) it is possible to derive [1]:

1. The directionality of the pressure field. It varies with the cosine between the line connecting the center of the reference system and the dipole axis;
2. The dependence on the distance scales in two different ways: $kd/|\mathbf{x}|$ in the acoustics far field ($k|\mathbf{x}| \gg 1$) and $d/|\mathbf{x}|^2$ in the acoustics near field ($k|\mathbf{x}| \ll 1$);
3. The maximum amplitude of a dipole is ikd times the one of a monopole. For the hypotheses done so far ($kd \ll 1$) this means that it is not efficient.

Therefore, because of (2) the far field approximation requires both geometrical ($|\mathbf{x}| \ll d$) and acoustics ($k|\mathbf{x}| \ll 1$) far-field.

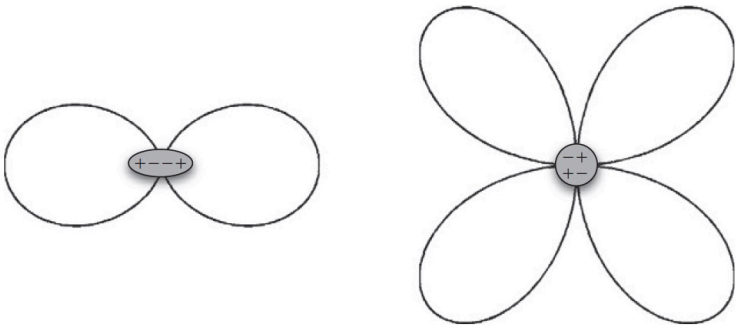

Figure 2.2: The directionality of different types of quadrupole layout. [1]

Quadrupole

A quadrupole source is obtained by putting together two dipole sources. This can be achieved in different ways such as the one in figure Figure 2.2. The resulting expression for the pressure fluctuations is very long for these two sources. Therefore, it will be presented just the most relevant part. The complete expression can be found in the book Aeroacoustics of Low Mach Number Flows at pages 61 and 62. The two expression depend on the different configurations chosen from Figure 2.2.

1. For the configuration on the left in Figure 2.2, the pressure fluctuations follows:

$$\hat{p}(\mathbf{x}) \propto (kdx_1)^2 \tag{2.19}$$

   Therefore, its directionality behaves like $cos(\theta^2)$, while, the source strength is one order of magnitude less than the monopole.

2. For the configuration on the right of Figure 2.2, the pressure fluctuations follows:

$$\hat{p}(\mathbf{x}) \propto (kd)^2 x_1 x_2 \tag{2.20}$$

   Therefore, its directionality behaves like $cos(\theta)sin(\theta)$ and the source strength is the same of the other quadrupole configuration.

2.2.3 Green's functions approach

A well-established approach used for solving the wave equation is the one implementing Green's functions. It is used to determine the pressure fluctuations $p'(\mathbf{x},t)$ at position $\mathbf{x}$ and time t coming from a source at time τ and location $\mathbf{y}$. Let us write the wave equation as a function of $\mathbf{y}$ and τ:

$$\frac{1}{c_0^2}\frac{\partial^2 p'(\mathbf{y},\tau)}{\partial \tau^2} - \frac{\partial^2 p'(\mathbf{y},\tau)}{\partial y_i^2} = 0 \tag{2.21}$$

Therefore, it is necessary to define the Green's function G that solves the inhomogeneous wave equation:

$$\frac{1}{c_0^2}\frac{\partial^2 G}{\partial \tau^2} - \frac{\partial^2 G}{\partial y_i^2} = \delta(\mathbf{x}-\mathbf{y})\delta(t-\tau) \tag{2.22}$$

Proceeding, let us multiply the (2.22) by $p'(\mathbf{y},\tau)$ and (2.21) by $G(\mathbf{x},t|\mathbf{y},\tau)$. Then subtract the two results and obtain:

$$\frac{1}{c_0^2}\left(p'\frac{\partial^2 G}{\partial \tau^2} - G\frac{\partial^2 p'}{\partial \tau^2}\right) - \left(p'\frac{\partial^2 G}{\partial y_1^2} - G\frac{\partial^2 p'}{\partial y_i^2}\right) = \delta(\mathbf{x}-\mathbf{y})\delta(t-\tau)p'(\mathbf{y},\tau) \tag{2.23}$$

Now, integrating (2.23) in both side over τ and the volume $V(\mathbf{y})$ we obtain:

$$\int_V \int_{-T}^{+T} \frac{1}{c_0^2}\left(p'\frac{\partial^2 G}{\partial \tau^2} - G\frac{\partial^2 p'}{\partial \tau^2}\right) - \left(p'\frac{\partial^2 G}{\partial y_1^2} - G\frac{\partial^2 p'}{\partial y_i^2}\right) = p'(\mathbf{x},t) \tag{2.24}$$

The first term in the integral can be manipulated in order to obtain:

$$\int_V \int_{-T}^{+T} \frac{\partial}{\partial \tau}\left(p'\frac{\partial G}{\partial \tau} - G\frac{\partial p'}{\partial \tau}\right) d\tau dV(\mathbf{y}) = \int_V \left[p'\frac{\partial G}{\partial \tau} - G\frac{\partial p'}{\partial \tau}\right]_{\tau=-T}^{\tau=T} dV(\mathbf{y}) \tag{2.25}$$

In the hypothesis of p' and $\partial p'/\partial \tau$ to be zero at $t=-T$ then the right hand side of (2.25) is zero at the lower limit. In addition to that, with the causality condition [1] it is possible to cancel also the upper limit. Applying a similar process to the second term of the integral in equation (2.23) it is possible to transform the integral into the divergence of a vector. Consequently, using the divergence theorem it is possible to change the volume integral into surface one [1]. Accordingly, by choosing a normal vector perpendicular to

the surface and pointing to the volume it is possible to obtain:

$$p'(\mathbf{x},t) = \int_{-T}^{+T} \int_S \left(p'(\mathbf{y},\tau) \frac{\partial G(\mathbf{x},t|\mathbf{y},\tau)}{\partial y_i} - G(\mathbf{x},t|\mathbf{y},\tau) \frac{\partial p'(\mathbf{y},\tau)}{\partial y_i} \right) n_i dS(\mathbf{y}) d\tau \tag{2.26}$$

From this equation, it is clear that in order to compute the acoustic field it is necessary to have the pressure and pressure gradients on the surfaces bounding the region of interest. Moreover, to solve the integral it is necessary to know Green's function which has to satisfy (2.22) and the causality condition. At this point, in order to compute an example of Green's function it is possible to take the example of the spherical surface. Knowing the solution and applying the boundary condition at equation (2.26) it is possible to determine the Green's function needed [1]:

$$G_0(\mathbf{x},t|\mathbf{y},\tau) = \frac{\delta(t - |\mathbf{x}-\mathbf{y}|/c_0 - \tau)}{4\pi|\mathbf{x}-\mathbf{y}|} \tag{2.27}$$

Substituting it into equation (2.26) it is possible to obtain:

$$p'(\mathbf{x},t) = \int_S \left[\rho_0 \frac{\partial u_n}{\partial \tau} \right]_{\tau=\tau^*} \frac{dS(\mathbf{y})}{4\pi|\mathbf{x}-\mathbf{y}|} + \int_S \left[\frac{\partial p'}{\partial \tau} n_i + \frac{p' n_i c_0}{|\mathbf{x}-\mathbf{y}|} \right]_{\tau=\tau^*} \frac{(x_i - y_i) dS(\mathbf{y})}{4\pi|\mathbf{x}-\mathbf{y}|^2 c_0} \tag{2.28}$$

In the expression written $\tau^* = t - |\mathbf{x}-\mathbf{y}|/c_0$ that is the so called "source time" [1]. It represents the time necessary for the wave to arrive at the observer. In equation (2.28) there are two terms:

1. The first term represents the sound generated by the vibration of a surface. Therefore, it is depending on its acceleration. It is also omnidirectional. Thus considered a monopole source term;

2. The second term represents the sound generated by the surface loading. It has a cosine direction, thereby, it is considered a dipole source term.

2.3 Aeroacoustics analogies

Aeroacoustics analogies are rearrangements of the Navier-Stokes equations meant to differentiate the sound generation process from the sound propagation mechanisms [1].

2.3.1 Lighthill's analogy

This analogy is meant to treat those applications in which it is necessary to account for turbulence [1]. Indeed, in linear acoustics, this was not the case. Therefore, one of the first applications of this analogy was the sound generated by jet engines. Lighthill's equations are derived from the Navier-Stokes equations without any assumption, therefore they are "exact" [1]. The process to derive Lighthill's analogy starts from the time derivation of the continuity equation (2.1) at which it is subtracted the divergence of momentum equation (2.2) (considering no body forces). In this way we obtain:

$$\frac{\partial^2 \rho}{\partial t^2} = \frac{\partial^2 (\rho v_i v_j + p_{ij})}{\partial x_i \partial x_j} \tag{2.29}$$

where the tensor p_{ij} is intended as: $p_{ij} = (p - p_\infty)\delta_{ij} - \tau_{ij}$. Therefore, the pressure is intended to be a gauge pressure [1]. Moreover, defining the the relative density perturbation $\rho' = \rho - \rho_\infty$ and subtracting $\partial^2(\rho' c_i nfty^2)/x_i^2$ from both sides of (2.29) we obtain the Ligthhill's wave equation:

$$\frac{\partial^2 \rho'}{\partial t^2} - c_\infty^2 \frac{\partial^2 \rho'}{\partial x_i^2} = \frac{\partial^2 T_{ij}}{\partial x_i \partial x_j} \qquad T_{ij} = \rho v_i v_j + (p - p_\infty) - (\rho - \rho_\infty) c_\infty^2 \delta_{ij} - \tau_{ij} \tag{2.30}$$

In this equation, it is possible to observe on the left the wave propagation mechanism. While on the right the source terms of the sound wave. The speed of sound c_∞ present in (2.30) is the speed of sound in the stationary medium, not the one in the turbulence [1]. As we said, this has been obtained without any approximation. However, the solution to this is not simple to be determined and additional considerations have to be made [1].

2.3.2 Curle's theorem

Using a similar approach to the one used for linear acoustics, it is possible to use Green's functions to solve equation (2.30). The process is very similar to the one adopted before. Therefore, I will not start the discussion from the beginning. However, since the approach used in [1] has been followed, it is possible to find the detailed beginning on page 78. Let

us start from

$$\rho'(\mathbf{x},t)c_\infty^2 = \int_{-T}^{+T}\int_S \left(\rho'(\mathbf{y},\tau)c_\infty^2\frac{\partial G}{\partial y_i} - G\frac{\partial(\rho'(\mathbf{y},\tau)c_\infty^2)}{\partial y_i}n_i dS(\mathbf{y})d\tau\right) + \int_{-T}^{+T}\int_V G\left(\frac{\partial^2 T_{ij}(\mathbf{y},\tau)}{\partial y_i \partial y_j}\right)dV(\mathbf{y})d\tau \quad (2.31)$$

Using Curle and Doack [18, 19] approach to manipulate the integral [1] it is possible to change the last term in the equation 2.31 and obtain:

$$\rho'(\mathbf{x},t)c_\infty^2 = \int_{T}^{+T}\int_S \left((\rho' c_\infty^2\delta_{ij} + T_{ij})\frac{\partial G}{\partial y_i} - G\frac{\partial(\rho' c_\infty^2\delta_{ij} + T_{ij})}{\partial y_i}\right)n_j dS(\mathbf{y})d\tau + \int_{-T}^{+T}\int_V \left(\frac{\partial^2 G}{\partial y_i \partial y_j}T_{ij(\mathbf{y},\tau)}\right)dV(\mathbf{y})d\tau \quad (2.32)$$

Lastly, it is possible to use the definition of Lighthill's stress tensor to substitute:

$$\rho' c_\infty^2\delta_{ij} + T_{ij} = p_{ij} + \rho v_i v_j \quad (2.33)$$

and with the momentum equation obtain:

$$\rho'(\mathbf{x},t)c_\infty^2 = \int_{T}^{+T}\int_S \left((p_{ij} + \rho v_i v_j)\frac{\partial G}{\partial y_i} - G\frac{\rho v_j}{\partial \tau}\right)n_j dS(\mathbf{y})d\tau + \int_{-T}^{+T}\int_V \left(\frac{\partial^2 G}{\partial y_i \partial y_j}T_{ij(\mathbf{y},\tau)}\right)dV(\mathbf{y})d\tau \quad (2.34)$$

This is actually the solution to Lighthill's equation. Therefore, it is possible to note the presence of the following sources of sound [1]:

1. The rate of change of mass flux on the surface;
2. The force per unit area applied on the fluid by the surface;
3. The momentum flux across the surface;
4. A volume integral contribution from the distribution of Lighthill's stress tensor.

By comparing these results to the ones from linear aeroacoustics, it is possible to note the sources of noise coming from turbulence are: momentum flux and the last volume

integral. Since there are no additional restrictions on the Green's functions, it is possible to use (2.27) and therefore, change (2.34) into:

$$\rho'(\mathbf{x},t)c_\infty^2 = \int_S \left[\frac{\partial(\rho v_j)}{\partial\tau}\right]_{\tau=\tau^*} \frac{n_j dS\mathbf{y}}{4\pi|\mathbf{x}-\mathbf{y}|} - \frac{\partial}{\partial x_i}\int_S [p_{ij}+\rho v_i v_j]_{\tau=\tau^*} \frac{n_j dS\mathbf{y}}{4\pi|\mathbf{x}-\mathbf{y}|} + \frac{\partial^2}{\partial x_i \partial x_j}\int_V [T_{ij}(\mathbf{y},\tau)]_{\tau=\tau^*} \frac{dV(\mathbf{y})\mathbf{y}}{4\pi|\mathbf{x}-\mathbf{y}|} \quad (2.35)$$

Also in this case there is the use of the corrected time.

Monopole and multipoles sources

In order to better analyze the results obtained from equation (2.35) it is useful to divide the equation into different parts [1]:

$$\rho' c_\infty^2 = (\rho' c_\infty^2)_{monopole} + (\rho' c_\infty^2)_{dipole} + (\rho' c_\infty^2)_{quadrupole} \quad (2.36)$$

The first term is the monopole one. Considering $v_i n_i = u_n$ it is possible to write:

$$(\rho' c_\infty^2)_{monopole} = \int_S \left[\frac{\partial(\rho u_n)}{\partial\tau}\right]_{\tau=\tau^*} \frac{dS\mathbf{y}}{4\pi|\mathbf{x}-\mathbf{y}|} \quad (2.37)$$

This equation is showing how sound can be generated by the flux of mass across a surface. If the surface is impenetrable, then this term goes to zero. If the surface is small the retarded time can be ignored (acoustically compact). In the acoustic far field, it is possible to write (2.37):

$$(\rho' c_\infty^2)_{monopole} = \int_S \left[\frac{\partial(\rho u_n)}{\partial\tau}\right]_{\tau=\tau^*} \frac{dS\mathbf{y}}{4\pi|\mathbf{x}|} \quad (2.38)$$

Which is omnidirectional in the acoustic far field. Consequently, it is named monopole term. Moreover, it does not depend on the shape of the surface.
Second, let us consider the dipole term:

$$(\rho' c_\infty^2)_{dipole} = -\frac{\partial}{\partial x_i}\int_S [p_{ij}+\rho v_i v_j]_{\tau=\tau^*} \frac{n_j dS\mathbf{y}}{4\pi|\mathbf{x}-\mathbf{y}|} \quad (2.39)$$

It is possible to rewrite (2.39) in another way, it is done just through mathematical considerations. Therefore, it is possible to write:

$$(\rho' c_\infty^2)_{dipole} = \int_S \left[\frac{\partial (p_{ij} + \rho v_i v_j)}{\partial \tau} + \frac{\partial (p_{ij} + \rho v_i v_j) c - \infty}{|\mathbf{x} - \mathbf{y}|} \right]_{\tau = \tau^*} \frac{(x_i - y_i) n_j dS\mathbf{y}}{4\pi |\mathbf{x} - \mathbf{y}|} \tag{2.40}$$

At this point, considering an impermeable surface ($\rho v_i v_j = 0$) and only the far field approximation (the second term is important in the near field) [1], it is possible to simplify the equation into:

$$(\rho' c_\infty^2)_{dipole} = \frac{x_i}{4\pi |\mathbf{x}|^2 c_\infty} \int_S \left[\frac{\partial (p_{ij} n_j)}{\partial \tau} \right]_{\tau = \tau^*} dS(\mathbf{y}) \tag{2.41}$$

From this equation, it is possible to see that for an impermeable surface, there is only surface loading that is accounting as a sound source. In equation (2.41) p_{ij} is accounting for both pressure and viscous stresses. If retarded time effects can be ignored, the source becomes:

$$(\rho' c_\infty^2)_{dipole} = \frac{x_i}{4\pi |\mathbf{x}|^2 c_\infty} \left[\frac{\partial F_i}{\partial \tau} \right]_{\tau = \tau^*} F_i(\tau) = \int_S p_{ij} n_j dS(\mathbf{y}) \tag{2.42}$$

From this, it is clear the presence of a cosine dependence and therefore, it is named dipole source. Finally, It is possible to prove [1] that the far filed intensity of a dipole scales as the sixth power of the mean flow velocity.

In conclusion, let us analyze the quadrupole term. Considering the acoustic far filed approximation, then:

$$(\rho' c_\infty^2)_{dipole} = \frac{x_i x_j}{4\pi c_{\infty^2} |\mathbf{x}|^3} \left[\int_V \frac{\partial^2 T_{ij}}{\partial \tau^2} dV(\mathbf{y}) \right]_{\tau = \tau^*} \tag{2.43}$$

From this equation, it is possible to note the directionality of the quadrupole source. It is in this term that there is the dependence on the turbulence [1]. In this case, it is possible to prove that the far field intensity scales as the mean velocity at the eighth power [1]. A noteworthy result from the previous results is:

$$\frac{(I_r)_{quadrupole}}{(I_r)_{dipole}} < \frac{U^2 V^2}{c_\infty^2 L^2 S^2} \tag{2.44}$$

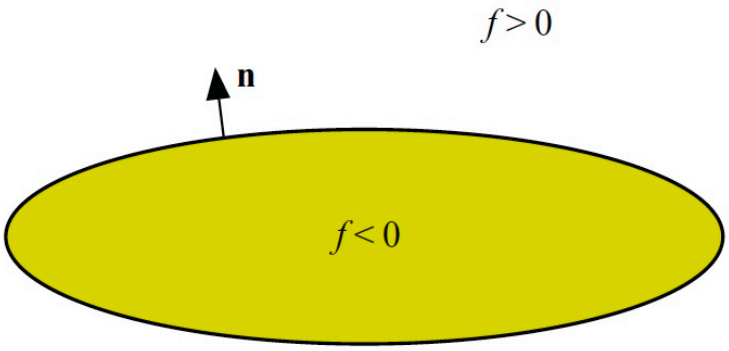

Figure 2.3: Function f that defines the surface bounding a volume. [1]

In this equation, V is the volume of the fluid, L is the length scale of the turbulence in the flow, S is the surface area of the body. In the equation mentioned above U^2/c_∞^2 is M^2 and so is the Mach number. If $V/(SL)$ is in the order of one, then for $M \ll 1$ the quadrupole source is negligible compared to the dipole one.

2.3.3 The Ffowcs Williams and Hawkings analogy

FfowcsWilliams and Hawkings approach has been introduced to adapt Lighthill's analogy in the case of moving surfaces[1]. Therefore, it is of fundamental importance to treat problems related for example to moving blades such as helicopters. This will be the actual equations that will be solved in our methodology. Indeed, we are considering manevuering propellers. Before treating this approach it is fundamental to briefly introduce the concept of generalized derivatives.

Generalized derivatives

The concept of generalized derivatives is fundamental to derive functions that present discontinuities. An example of this is the function $f(x)$ in Figure 2.3 Where $f(x) = 0$ in the surface. This is used for the situation in which there is a flow defined outside of a region S_0 but there is no information about the flow in the region S_0. In this case, it is possible to define a variable $\mathbf{v}H_s(f)$ which is the velocity outside the region but it is zero inside of it.

The Ffowcs Williams and Hawkings equation

Before deriving the equation, it is necessary to derive the continuity and momentum equations using as variables $\mathbf{v}H_s$, ρH_s, pH_s which have the properties introduced before. Following the procedure of [1] it is possible to derive the continuity equation as follows ($\rho' = \rho - \rho_\infty$):

$$\frac{\partial(\rho' H_s)}{\partial t} + \frac{\partial(\rho v_i H_s)}{\partial x_i} = (\rho v_j - \rho' V_j) n_j \delta(f) |\nabla f| \tag{2.45}$$

Similarly, it is possible to derive the momentum equation as follow [1]:

$$\frac{\partial(\rho v_i H_s)}{\partial t} + \frac{\partial(\rho v_i v_j H_s + p_{ij} H_s)}{\partial x_j} = (\rho v_i (v_j - Vj) + p_{ij}) n_j \delta(f) |\nabla f| \tag{2.46}$$

In both equations $\mathbf{V}$ is the velocity of the moving surface. Now it is possible to derive the wave equation for a moving surface. Taking the time derivative of Eq. (2.45), the divergence of Eq. (2.2) and subtracting them. Then, subtracting $\partial^2(\rho' c_\infty^2 H_s)/\partial x_i^2$ from both sides gives:

$$\begin{aligned}\frac{\partial^2(\rho' H_s)}{\partial t^2} - c_\infty^2 \frac{\partial^2(\rho' H_s)}{\partial x_i^2} = \frac{\partial^2(T_{ij} H_s)}{\partial x_i \partial x_j} - \frac{\partial}{\partial x_i}((\rho v_i (v_j - V_j) + p_{ij}) n_j \delta(f) |\nabla f|) \\ + \frac{\partial}{\partial t}((\rho v_j - \rho' V_j) n_j \delta(f) |\nabla f|)\end{aligned} \tag{2.47}$$

This is the Ffowcs Williams and Hawkings equation which can be solved using the method of Green's functions. With some mathematical manipulations [1], it is possible to derive.

$$\begin{aligned}\rho'(\mathbf{x}, t) c_\infty^2 = \int_{-T}^{+T} \int_{V_0(\tau)} \frac{\partial^2 G}{\partial y_i \partial y_j} T_{ij} dV(\mathbf{y}) d\tau \\ + \int_{-T}^{+T} \int_{S_0(\tau)} \frac{\partial G}{\partial y_i} ((\rho v_i (v_j - V_j) + p_{ij}) n_j) dS(\mathbf{y}) d\tau \\ - \int_{-T}^{+T} \int_{S_0(\tau)} \frac{\partial G}{\partial \tau} ((\rho v_j - \rho' V_j) n_j) dS(\mathbf{y}) d\tau\end{aligned} \tag{2.48}$$

It is important to notice that this solution has to be evaluated using surface and volume integrals over moving surfaces. Therefore, it is a very complex solution that can be simplified considering impenetrable surfaces in which $v_i n_i = V_i n_i$ [1]. The solution to (2.47)

becomes:

$$\rho'(\mathbf{x},t)c_\infty^2 = \int_{-T}^{+T}\int_{V_0(\tau)} \frac{\partial^2 G}{\partial y_i \partial y_j} T_{ij} dV(\mathbf{y}) d\tau + \int_{-T}^{+T}\int_{S_0(\tau)} \frac{\partial G}{\partial y_i} p_{ij} n_j dS(\mathbf{y}) d\tau - \int_{-T}^{+T}\int_{S_0(\tau)} \frac{\partial G}{\partial \tau} \rho_\infty V_j n_j dS(\mathbf{y}) d\tau \quad (2.49)$$

Since we are considering moving surfaces it is useful to consider the moving coordinates as $\mathbf{z}$ which are identical to $\mathbf{y}$ for τ_0 and then for $\tau > \tau_0$ they are:

$$\mathbf{y} = \mathbf{x} + \int_{\tau_0}^{\tau} \mathbf{V}(t')dt' \quad (2.50)$$

It is possible to prove [1] that for constant linear or angular velocity $\partial G/\partial y_i = \partial G/\partial z_i$. Since this approach is often used for rotating surfaces, it is noteworthy to report a result obtain in [1]:

$$\rho'(\mathbf{x},t)c_\infty^2 H_s = \frac{\partial^2}{\partial x_i \partial x_j}\int_{V_0}\left[\frac{T_{ij}}{4\pi r|1-M_r|}\right]_{\tau=\tau^*} dV(\mathbf{z}) - \frac{\partial}{\partial x_i}\int_{S_0}\left[\frac{(\rho v_i(v_j - V_j) + p_{ij})}{4\pi r|1-M_r|}\right]_{\tau=\tau^*} dS + \frac{\partial}{\partial t}\int_{S_0}\left[\frac{(\rho v_j - \rho' V_j)n_j}{4\pi r|1-M_r|}\right]_{\tau=\tau^*} dS \quad (2.51)$$

Here the corrected time is defined as the solution to $\tau^* = t - r(\tau^*)/(c_\infty)$. In the acoustic far field ($|\mathbf{x}| \gg |\mathbf{y}|$) it is possible to write [1]:

$$\frac{\partial G}{\partial x_i} \approx -\frac{x_i}{\mathbf{x}}\left(\frac{1}{c_\infty}\frac{\partial G_0}{\partial t}\right) \quad (2.52)$$

Therefore, substituting this equation in (2.51) we obtain:

$$\rho'(\mathbf{x},t)c_\infty^2 \approx \frac{x_i x_j}{|\mathbf{x}|^2}\frac{1}{c_\infty^2}\frac{\partial^2}{\partial t^2}\int_{V_0}\left[\frac{T_{ij}}{4\pi|\mathbf{x}||1-M_r|}\right]_{\tau=\tau^*} dV(\mathbf{z}) + \frac{x_i}{|\mathbf{x}|}\frac{1}{c_\infty}\frac{\partial}{\partial t}\int_{S_0}\left[\frac{p_{ij}n_j}{4\pi|\mathbf{x}||1-M_r|}\right]_{\tau=\tau^*} dS(\mathbf{z}) + \frac{\partial}{\partial t}\int_{S_0}\left[\frac{\rho_\infty V_j n_j}{4\pi|\mathbf{x}||1-M_r|}\right]_{\tau=\tau^*} dS(\mathbf{z}) \quad (2.53)$$

Moreover, in this expression, it is possible to understand the terms responsible for the sound generation on a moving surface. In particular, they are quadrupole terms driven by T_{ij} that represents the turbulence. The second term is the dipole source controlled by the surface loading p_{ij}. Finally, there is $\rho_\infty V_j n_j$ that depends on the surface (blade) velocity and density of the observer. It is important to notice the presence of the so called Doppler factor $|1-M_r|^{-1}$ which is accounting for the movement of the source. It is noteworthy the fact that for $M_r = 1$ the integral becomes singular.

2.4 Rotating Blades acoustics

Rotating blades emit two different sound signatures. The first one is named ”tone noise”, while the second is the ”broadband noise” [20, 1]. The former is related to sources that repeat themselves at each rotation of the rotor. While the latter is random and generated by turbulent flow over the blades [1]. A necessary parameter used for the description of the tonal noise is the Blade Passing Frequency (BPF) which is defined as:

$$BPF = \frac{B\Omega}{60} \quad (2.54)$$

Where, B is the number of blades, Ω is the rotation speed in *rpm*.

Broadband noise is generated by the random variation of blade loading when interacting with turbulence. Since it is related to turbulence, in order to well simulate this phenomenon from a numerical point of view it is necessary to use very accurate methods[21]. As it will be explained later the uRANS schemes are not able to well describe this kind of noise source. Therefore, in this thesis, it will not be treated. However, this restriction is not affecting the analysis. Indeed, it has been proved that in forward, hovering, and

transition the most important signature is the Tonal one [5, 4].

2.4.1 Tonal Noise

Tone noise is mainly generated by rotor tip speed and the flow condition in which it is operating. The tonal noise is described by the Ffowcs-Williams and Hawkings equation:

$$\rho'(\mathbf{x},t)c_\infty^2 H_s = \frac{\partial^2}{\partial x_i \partial x_j}\int_{V_0}\left[\frac{T_{ij}}{4\pi r|1-M_r|}\right]_{\tau=\tau^*} dV(\mathbf{z}) - \frac{\partial}{\partial x_i}\int_{S_0}\left[\frac{p_{ij}n_j}{4\pi r|1-M_r|}\right]_{\tau=\tau^*} dS(\mathbf{z}) + \frac{\partial}{\partial t}\int_{S_0}\left[\frac{\rho_\infty V_j n_j}{4\pi r|1-M_r|}\right]_{\tau=\tau^*} dS(\mathbf{z}) \quad (2.55)$$

Usually, at low speed the second term is dominant. Therefore, steady and unsteady pressure is key in sound radiation. Unsteady loading is usually the leading source of sound [1] compared to steady ones. This unsteadiness can be caused by several phenomena such as a change in the angle of attack.

The additional term responsible for the tonal noise is the thickness which is related to the third integral in Equation (2.55). The physical process that causes this noise is the time-varying displacement of fluid by the blade volume when rotating [1]. It is relevant only in transonic flows and can be limited by reducing the volume of the blade near the tips.

Time domain tonal noise analysis

This component is related to the second term of (2.55):

$$(p'(\mathbf{x},t))_{loading} = -\frac{\partial}{\partial x_i}\int_{S_0}\left[\frac{p_{ij}n_j}{4\pi r|1-M_r|}\right]_{\tau=\tau^*} dS(\mathbf{z}) \quad (2.56)$$

the surface integral can become integral in the blade planform (projected area) for thin blades if the acoustic wavelength at maximum frequency is much larger than the blade thickness [1]. With this simplification, it is possible to write :

$$f_i d\Sigma = ([p_{ij}n_j]_{upper} - [p_{ij}n_j]_{lower})dS \qquad |n_1|dS = d\Sigma \quad (2.57)$$

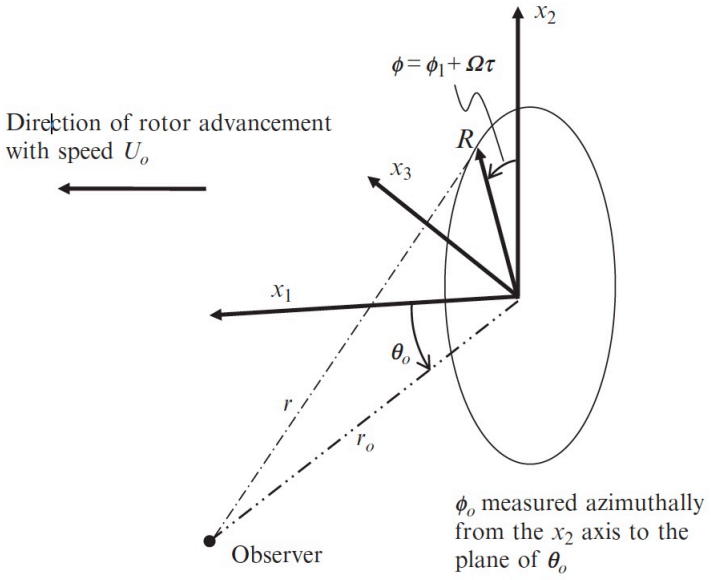

Figure 2.4: Coordinate system used for propeller and rotor noise calculations. [1]

Substituting it into equation (2.56) we obtain:

$$(p'(\mathbf{x},t))_{loading} = -\frac{\partial}{\partial x_i}\int_{\Sigma_0}\left[\frac{f_i(\mathbf{z},\tau)}{4\pi r|1-M_r|}\right]_{\tau=\tau^*} d\Sigma(\mathbf{z}) \tag{2.58}$$

From this equation, it is clear that if the load f_i repeats itself every rotation, then the tonal noise is generated. At this point, the main problem is related to the fact that in order to compute the integral it is necessary to know the exact time τ at which the load was generated. However, the problem is related to the surface integral must be evaluated at a fixed observer time, and so the emission time τ will vary over the surface of the blade [1]. In order to solve this problem the method of Farassat [22] is used. Here the spatial derivatives are shifted to source time. In this way, it is possible to obtain:

$$(p'(\mathbf{x},t))_{loading} \approx \frac{1}{c_\infty}\int_{\Sigma_0}\left[\frac{x_i}{4\pi|\mathbf{x}|^2(1-M_r)^2}\left\{\frac{\partial f_i}{\partial\tau}+\frac{fi}{(1-M_r)}\frac{\partial M_r}{\partial\tau}\right\}\right]_{\tau=\tau^*} d\Sigma(\mathbf{z}) \tag{2.59}$$

To compute the equation above mentioned, it is necessary to evaluate the location of each surface element defined in the integrand at a certain observer time. In order to compute the integral, it is necessary to define a reference system. In this case, it has been chosen the one in Figure Figure 2.4

In addition to the loading noise there is the so called thickness noise [20] :

$$(p'(\mathbf{x},t))_{thickness} = \frac{\partial}{\partial t}\int_{S_0}\left[\frac{\rho_\infty V_j n_j}{4\pi r|1-M_r|}\right]_{\tau=\tau^*} dS(\mathbf{z}) \tag{2.60}$$

Also in this case it is possible to apply the same approach adopted for the previous sound contribution. Therefore, the equation (2.60) becomes:

$$(p'(\mathbf{x},t))_{thickness} = -\frac{\partial}{\partial t}\int_{\Sigma_0}\left[\frac{\rho_\infty \mathbf{V}\cdot\nabla h}{4\pi r|1-M_r|}\right]_{\tau=\tau^*} d\Sigma(\mathbf{z}) \tag{2.61}$$

where some mathematical properties has been used as in [1] and $\nabla h = \nabla y_+ - \nabla y_-$. It is interesting to note the independence of the thickness noise from the angle of attack. The evaluation of the (2.61) can be challenging from a numerical point of view [1]. Therefore, also here it is possible to apply a simplification [22]:

$$[p'(\mathbf{x}),t]_{thickness} = \frac{\partial^2}{\partial t^2}\int_{V_\infty}\left[\frac{\rho_\infty(i-H_s(f))}{4\pi r|1-M_r|}\right]_{\tau=\tau^*} dV(\mathbf{z}) \tag{2.62}$$

In (2.62) the term $1-H_s(f)$ represents the volume inside the moving surface. Therefore, thickness noise is equivalent to the sound from a displaced mass of fluid moving through a stationary medium. This is referred to as Isom's result [22].

This result is useful from a numerical point of view. Indeed, it is possible to divide the volume of the blade into acoustically compact volume elements of volume $\triangle V_k$ centered on $y(k)$. Moreover, considering $\partial/\partial t = (1-M_r)\partial/\partial\tau$:

$$[p'(\mathbf{x}),t]_{thickness} = \sum_k \rho_\infty \triangle V_k\left[\frac{1}{1-M_r}\frac{\partial}{\partial\tau}\left(\frac{1}{1-M_r}\frac{\partial}{\partial\tau}\left(\frac{1}{4\pi|1-M_r|}\right)\right)\right]_{\mathbf{y}=\mathbf{y}^{(k)},\tau=\tau^*} \tag{2.63}$$

Frequency domain tonal noise analysis

In order to treat the tonal noise in the frequency domain let us start from:

$$p'(\mathbf{x},t) = -\frac{\partial}{\partial x_i}\int_{\Sigma_0}\left[\frac{f_i(\mathbf{z},\tau)}{4\pi r|1-M_r|}\right]_{\tau=\tau^*} d\Sigma(\mathbf{z}) - \frac{\partial}{\partial t}\int_{\Sigma_0}\left[\frac{\rho_\infty \mathbf{V}\cdot\nabla h}{4\pi r|1-M_r|}\right]_{\tau=\tau^*} d\Sigma(\mathbf{z}) \tag{2.64}$$

Since the acoustic signature of the tonal noise is periodic, this feature will be exploited in the frequency analysis. The contribution to the acoustic signature will be $p_1(\mathbf{x},t)$, let us assume the presence of B blades and T_p the period of one rotation:

$$p'(\mathbf{x},t) = \sum_{n=1}^{B} p_1(\mathbf{x}, t + nT_p/B) \tag{2.65}$$

Given that the acoustic signature of one blade is periodic, it can be expanded in a Fourier series:

$$p_1(\mathbf{x},t) = \sum_{j=-\infty}^{+\infty} c_j e^{-2\pi ijt/T_p} = \sum_{j=-\infty}^{+\infty} c_j e^{ij\Omega t} \tag{2.66}$$

where $\Omega = 2\pi/T_p$ is the rotational frequency. Combining (2.64) and (2.66) we obtain:

$$p'(\mathbf{x},t) = B\sum_{-\infty}^{\infty} c_{mB} e^{-imB\Omega t} \tag{2.67}$$

The Fourier coefficients can be computed following.

$$c_n(\mathbf{x}) = \frac{\Omega}{2\pi}\int_0^{T_p} p_1(\mathbf{x},t) e^{in\Omega t} dt \tag{2.68}$$

Using it with equation (2.64) [1]:

$$\begin{aligned} c_n(\mathbf{x}) = -\frac{\Omega}{2\pi}\int_0^{T_p} \left\{ \frac{\partial}{\partial x_i}\int_{\Sigma_0} \left[\frac{f_i}{4\pi|1-M_r|}\right]_{\tau=\tau^*} d\Sigma(\mathbf{z}) \right\} e^{in\Omega t} dt \\ - \frac{\Omega}{2\pi}\int_0^{T_p} \left\{ \frac{\partial}{\partial t}\int_{\Sigma_0} \left[\frac{\rho_\infty \mathbf{V}\cdot\nabla h}{4\pi|1-M_r|}\right]_{\tau=\tau^*} d\Sigma(\mathbf{z}) \right\} e^{in\Omega t} dt \end{aligned} \tag{2.69}$$

2.4.2 Continuous arrays

The approach described in this section is referred to the dipole sources only. Therefore, it can not be used for the thickness noise source. However, in cases of low Mach number ($M < 0.7$) this last sound source is not relevant [1].

A possibility to simulate the tonal noise produced by rotating sources is the use of a circular distributions of phase-shifted dipoles [23]. This approach consist in the use of an infinite number of fixed dipoles instead of a single one (Figure 5.1). In order to represent

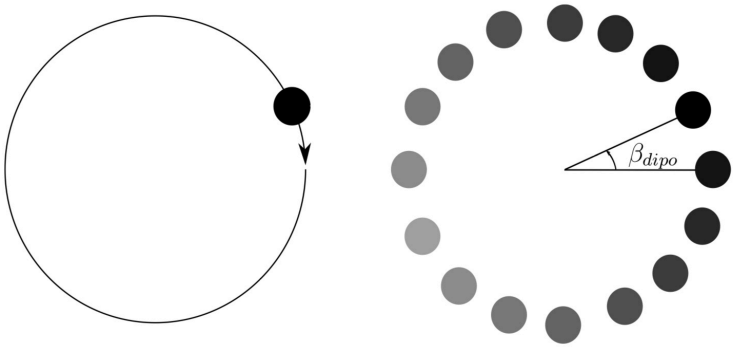

Figure 2.5: Fan source modeling strategies; (left) single rotating dipole, (right) continuous array of phase shifted dipoles.

the rotating dipole, it is used the phase shifting of the fixed dipoles determined by their angular position B_{dipo} [24]. This will be used as a numerical approach. Therefore, it will be essential to determine the number of fixed dipoles that can well represent the rotating one. Assuming a compact radial behavior of the sources, then the surface integral in (2.56) vanishes. The integral from 0 to 2π can be replaced with

$$\int_0^{2\pi} d\varphi' = \sum_{N_{dipo}} \int_{\beta_{dipo}-\frac{2\pi}{N_{dipo}}}^{\beta_{dipo}+\frac{2\pi}{N_{dipo}}} d\varphi' \tag{2.70}$$

where N_{dipo} is the number of dipoles used. The strength of the phase shifted dipoles is related to the initial one as:

$$F(\beta_{dipo}.t) = F\left(0, t - \frac{n\beta_{dipo}}{\omega}\right) \tag{2.71}$$

Let us define $F(0,t) = |F|e^{-i\omega t}$ where $|F|$ is the strength amplitude. Therefore, the force strength of each dipole becomes:

$$F^{\alpha}_{n,dipo} = \sum_{p=-\infty}^{+\infty} = F^{\alpha}_{p} e^{i(n-p)\beta_{dipo}} \tag{2.72}$$

With the same approach, if a fan has B number of blades equally spaced then:

$$F^{\alpha}_{nB,dipo} = \sum_{p=-\infty}^{+\infty} = F^{\alpha}_{p} e^{i(nB-p)\beta_{dipo}} \tag{2.73}$$

These are the forces responsible for the pressure variation in a dipole source. Therefore, introducing them into acoustic pressure formulation, the total acoustic field generated by the model becomes:

$$p'_{nB} = \frac{B}{N_{dipo}} \sum_{N_{dipo}} p'_{nB,dipo} \tag{2.74}$$

3

Computational fluid dynamics theoretical background

This thesis will focus on the numerical approach for the comprehension of the aeroacoustics phenomena that are dominant in the transition phase from hovering to forward flight. Therefore, as explained earlier, it will be necessary to analyze the fluid dynamics field of the problem with the use of a CFD solver. In this case the commercial software Simcenter Starccm+ from Siemens will be used. In order to better understand the numerical approaches with its characteristics and limitations it will be briefly introduced an overview of different numerical methods with greater attention on those applied in this methodology.

3.1 Turbulence characterization

One of the most important points of the solvers used in CFD analysis is the variety of approaches used for treating turbulence. This phenomena is driven by the following characteristics [25]:

1. Randomness. Turbulent flows have random velocity fluctuations with a wide range of length and time scales. Therefore, statistical approaches are preferred to deterministic ones.

2. Rich in scales of eddying motion. The large-scale motions are strongly influenced by the geometry of the flow. On the other hand, the behavior of the small-scale motions may be determined by the rate at which they receive energy from the large scales. They are also influenced by the viscosity of the fluid. Therefore, these small-scale motions can have a universal character, independent of the flow geometry.

3. Large Reynolds numbers. All turbulent flows are characterized by large Reynolds numbers. This indicator is defines as: $Re = intertia/viscous\ \ forces$. Therefore, turbulent flows have Re so large that fluid viscosity cannot keep the turbulence from occurring.

4. Dissipative. Turbulent flows are always dissipative in the sense that they lose energy and tend to decay.

5. High vortical. Turbulent flows are highly vortical and with high levels of fluctuating vorticity.

6. A turbulent flow has to be three-dimensional.

7. Turbulent flows are highly diffusive. They cause rapid mixing and increased rates of momentum, heat, and/or mass transfer.

8. Continuum. Turbulence is a continuum phenomenon, governed by the equations of fluid mechanics.

3.2 Mean-Flow equations

In order to understand the following concepts related to the numerical methods used to solve the Navier-Stokes equations it is useful to manipulate them in order to obtain some terms that will be used later. Let us start with the decomposition of the velocity into the mean term and the fluctuations [26]:

$$u(x,t) \equiv U(x,t) - \langle U(x,t) \rangle \tag{3.1}$$

Applying this at the momentum it is possible to write:

$$\frac{\overline{\mathrm{D}}\langle U_j \rangle}{\overline{\mathrm{D}}t} = \nu \nabla^2 \langle U_j \rangle - \frac{\partial \langle u_i u_j \rangle}{\partial x_i} - \frac{1}{\rho}\frac{\partial \langle p \rangle}{\partial x_j} \tag{3.2}$$

Where,

$$\frac{\overline{\mathrm{D}}}{\overline{\mathrm{D}}t} \equiv \frac{\partial}{\partial t} + \langle U \rangle \cdot \nabla \tag{3.3}$$

and $\langle u_i u_j \rangle$ are the so called Reynolds stresses. Apparently, (3.2) and Navier-Stokes equations are the same except for the term of Reynolds stresses. Clearly, since the difference lies in $\langle u_i u_j \rangle$: it has to be a crucial term in the description of the flow field. Reynolds stress arises from momentum transfer by the fluctuating velocity field. For a statistically three-dimensional flow, there are four equations: components of the Navier-Stokes equations and the mean continuity equation ($\nabla \cdot \langle U \rangle = 0$). However, the unknowns are more then four [26]. In particular, the so-called "closure problem" arises from the presence of the Reynolds stresses.

3.3 Modelling and Simulation

In the study of turbulent flows, the ultimate goal is to obtain a model or a theoretical description that can be used to calculate quantities of interest and practical relevance. The "turbulence problem" has no analytical solution. Therefore, it is studied using numerical approaches. It is interesting to see the reasons for which it is difficult to develop a theory or a model to solve this problem. Indeed, the velocity field $U(x,t)$ is three-dimensional, time-dependent, and random. The largest turbulent motions are almost as large as the characteristic width of the flow, thus it is directly influenced by the geometry of the problem [26]. There is a large range of timescales and length-scales. In order to describe some of the main numerical methods used it is important to distinguish between:

1. Turbulent-flow simulation: equations are solved for a time-dependent velocity field that represents the velocity field $U(x,t)$ for one realization of the turbulent flow;
2. Turbulent-model: equations are solved for some mean quantities, for example $U(x,t)$, $\langle u_i u_j \rangle$, and ε.

The two simulations are: Direct Numerical Simulation (DNS) and Large-Eddy Simulation (LES). Firstly, In DNS the Navier-Stokes equations are solved to determine $U(x,t)$. Since all lengthscales and timescales have to be resolved, DNS is computationally expensive (computational cost grows as Re^3). Therefore, they are used for low-to-moderate Re numbers flows. On the other hand, LES equations are solved for a 'filtered' velocity field $\bar{U}(x,t)$, which is representative of the larger-scale turbulent motions. This approach

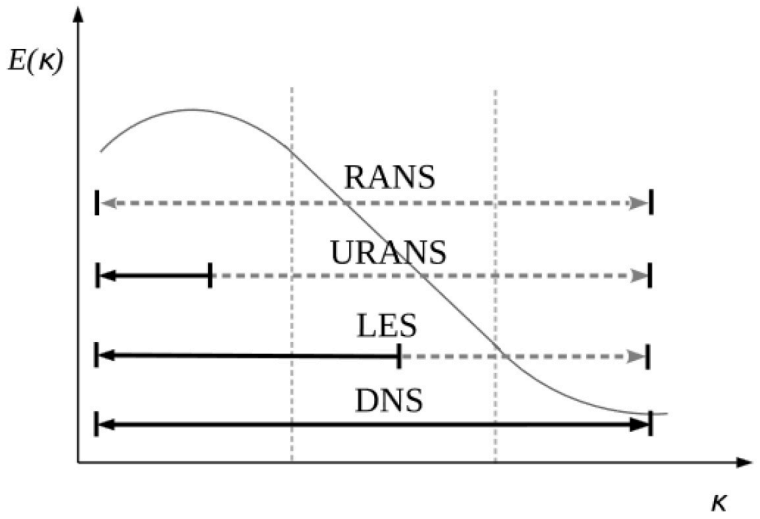

Figure 3.1: Spectrum for turbulent kinetic energy overlaid by turbulence modeling techniques with ranges of resolved and modeled turbulence. Horizontal dashed grey lines: modeled turbulence; solid black lines: resolved turbulence.[2]

includes a model for the influence of the smaller-scale motions which are not directly represented. The other types of approaches are the one called Reynolds averaged Navier–Stokes (RANS), since they involve the solution of the Reynolds equations to determine the mean velocity field. Here, models are used in order to solve the Navier-Stokes equations. With the terms uRANS (Unsteady Reynolds average equations) and RANS we are usually referring to the presence or absence of the unsteady term in the equations.

3.4 RANS and uRANS

RANS are the average Navier-Stokes equations that have been obtained earlier. They are numerically solved for the mean velocity field. However, it has already been mentioned the presence of an additional unknown (Reynolds stress tensor) that caused the ”closure problem”. Therefore, these equations need some models in order to express the stress tensor and thus close the equation system. According to the turbulent-viscosity hypothesis [26], Reynolds stresses can be defined as:

$$\langle u_i u_j \rangle = \frac{2}{3} k \delta_{ij} - \nu_{\mathrm{T}} \left(\frac{\partial \langle U_i \rangle}{\partial x_j} + \frac{\partial \langle U_j \rangle}{\partial x_i} \right) \tag{3.4}$$

This hypothesis is not always valid. However, let us consider the situations in which it can be applied. For these cases, the problem is now to determine the turbulent viscosity. It is expressed as function of a viscosity and a length.

$$v_T = u^* l^* \tag{3.5}$$

Therefore, the specification of the turbulent viscosity is then defined through the definition of u^* and l^*. These can be defined either with algebraic models or two-equation models.

3.5 RANS turbulence models

As mentioned, in order to solve the RANS equations it is necessary to define the Reynolds stresses. Therefore, there are several ways that can be used in order to close the equation system. These models start from the simpler to the more complex ones.

3.5.1 Algrebraic models

In this group of models there are two main approaches: the uniform turbulent viscosity and the mixing-length model [26].

The Uniform-Turbulent-Viscosity

This model is used for planar two-dimensional free shear flow the uniform turbulent-viscosity model can be written as:

$$v_T(x,y) = \frac{U_0(x)\delta(x)}{R_T} \tag{3.6}$$

where $U_0(x)$ is the characteristic velocity scale and $\delta(x)$ is the lengthscale of the mean flow. While, R_T is a flow-dependent constant that can be interpreted as a turbulent Reynolds number. Therefore, the turbulent viscosity is considered constant in the y direction but it varies in the mean-flow direction. It is clear that the applicability of this model is very limited [26]. These limitations are related to the difficulties to define the direction of the flow and the flow characteristics. The uniform-turbulent-viscosity model could be applied to simple wall-bounded flows. However, since the turbulent viscosity varies significantly

across the flow, the resulting predicted mean velocity profile would be inaccurate. Therefore, it is sued for s very limited range of applications [26].

The Mixing-Length-Model

This model is used for two-dimensional boundary-layer flows. The mixing length $l_m(x,y)$ is defined as a function of position. Then, the turbulent viscosity is defined as:

$$v_T = l_m^2 \left| \frac{\partial \langle U \rangle}{\partial y} \right| \tag{3.7}$$

This equation can be generalized in different ways for example, following the Smagorinsky model or the Baldwin and Lomax model. The difference in these models is related to how the absolute value in equation (3.7). All these models can be applied to all turbulent flows [26]. However, the main limitation is that the mixing length $l_m(x,y)$ has to be specified. This length is dependent on the geometry of the flow. Clearly, the problem of the l_m definition is relevant if it is applied to flows that have not already been studied. On the other hand, for well comprehended flows the mixing length can be defined without relevant problems.

3.5.2 One-equation models

Turbulent-kinetic-energy models

This model also known as ”one-equation model” [26] was developed independently by Kolmogorov and Prandtl. This approach is based on the use of turbulent kinetic energy for the definition of the velocity scale:

$$u^* = ck^{1/2} \tag{3.8}$$

where c is a constant. Using again the lengthscale as the mixing length:

$$v_T = ck^{1/2} l_m \tag{3.9}$$

In order to use (3.9) it is necessary to define c ($c \approx 0.55$) and $k(\mathbf{x},t)$. Kolmogorov and Prandtl suggested achieving this by solving a model transport equation for k. Before

defining the equation for k it is better to describe the overall model [26]:

1. the mixing length $l_m(\mathbf{x}, t)$ is specified;
2. a model transport equation is solved for $k(\mathbf{x}, t)$;
3. the turbulent viscosity is defined;
4. the Reynolds stresses are obtained;
5. the Reynolds equations are solved for $\langle U(x,t)\rangle$ and $\langle p(\mathbf{x}, t)\rangle$

Now, let us consider the k equation:

$$\frac{\overline{\mathrm{D}}\,\langle k\rangle}{\overline{\mathrm{D}}t} = \frac{\partial k}{\partial t} + \langle U\rangle \cdot \nabla k = -\nabla \cdot \mathbf{T'} + P - \varepsilon \tag{3.10}$$

Where $T' = \frac{1}{2}\langle u_i u_j u_j\rangle + \langle u_i p'\rangle/\rho - 2\nu\langle u_j s_{ij}\rangle$. In (3.10) there are two unknown ε and $\nabla \cdot \mathbf{T'}$ while all the others are known. From dimensional life it is reasonable to model ε as:

$$\varepsilon = C_D k^{3/2}/l_m \tag{3.11}$$

where C_D is a model constant. Therefore, combining (3.11) and (3.9) we obtain

$$\nu_T = cC_D k^2/\varepsilon \tag{3.12}$$

While, the other unknown is:

$$\mathbf{T}' = -\frac{\nu_T}{\sigma_k}\nabla k \tag{3.13}$$

where the "turbulent Prandtl number" for kinetic energy is generally taken to be $\sigma_k = 1.0$. Mathematically, this term ensures that the transport equation for k yields smooth solutions, and that a boundary condition can be imposed on k everywhere [26]. This model gives good results with respect to the algebraic approaches. However, there is still the problem of defining l_m.

The Spalart–Allmaras model

This is a one-equation model used for aerodynamic applications. This model is not as accurate as the ones that will be presented later. However, it is less costly and easier to

be used [26]. This was developed to remove the need for l_m definition but keep a simpler model than the two-equations ones. The model is designed for aerodynamic flows, such as transonic flow over airfoils, including boundary-layer separation [26]. This model is based on some complicated details that will not be presented here. However, it is enough to say that it has been proven successful for the scopes it was designed. In any case, it can not be used for a wider range of simulations.

3.5.3 Two-equation models

In this section there will be a presentation of more complex and accurate model for the closure of the RANS. The advantage of the two-equation models is that they do not need flow dependent specifications such as l_m [26].

The $k-\varepsilon$ model

In this model transport equations are solved for two turbulence quantities (k and ε). This model is based on:

1. the turbulent viscosity hypothesis;
2. the model transport equation for k (the same as before);
3. the model transport equation for ε
4. the specification of the turbulent viscosity as:

$$\nu_T = C_\mu k^2/\varepsilon \tag{3.14}$$

where $C_\mu = 0.09$

As mentioned, the k equation is the same as (3.10). On the other hand, the ε equation is derived empirically [26] and it is:

$$\frac{\overline{\mathrm{D}}\langle\varepsilon\rangle}{\overline{\mathrm{D}}t} = \nabla\cdot\left(\frac{\nu_T}{\sigma_\varepsilon}\nabla\varepsilon\right) + C_{\varepsilon 1}\frac{P\varepsilon}{k} - C_{\varepsilon 2}\frac{\varepsilon^2}{k} \tag{3.15}$$

where all the standard values for the model are: $C_{\varepsilon 1} = 1.44$, $C_{\varepsilon 2} = 1.92$, $\sigma_k = 1.0$, $\sigma_\varepsilon = 1.3$.

The $k-\varepsilon$ model the simplest complete turbulence model [26]. At the same time it has one of the largest range of applicability: heat transfer, combustion, multi-phase flows.

The $k-\omega$ model

This is still a two-equation model. However, instead of using ε it uses ω as second equation. Here, $\omega = \varepsilon/k$ and its equation is:

$$\frac{\overline{\mathrm{D}}\,\langle\omega\rangle}{\overline{\mathrm{D}}t} = \nabla\cdot\left(\frac{\nu_T}{\sigma_\omega}\nabla\omega\right) + C_{\omega 1}\frac{P\omega}{k} - C_{\omega 2}\frac{\omega^2}{k} \tag{3.16}$$

Looking at this equation there is no difference between the $k-\omega$ model and the $k-\varepsilon$ model. However, it can be shown that for inhomogeneous turbulence flows there is an additional term that distinguishes this equation from the other one [26]. For boundary-layer flows, the $k-\omega$ model is superior both in its treatment of the viscous near-wall region, and in its accounting for the effects of streamwise pressure gradients [26]. On the other hand, the treatment of non-turbulent free-stream boundaries is problematic.

An additional model was proposed. It was designed to yield the best behavior of the $k-\omega$ model and the $k-\varepsilon$ model. It is written as a $k-\omega$ model, with the ω equation:

$$\frac{\overline{\mathrm{D}}\,\langle\omega\rangle}{\overline{\mathrm{D}}t} = \nabla\cdot\left(\frac{\nu_T}{\sigma_\omega}\nabla\omega\right) + (C_{\varepsilon 1}-1)\frac{P\omega}{k} - (C_{\varepsilon 2}-1)\frac{\omega^2}{k} + \frac{2\nu_T}{\sigma_\omega k}\nabla\omega\cdot\nabla k \tag{3.17}$$

but with the final term multiplied by a 'blending function.' Close to walls the blending function is zero (leading to the standard ω equation), whereas remote from walls the blending function is unity (corresponding to the standard ε equation). This blended model is called $k-\omega$ *SST*. This has been proved very successful for external aerodynamic.

4

Literature Review

In this chapter, there will be an analysis of current works concerning the aeracoustics of drones and isolated propellers. Most of the studies are focusing on the hover configuration and there is a lack of material concerning the transition and maneuver configurations. The purpose of this chapter is to better motivate the reasons behind this thesis and also to explain the starting point for my study.

4.1 Drone in Hovering

For a hovering drone, the most annoying noise signature is the one related to tonal sound [3]. For the case of low mach number and thin blades, the main source of tonal noise are the periodic unsteady loads [3]. In the case of multicopter drones, these unsteady loads are caused by the non homogeneous flow in which the rotors are moving. In particular, the unsteady loads are due to two main sources. First, the interaction between propellers and drone's structure [27]. Second, the interaction between different propellers [28].
Where φ is the azimuth angle of the propeller's blade. From Figure 5.1 it is possible to understand the effect of blade-blade interaction. Indeed, the presence of additional propellers causes fluctuations of the thrust itself. Moreover, it is also responsible for a reduction in aerodynamic performance (lower average thrust) [3]. On the other hand, the fluctuations on the isolated-propeller case are related to the interaction between the blade

and the propeller wake [3].

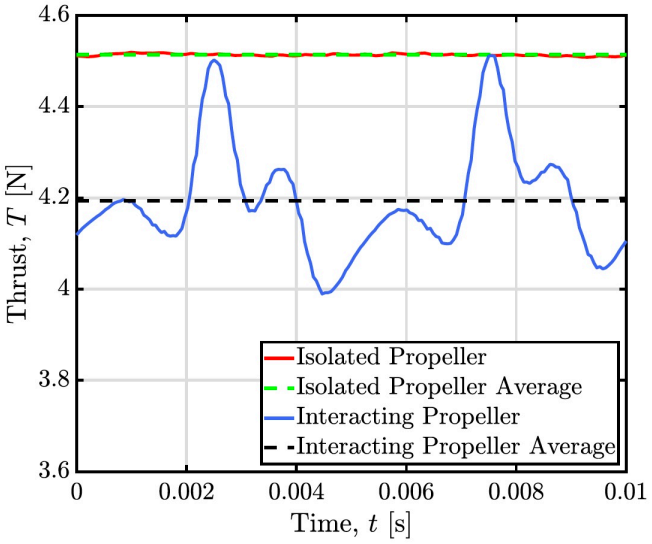

Figure 4.1: Comparison between the thrust of the isolated propeller against the one of a propeller interacting with the other three. In solid line, the instantaneous quantities are shown, whereas in dashed line the averaged ones are depicted. [3]

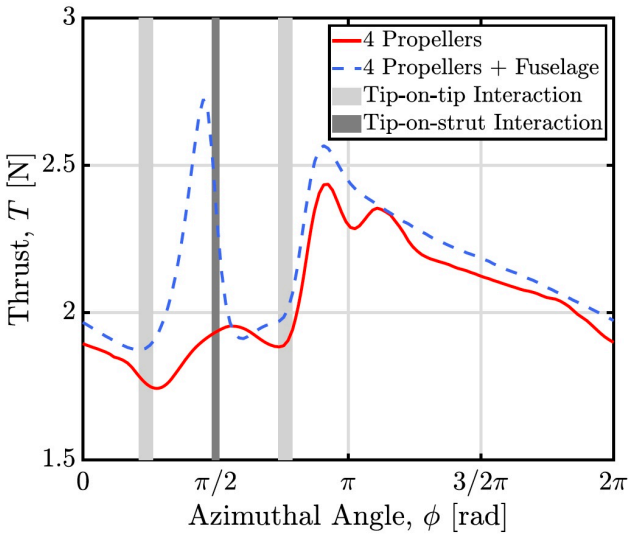

Figure 4.2: One-blade thrust against the azimuthal angle φ extracted from the four-propellers case in red solid line and from the four-propellers-and-airframe case in blue dashed line. The light-grey bands represent the tip-on-tip interaction zones, whereas the dark-grey band represents the tip-on-strut interaction zone. [3]

Also from Figure 4.2 it is clear the importance of the interaction of propellers with the structure in the creation of unsteady loads. However, for this phenomenon there is a beneficial effect on the average lift created. Acoustically, this effect produces an amplification in almost all directions of at least 5 dB [3].

4.2 Transition from Hovering to Forward Flight

The relevance of the transition maneuver for noise production has been studied and it is clear [11]. Indeed, it is considered the second most annoying flight configuration after the forward flight. An experimental characterization of the transition maneuver was conducted [4]. This experimental set-up was related to the transition of a single propeller from a vertical position to forward flight. During the experiment, both the aerodynamic and the acoustic of the system were described. An important parameter used was the advanced ratio defined as: $\mu = Ucos(\alpha)/\rho R$. Moreover, also the coefficient of Thrust was: $C_T = T/(\rho(R\Omega)^2 A)$. In this study they studied the following effects on the rotor noise:

1. Effect of rotation speed;
2. Effect of inflow velocity;
3. Effect of rotor disc tilting angle.

Analysis Figure 4.3 and Figure 4.4 it is possible to retrieve some noteworthy conclusions that are described in [4]. This will help the analysis of the acoustic data during the maneuver later in the thesis.

1. Effect of rotational speed: assuming an increase in rotational speed (considering freestream velocity and α to be constant) it is expected a shift in the tonal noise. Moreover, it is measured an increase in OASPL. [4]
2. Effect of freestream inflow velocity: with an increase of inflow velocity it is expected an increase in tonal noise [4]. Moreover, as α increases at higher speeds the tonal noise seems to be dominant at the first BPF [4].
3. Effect of rotor disc tilting angle: the increase of tilt angle is expected to reduce the rotor noise because of the highly non uniform condition that is met [4]. This has been measured up to a tilt angle of $\alpha = 20$. Once that value has been passed, the effect seems to be the opposite.

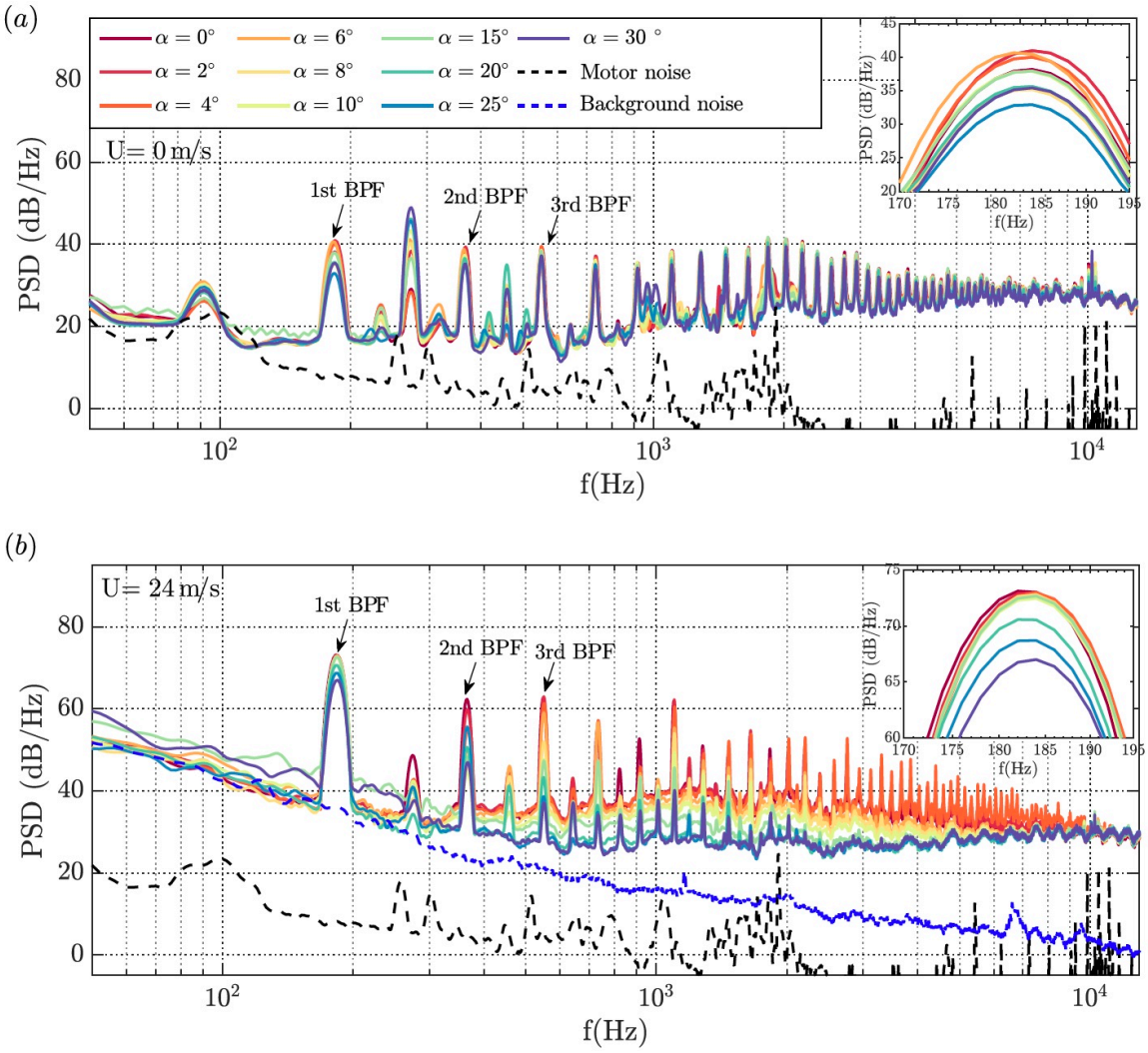

Figure 4.3: Effect of tilting angle on the radiated noise spectra at 90° microphone for angles of 0°<α <30° at N = 5500 rpm at freestream velocities of (a) U =0 m/s and (b) U =24 m/s. A close-up look for the 1st BPF is presented on the top-right corner of the each sub-figure. [4]

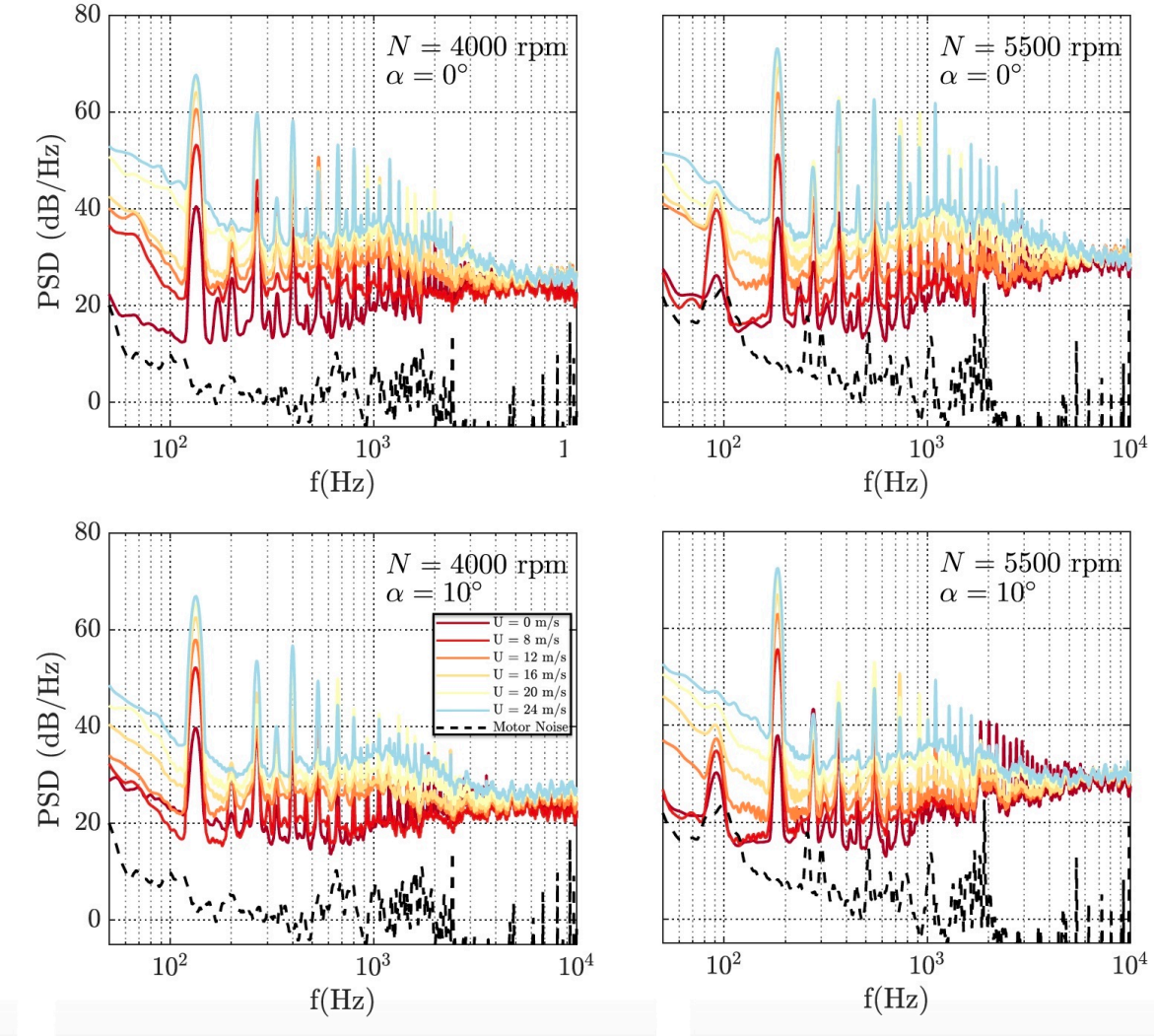

Figure 4.4: Power spectral density of the far-field pressure fluctuations for rotor in hover and tilting flight at α = 0 m/s and α = 10 m/s and over a freestream inflow velocity range of 0 m/s < U < 24 m/s. [4]

4.2.1 Maneuvering propellers acoustics prediction

An acoustic study of a maneuvering propeller has been developed in [29]. This paper's focus was the computational efficiency of a numerical code for the solution of FW-H equations. Therefore, this concept exceeds the scope of this thesis. However, the most important concept developed in that paper is that the aeroacoustic analysis for a maneuvering propeller has been based on the solution of FW-H equations is time domain. In this paper the solution of FW-H equations was based on a permeable surface in order to account for transonic effects [29] typical for helicopters studies.

4.3 Forward Flight

The forward flight annoyance has been proven to be of great impact [11]. This flight maneuver was the subject of several studies both numerical and experimental. Here I am going to present some of the results obtained in [5]. The main outcomes obtained here are:

1. Loading and pressure fluctuations due to the tilting angle are responsible for the noise generation [5];
2. When the advance ratio decreases, the SPL (Sound Pressure Level) at 1 BPF increases due to the increased fluctuation of the unsteady loading [5];
3. The directivity of the OASPL (Overall Sound Pressure Level) is the same as that of the SPL at 1 BPF, which means that the tonal noise is the dominant source of propeller noise [5].

4.4 Overset mesh

At the beginning of the thesis it was explained that it will be used the Overset mesh method, also known as chimera mesh approach. This method is well established in the rotorcraft research area [14, 12, 30]. The success of the method is due to the fact that the use of multiple grids makes the CFD simulations of bodies in relative motion much easier. This method consists in the use of at least two computational grids. These grids are overlapping

and transferring information of the flow from one to the other [31]. Normally, one mesh is describing the whole computational domain (background mesh) and the other mesh is describing the mesh for a smaller part of the domain which is moving (moving mesh). Usually, the background mesh is coarser than the moving one. In the use of the overset mesh method, there are several cells with different purposes [31]:

1. Active cells: in these cells the flow equations are solved. These cells are present both in the background and moving mesh.
2. Acceptor cells: in these cells there is information transfer between the two (or more) grids. Also these are present in both meshes.
3. Passive or inactive cells. In these cells the flow is not solved.

It is noteworthy to highlight the differences between an overset mesh approach and a sliding mesh one. Usually, using a sliding mesh approach, the computational domain must be divided in two: a stationary and a rotational domain. These are then connected through a numerical interface [13]. In this approach the two different domains are always different, and they are communicating only through the interface. On the other hand, in the overset mesh, the different meshes are moving one on the other. Therefore, the flow equations are solved in one mesh that later will exchange information with the one in a lower hierarchical level.

From this description it is clear that for the case studied in this thesis the overset mesh is the best choice. Indeed, it is especially recommended when considering large body motions with interacting parts [31]. However, it has been observed that the overset mesh usually requires a higher computational cost when compared to a more classical sliding mesh. [32]

4.5 Motivation of the thesis

After this presentation it is clearer the reason for my study. Indeed, the importance of the transition phase for the aeroacoustics of a drone is well established. However, it has been studied only from an experimental point of view. Therefore, the objective of this thesis is to create a methodology and validate its results for dealing with the transition from a numerical point of view. The work will be organized in the following way: first, it

will be studied both the fluid dynamic and the acoustic of a single propeller in transition. This step is crucial in order to understand how to treat from a numerical point of view the transition itself. Indeed, during the transition the periodic nature of the loading variation is lost. Moreover, this first passage will be useful to validate and understand how to properly use the overset mesh method. In a second step it will be treated the problem of the drone.

5

Fluid Dynamics Methodology

This chapter is meant to describe the methodology used for the description of the maneuvering drone's fluid dynamics. The methodology used to obtain the loads acting on the propeller's blades will be described. It will be necessary to explain the choices made in the definition of the simulation environment: the overset mesh approach and the simulation set-up. This analysis started from the single propeller case and continued with the full drone simulation. Such an approach was done for two reasons. Firstly, it was possible to test the methodology with an increasing level of difficulty. Thus allowing a better understanding of the parameters used in the simulation set-up. Secondly, in this way, it was possible to analyze different effects due to blades and body frame interactions. Indeed, the propeller's behavior is expected to be different if isolated or in the drone configuration [3].

The transition maneuver is a complex process to be simulated from a fluid dynamic point of view. The challenging nature of the phenomena is mainly due to:

1. First, the numerical effort needed for the discretization of the domain. Indeed, the overset mesh approach is expected to have a high computational cost [32];
2. Second, the complexity of the motion description. Indeed, the maneuver can be divided into several rigid body motions that are happening simultaneously. Starting with the rotation of the rotor around its axis. A change in the propeller RPM is necessary to vary the thrust magnitude. Consequently, the propeller tilts thus translating in the desired direction.

3. Finally, the transient nature of the problem. Indeed, it will be necessary to adopt an unsteady simulation with the motions described above. This is clearly introducing several concerns regarding the convergence of the simulation. [29]

Since the use of chimera mesh had to be validated, the study started with the hovering condition of both the propeller and drone. Indeed, for this case, a wide range of numerical and experimental results were available [3, 33].

5.1 Single propeller in hovering

5.1.1 Geometry

The propeller used for the study was the DJI propeller. This is part of the DJI Phantom II quadcopter that will later be used in the study of the full drone simulation. This choice was led by the availability of the propeller CAD and of both numerical and experimental results. These data were provided by NASA Ames Research Center. The model 9450 used in the study has an average chord of approximately 0.025m and a rotor diameter of 0.239m. It can be seen in figure Figure 5.1

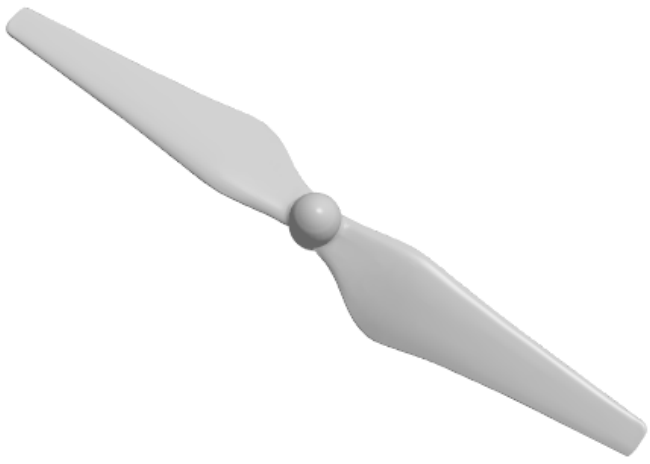

Figure 5.1: DJI propeller geometry

5.1.2 Domain, Mesh and Boundary conditions

The domain has been defined similarly to the one in [5]. From Figure 5.2 and Figure 5.3 it is possible to see that a prism shape was used. Its dimensions have been chosen following the approaches used in [3, 5] ($R = 0.1195\ m$ is the propeller radius). In this way, it was guaranteed the full development of the wake, as well as the distance of the domain's surfaces from the propeller. Usually, for the hover configuration, it is suggested to use a "bullet shape" domain [31]. This choice is justified by the symmetry of the case. However, in the transition case, this symmetrical characteristic is no more present. This is due to the tilt of the propeller and of the wake. Therefore, although the bullet shape domain would have been ideal in this first validation step, it has been discarded in order to implement directly the final configuration of the numerical environment.

Mesh

The mesh design was probably one of the most important and delicate steps of all the methodology. It was necessary to define the different levels of meshes used:

1. Propeller's mesh: this mesh is the one rotating with the propeller while in hover;
2. Wake mesh: this will be tilting and translating when the forward movement is necessary. During the hovering study it was stationary;
3. Background mesh: this is the stationary mesh over which the others are moving.

In the overset mesh approach it is necessary to guarantee that cells of different mesh levels need to have a comparable size in the contact area [31, 32]. Otherwise, it is not possible to ensure a correct passage of information from one level to the other.
Let us start the analysis from the background mesh. Here, it was necessary to mesh the domain in order to guarantee several peculiarities: a refined region near the propeller and in the area of the wake. The reason for this is straightforward, indeed, it has to be guaranteed a good resolution close to the region where the most important fluid dynamics phenomena are happening. Moreover, in order to reduce the computational cost, it was necessary to decrease the cell sizes near the end of the domain. All these characteristics were taken into account defining different volumes in the background domain that would have been meshed with different, but fixed, constraints. These volumes are the ones highlighted in: (Figure 5.3, Figure 5.2).

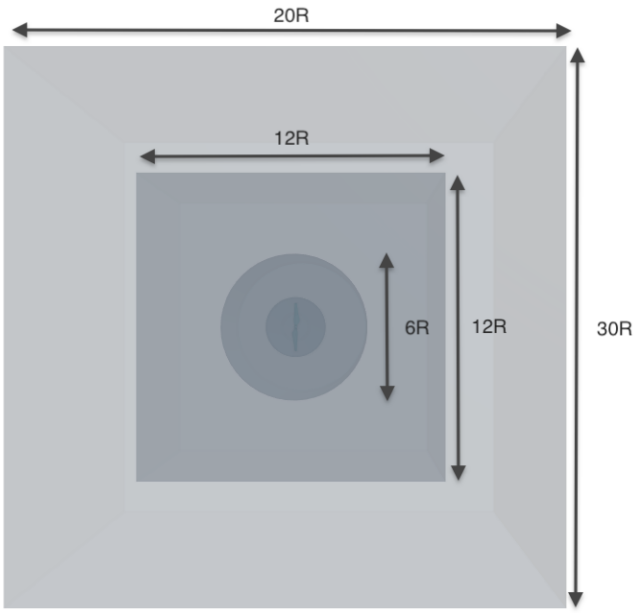

Figure 5.2: Domain for the hovering of the propeller.

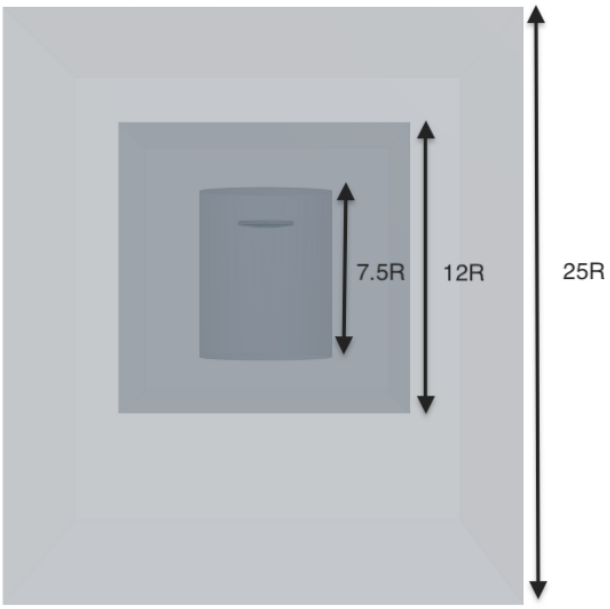

Figure 5.3: Domain for the hovering of the propeller.

The wake-mesh was introduced in order to guarantee a smooth transition of cell size be-

tween the propeller domain and the background domain. Therefore, it was an additional part that would be extremely useful in the maneuver study. Indeed, during the transition, this region will be allowed to follow the propeller. Therefore, it guaranteed a refined discretization avoiding refining the whole background mesh.

Finally, the propeller mesh is defined. This region of the simulation is the one rotating. In this domain, a prism layer mesh is used in order to discretize the propeller's wall surface.

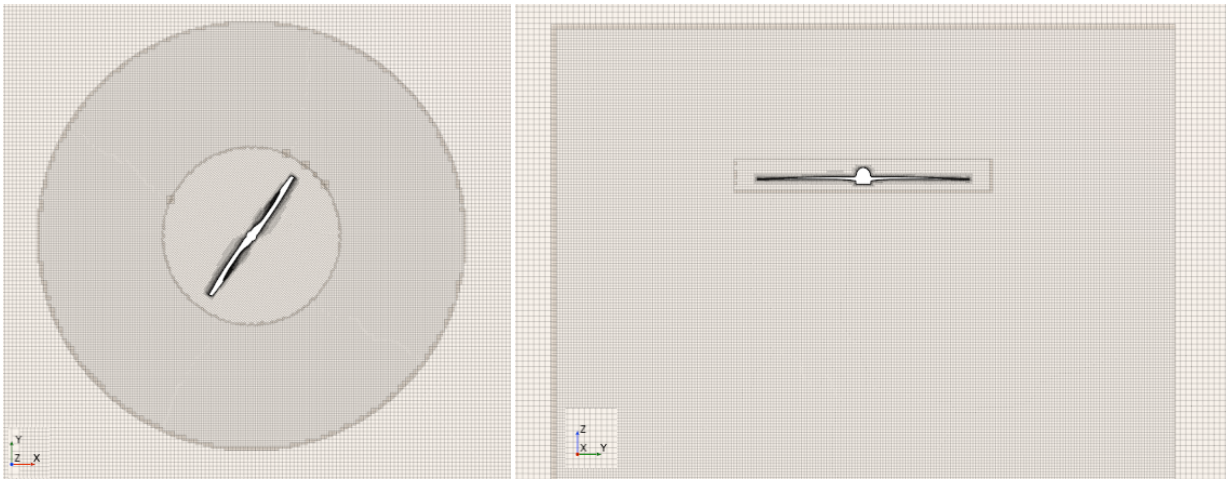

Figure 5.4: Adaptive mesh view on different planes.

In order to better understand how the overset mesh works, in Figure 5.4 is reported the mesh from different points of view. After initializing the simulation, the software applied the "hole cutting" process that consists in the cancellation of the non-active cells. In this case, the non-active cells are the ones occupied by the propeller. Moreover, in Figure 5.4 it is possible to notice that the overlapping cells of the two different regions have been highlighted. These are the elements where the information exchange is actually happening.
In the meshing process it has been used a "Base" parameter as a reference for the cell size in all three regions. In this way, it was possible to change the value of the "Base" and re-mesh the whole simulation keeping the same relations between all the different levels of mesh.
The values used are ($Base = 2.2e-4m$): The setting reported in Table 5.1 have been chosen based on some suggestions and simulations in [31]. While the values related to the

Domain's name	Base size value
Background domain	Base · 256
Wake domain	Base · 16
Rotating propeller's domain	Base

Table 5.1: Domain parameters.

Minimum Surface Size	25% (of Base size)
Number of Prism Layers	10
PL Near Wall Thickness	2E-6 m
PL Total Thickness	0.001 m

Table 5.2: Propeller's domain parameters.

boundary layer thickness have been chosen from [3] in which identical conditions where applied. For the rotating domain, it has been used a Prism layer mesher. The settings used in this mesher were: These parameters have been chosen looking at different simulations performed at VKI and in the Starccm+ manual for a similar case [31]. With these settings, the final number of cells used are $2.2e7$. This number of cells is much larger than the one used in the study of [3] where a sliding mesh was used. However, this was necessary for the stability of the result. A more detailed discussion on this subject has been done later in the thesis.

The values chosen in Table 5.1 are of primary importance. Indeed, through these values, it is possible to guarantee the exact match of the cell size on the overlapping layers. This consideration is crucial for the correct convergence of the results and in general for the chimera approach. Otherwise, there would be a larger propagation of error [12].

Mesher choice

In the methodology definition, it has been studied the difference in the results using both the trimmed mesher and the polyhedral mesher. A similar analysis had been performed at VKI for the drone in hover and for that case, it has been found that the polyhedral mesh was able to provide more precise and less computationally expensive results.
On the other hand, using the overset mesh approach it has been observed a different outcome with respect to the results in [3]. Indeed, it has been tested both the polyhedral and

Parameter at the 3rd revolution	Polyhedral mesh	Trimmed mesh
Mean Thrust value [N]	4.64	4.87
Error %	3.34	1.54
Fluctuations %	1.74	1.14
N. of cells	4.7 e7	6.7 e7

Table 5.3: Trimmed and polyhedral mesh comparison.

the trimmed mesher using the same settings and domains. A relevant difference in the settings has been the Base size value. Indeed, using the same base size the software was not able to mesh the domain because of computational limits.
Therefore, in order to overcome this problem, it has been used a Base size such that the overall number of cells was lower in the polyhedral case, but in the wake and propeller domain the number of cells was comparable. In this way, a similar discretization level was guaranteed in the crucial regions.
The results are described in the following table, where fluctuations and errors are referred to the experimental results [33]: From this table, it is noteworthy that there is not a real advantage in choosing one or the other. However, as mentioned before, for the same amount of computational power the trimmed approach is able to reach a more precise and less fluctuating result (see Figure 5.5). Therefore, the trimmed mesh have has chosen for further computations. A similar result has been obtained in [34] using Starccm+.

Boundary Conditions and Solver settings

In this simulation, the boundary conditions used are:

1. Stagnation inlet: for the sides and the upper surface of the domain. This boundary condition is used when on the boundary the flow can be assumed at rest [31]. This was guaranteed by the distance of the boundary from the propeller. Here, ambient conditions were applied: $P = 101325\ Pa$, $T = 300\ K$;

2. Pressure outlet: this is used where the wake is expected to influence the flow field. In this case only the ambient pressure had to be specified.

The main models used in the simulations have been:

1. SST-kω;

2. RANS;

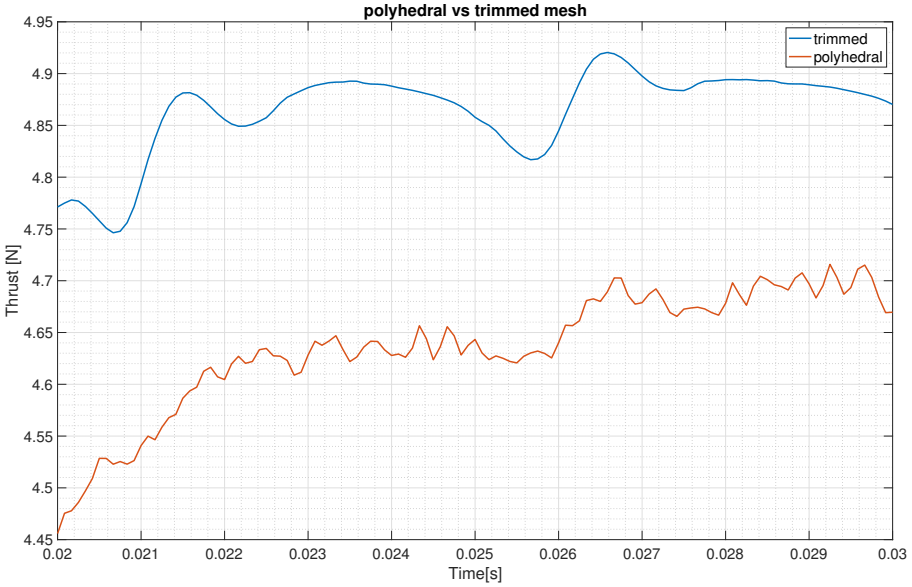

Figure 5.5: Propeller trust in hovering during the third revolution using both trimmed and polyhedral mesh.

3. Coupled flow;
4. Ideal Gas;
5. Implicit unsteady.
6. second order time accuracy.

These are selected in the physics of the computational domain. The use of uRANS impose a limit to the solution. Indeed, it is not possible to solve the turbulence scales and therefore the broadband noise cannot be predicted [21]. However, it is accepted this limit in order to avoid the use of more precise but also more demanding turbulence models [15, 16, 35].
In the solver settings it has been used the 2nd order time discretization with a $dt = 2.77775e-5 \cdot 3\ s$. This time step coincides with a rotation of three deg each time step. Indeed, the rotational speed was 6000 *rpm*. A typical time step for these simulations is $1°/s$ [36]. However, it has been observed that for the chosen time step the simulation was converging to a precise result and in a faster way with respect to the ideal time step choice. This time step was used also for the sliding mesh approach in [3].
The choice of SST-kω model has been made for the theoretical reasons that can be found in Chapter 3 and because this method has been used for similar studies and has been

proven to work in all these applications [30, 35].
For all the cases studied in this thesis, the typical Mach number is $M < 0.3$. Therefore, it would be reasonable to use an incompressible formulation. However, from [31] and during a dialogue with Starccm+ experts it emerged that the use of compressible flow was preferred. This might be related to the mesh method used. Indeed, for the same simulation using a sliding mesh method, it was used an incompressible formulation [3]. A direct consequence of this is the use of the coupled flow solver that is dealing with all Navier-Stokes equations simultaneously [31]. These last two choices will result in a longer time during the solution of the CFD simulation. However, these were recommended to avoid convergence problems.

Methodology validation for the single propeller

In order to validate the methodology of the overset method it has been tested the hover maneuver. Here are reported some of the main results. In the simulation process, it has been tried two different approaches:

1. First, starting from a steady-state solution with a developed wake and switch the simulation to unsteady;

2. Second, starting directly with the unsteady one.

These two paths have been tried in order to understand which one was going to provide the fastest result. In the end, both approaches needed the same amount of time to arrive at convergence. Therefore, it has opted for the second approach in order to avoid the steady-state simulation. The convergence of the simulation has been controlled with two different monitors: the torque and the thrust generated by the propeller. Moreover, the classical residual monitor has been employed. However, the residuals monitor was less relevant than in a steady-state simulation. Indeed, the simulation is changing in each time step. Therefore, the residuals will never reach a very low and flat graph. In any case, it was noteworthy to monitor that they never diverged.

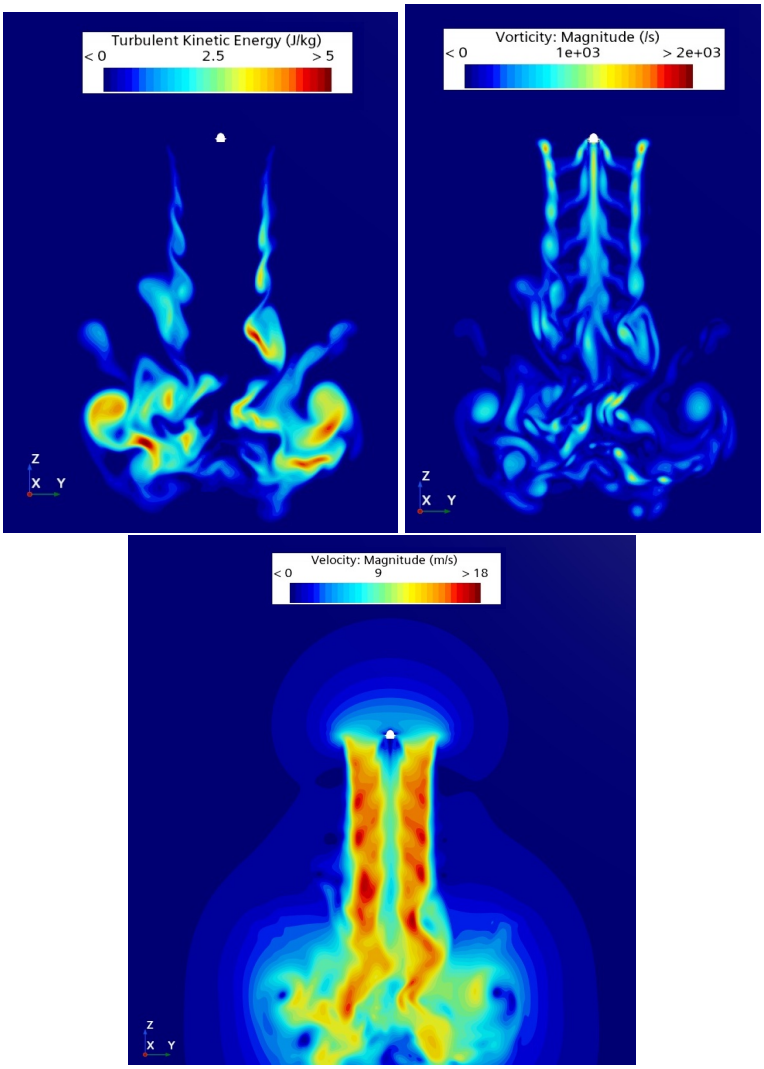

Figure 5.6: Velocity, Vorticity and Turbulent kinetic energy magnitude for the propeller in hovering.

From Figure 5.6 is possible to see that the wake under the propeller is symmetrical, except for the area far from the propeller where some differences may arise. Moreover, from the turbulent kinetic energy figure it is possible to see that the turbulence created by the tips is dominant with respect to the one created by the hub. As mentioned before, the Thrust has been used as a monitor. Therefore, it is useful to cite some of the results obtained. Here the numerical results have been compared to the experimental data from [33]: From the comparison with the results obtained by [3] and the measured ones [33] it possible to conclude that the simulation has properly resolved the case studied.

Parameter	CFD results
Mean Thrust value [N]	4.81
Error %	0.4
Fluctuations %	0.5
N. of cells	2 e7

Table 5.4: CFD results. The comparison is made with respect to the experimental results.

Base Size	N. cells	CFD results
2 e-4	2.2 e7	4.81
2.5 e-4	1.4 e7	4.79
3.3 e-4	7.1 e6	-
5 e-4	2.7 e6	-

Table 5.5: Convergence study of the mesh.

5.1.3 Mesh convergence study

At this point, it is necessary to study the convergence of the results with respect to the mesh size. Therefore, it has been changed the value of the Base size and it has been performed the simulation for the hovering of the propeller. In table Table 5.5 it has been reported the value used for the Base size and the results obtained. The last values of the table are not provided because the mesh was too coarse for the ”hole cutting” process to happen correctly. Therefore, the simulation was not performed. On the other hand, for the case of Base Size nr. 2 the simulation was performed and the mean value was very well computed. However, from Figure 5.7 it is possible to see that the fluctuations are significant.
It is noteworthy that by comparing the same simulation with the ones performed in [3], the overset mesh approach is more sensible to the domain discretization than the sliding mesh approach.

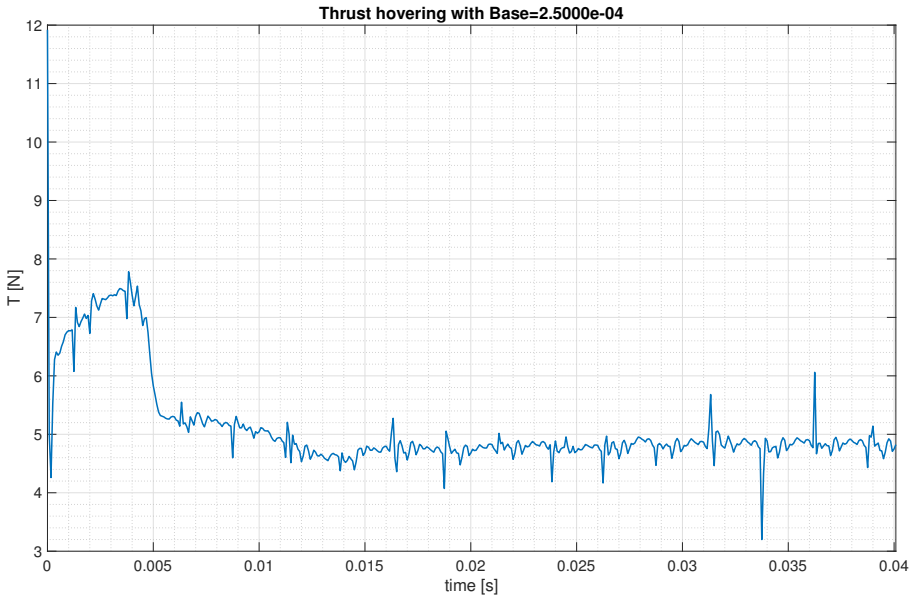

Figure 5.7: Thrust for a different size mesh.

5.2 Drone in hovering

Up to now, it has been described the methodology and the results concerning the isolated propeller simulation from the aerodynamic point of view.
Now it has been considered the same approach used before but in the case of the drone. Also here, it has been validated using some numerical data obtained at the VKI and in [3]. Since the general set-up and configuration is very similar to the one used for the single propeller, only the differences will be discussed in detail.

5.2.1 Geometry and Mesh

The geometry of the drone simulation consists of four propellers and the body frame. It has been avoided the use of electric motors just for simplicity reasons. A different view of the drone has been provided in Figure 5.8a and Figure 5.8b

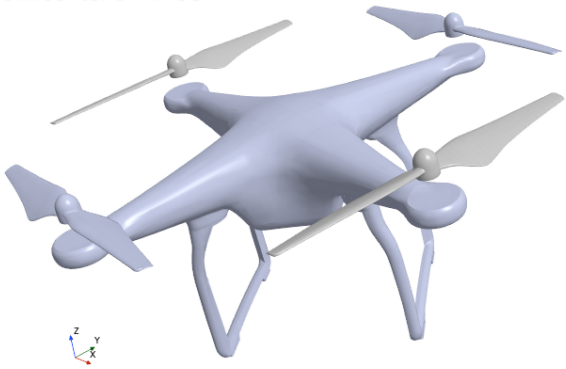

(a) Geometry drone view 1.

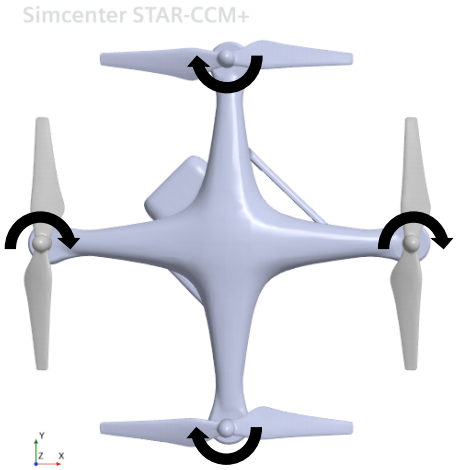

(b) Geometry drone view 2.

The mesh configuration for this case has been performed trying to reduce as much as possible the number of cells in order to have a faster simulation. The background domain is the same used for the single propeller simulation. On the other hand, for this case, it is necessary to introduce additional regions: one for each additional propeller and one for the body frame. This increases the amount of complexity as well as the computational cost because of a larger number of interfaces and interaction between different propellers and body frame. In the following figures, it is possible to look at the final mesh configuration used. All the parameters used for the size of the mesh and the boundary layers are the same imposed in the single propeller case.

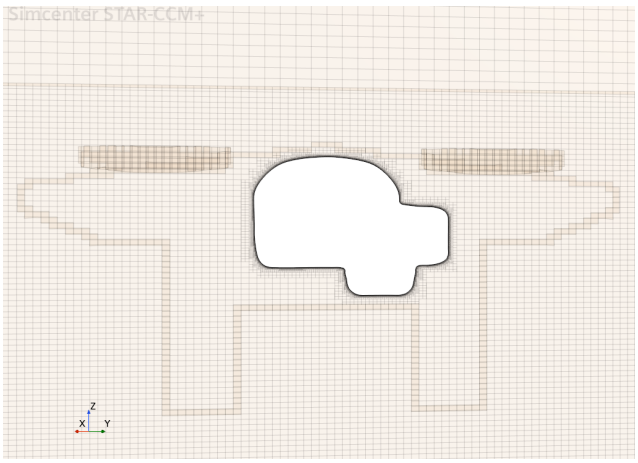

(a) Mesh for drone case view 1.

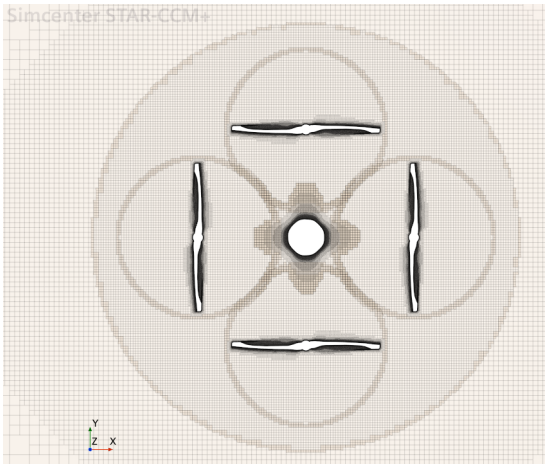

(b) Mesh for drone case view 2.

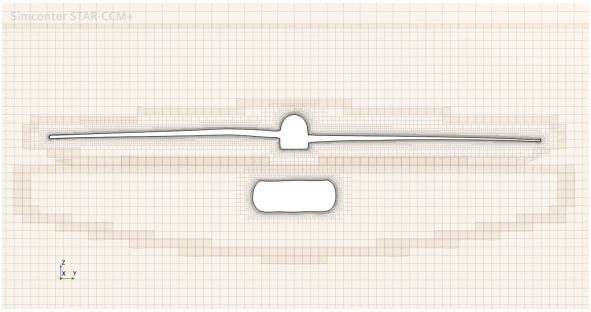

(a) Mesh for drone case view 3.

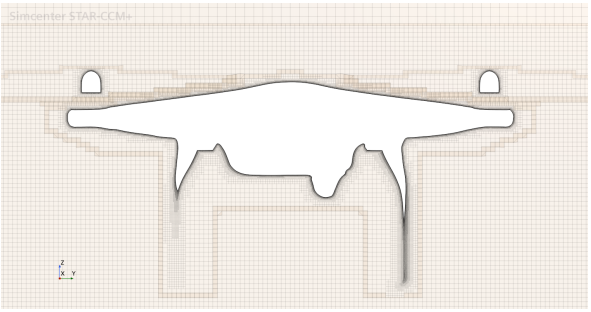

(b) Mesh for drone case view 4.

For this configuration, it has been exploited some additional functions proper of Simcenter Starccm+. Indeed, the boundary layer could have raised problems in the interfaces between:

1. Propeller and body frame;
2. Propeller and propeller.

These particular small gaps may cause errors during the hole cutting or the boundary layer description. Therefore, it has been activated additional features such as:

1. Prism layer shrinkage;
2. Close proximity;
3. Alternate hole cutting.

All these parameters are activated in the interfaces concerning propellers and body frame. These are introducing some additional steps that Starccm+ will include when changing the overset mesh. The use of these functions has been done as suggested in Starccm+ manuals [31] and in the work of [34]. In particular, with these parameters, it is possible to perform a better hole cutting process in the selected regions.
Similarly to the single propeller simulation, it has been performed a study for understanding the effect of mesh size on final results. From Table 5.6 it is clear that the mean value obtained is not affected much by the mesh value as it was for the isolated propeller. However, as in the previous case, the effect of mesh size is critical in the smoothness of the result. This last concept can be seen in the following figures

Base Size	N. cells	Single propeller mean thrust
2 e-4	14.1 e7	4.4927 N
2.5 e-4	9.7 e7	4.4613 N

Table 5.6: Convergence study of the mesh for drone case.

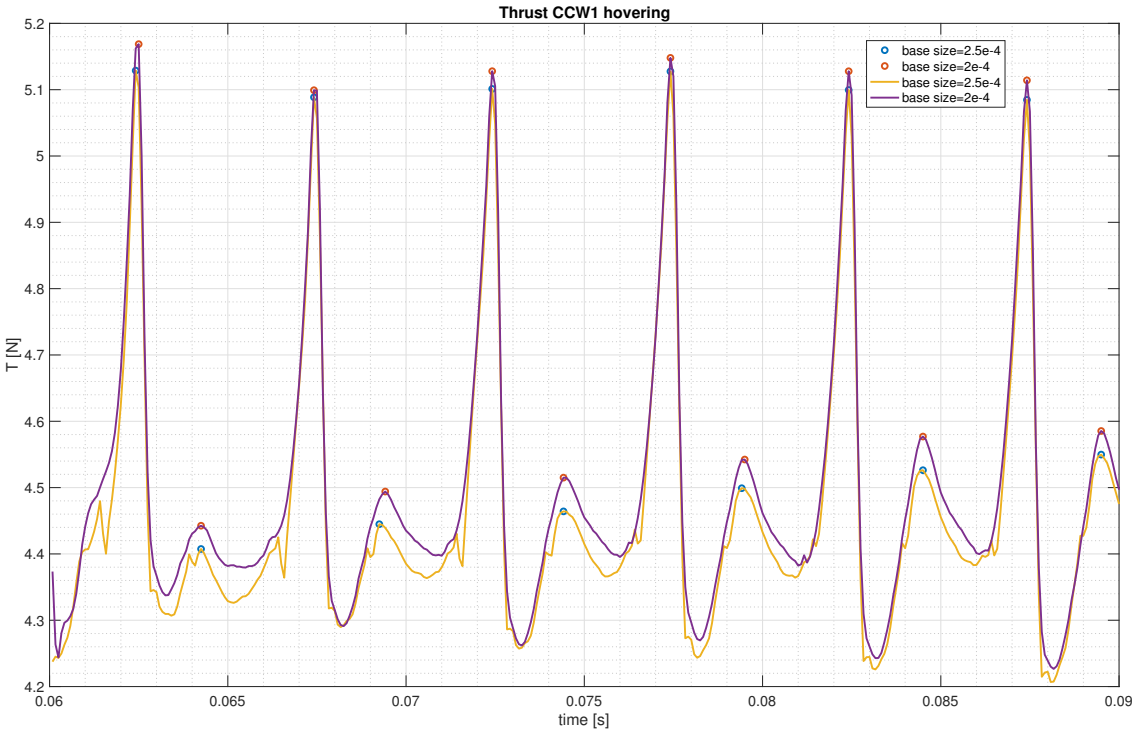

Figure 5.11: Thrust of one propeller for the drone case in hovering vs different size mesh.

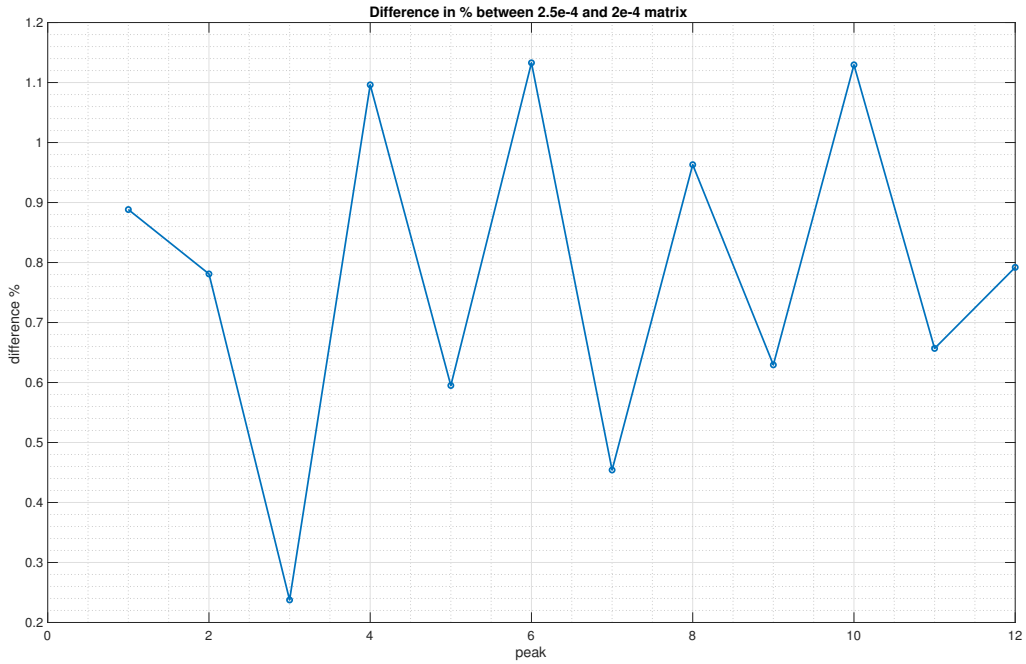

Figure 5.12: Difference between peaks levels for the single propeller in the drone case.

In figure Figure 5.12 it is clear that the difference in the peaks between the two meshes is negligible. It is important to note that the percentage is computed with respect to the mean value of the single propeller.

It is noteworthy to compare the influence of the mesh size on the simulation for the single propeller and the drone. Firstly, in both simulations, the size of the mesh is not drastically affecting the mean value of the thrust. Indeed, in both cases, the mean value is well determined moving from a base size of $2e-4$ to $2.5e-4$. On the other hand, the effect of base size on the fluctuations varies in the two simulations. For the single propeller case, the fluctuations reach very high values thus the simulation is not usable. On the other hand, in the drone case, the same increase of Base size is affecting the result in a more modest way.

5.2.2 Validation of drone methodology

In order to validate this methodology it is useful to consider the average thrust value obtained from all the propellers in the drone case. In this situation $T_{mean} = 17.91$ which is in agreement with the experimental results [33]. In addition to that, it is noteworthy the

Simulation	Average thrust for a single propeller
Isolated propeller	4.81 N
Drone's simulation	4.46 N

Table 5.7: Thrust variation for a single propeller in the isolated case vs drone case.

reduction in the average thrust generated by every single propeller. Also in this case the results are in agreement with the thrust variation described in [3]. This reduction in the average thrust and the oscillations can be attributed to the tip-to-tip and tip-to-structure interactions as described in [3].

Another interesting result can be seen in the comparison of the thrust history between the simulation with the overset mesh approach and the classical sliding interface.

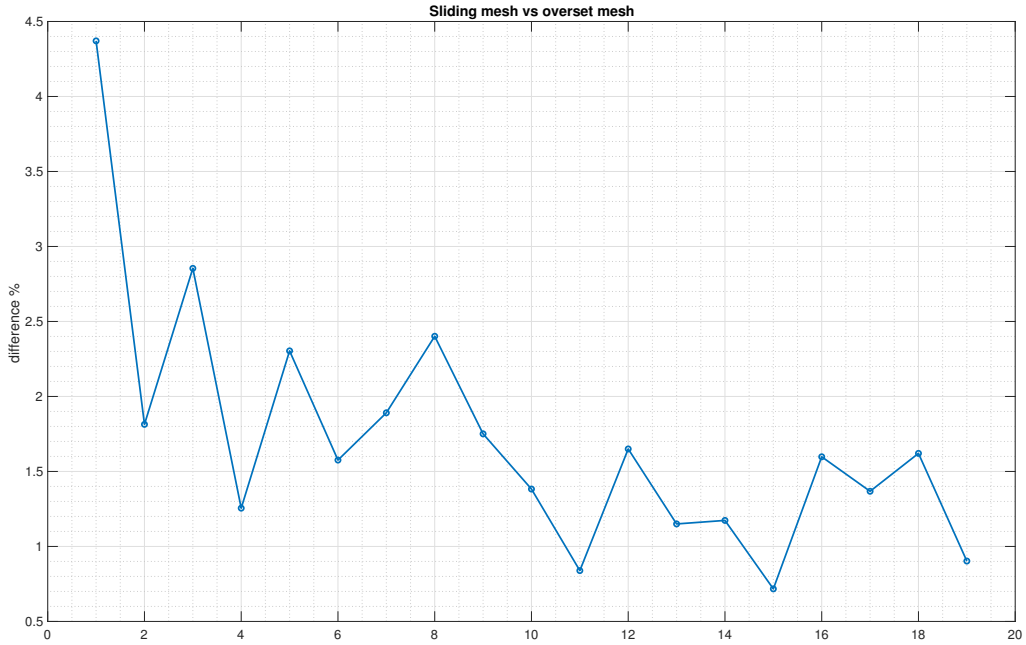

Figure 5.13: Thrust history comparison between sliding mesh and overset mesh.

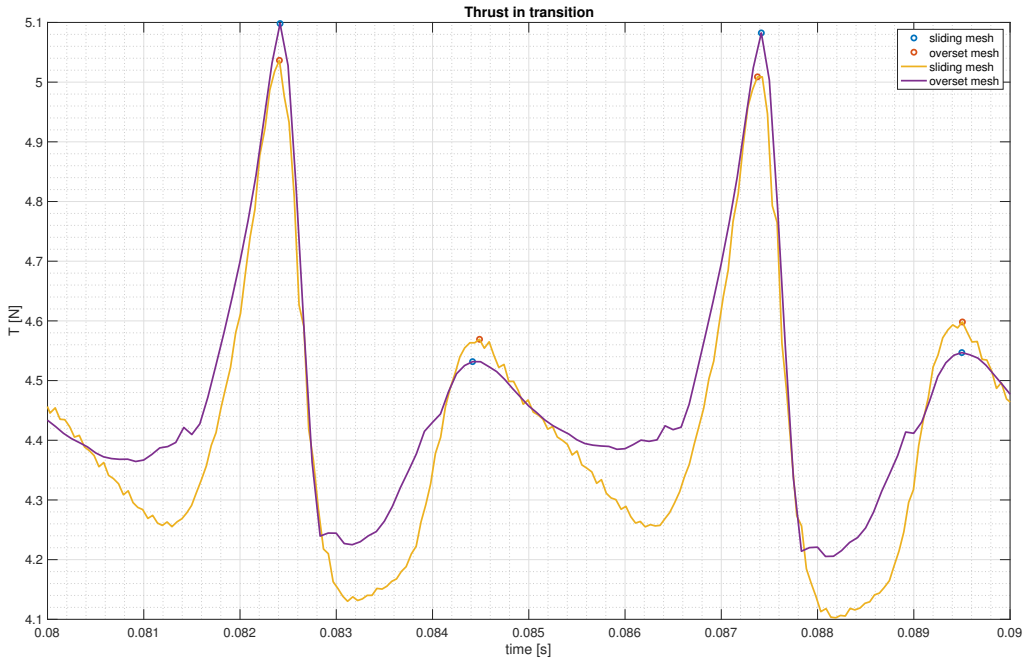

Figure 5.14: Difference in peaks between sliding mesh and overset mesh.

From these figures, it is clear that the peaks locations and the frequencies are very similar. Moreover, also the thrust peaks are very similar but the match is not perfect. This difference in values is probably due to the different mesh approaches used and the mesh size. A difference between sliding mesh and overset mesh is well documented in the literature [13]. However, it is relevant to notice a good prediction of peaks locations and frequency. In particular, the first and highest peaks is caused by the tip-on-structure interaction, while the locals minimum before and after the peak is related to the tip-to-tip interaction.

The graph reporting the difference between the peaks in Figure 5.14 shows a clear decrease that may be due to a not complete convergence of the overset mesh approach. Indeed, it is possible that with a larger number of rotations, the result would have been better.

Finally, in order to complete the validation process it is useful to consider the flow field resulting from the simulation.

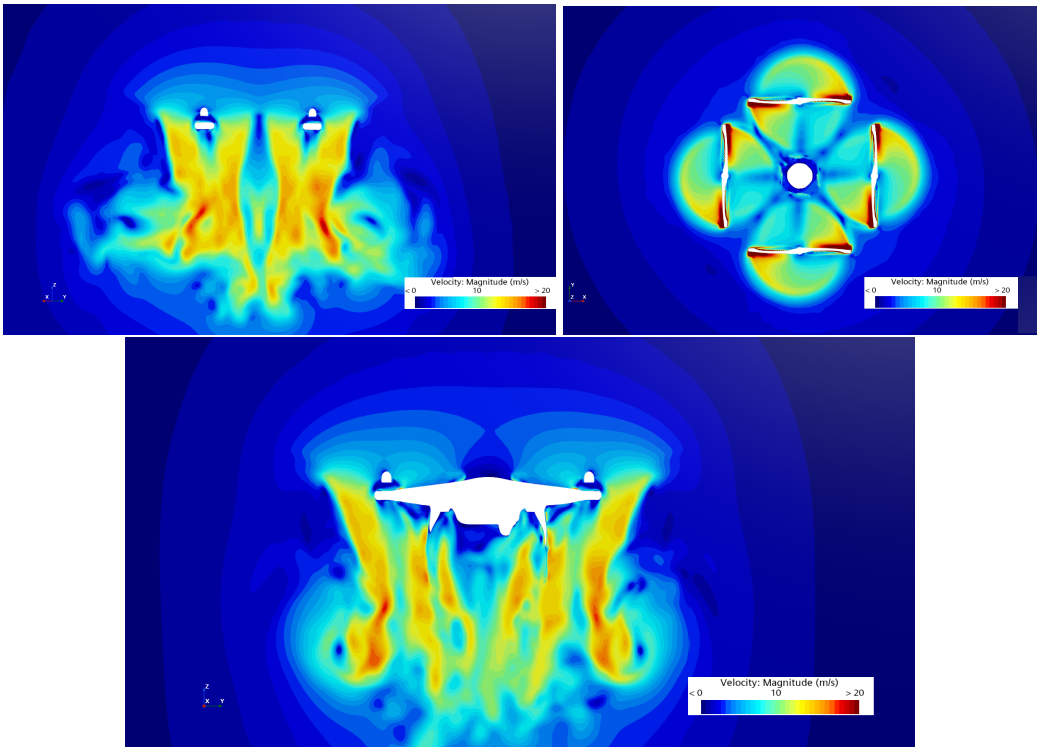

Figure 5.15: Velocity magnitude of drone in hovering.

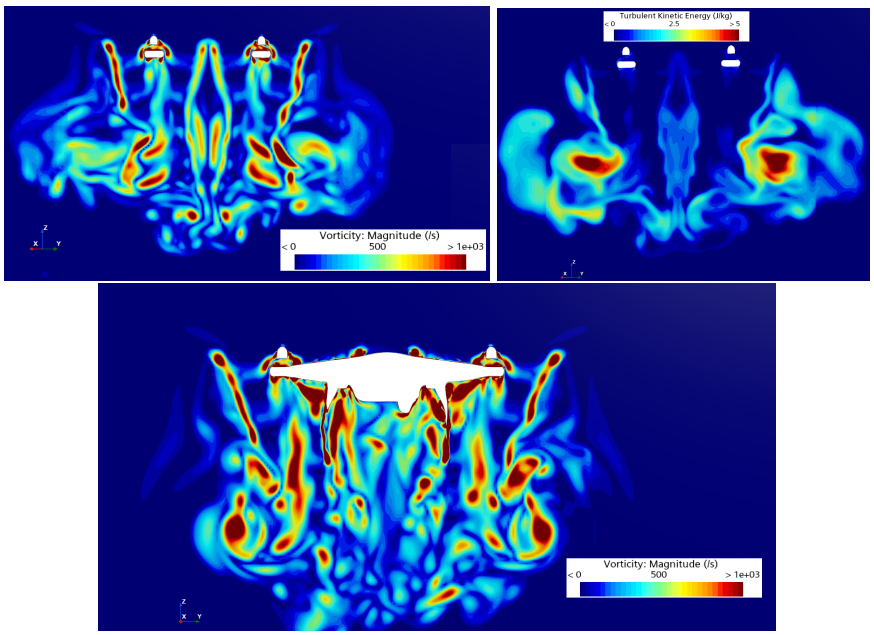

Figure 5.16: Vorticity and turbulent kinetic energy for drone configuration.

The results obtained are comparable to the one in [3]. Also in this case it is possible to notice that the flow field of each propeller is very similar to one another. However, there are relevant differences between the isolated propeller and the drone configuration. Indeed, the vorticity of the isolated propeller is symmetric between the two blades. On the other hand, in the drone case the symmetry between the blades is not very visible.

6
Transition single propeller

In this chapter, it will be described the use of the methodology earlier developed. In this case, it will be simulated as a maneuvering isolated propeller. An important part of the presentation will be the definition of the maneuver itself. Moreover, it will be explained the implementation of the motion in Starccm+.

One of the most important limits found at this stage was the validation of the results. Indeed, there are no experimental or numerical data available. Therefore, it has been implemented a theoretical 2D model, which will be described later, in order to validate the results obtained.

6.1 Transition Maneuver

During the transition from hovering to forward flight of a drone, there are three rigid body motions that are happening together [37]. Here they are described as they happen in a real case scenario:

1. The rotational speed of two propellers is reduced while the rotational speed of the other two is increased. Thus creating a thrust unbalance between the two sides of the drone;

2. This thrust unbalance will cause a tilt of the drone around one of its axis;

3. Through the tilt of the drone there will be a forward translation of the vehicle.

From this description, it is clear that in order to properly describe the maneuver it is necessary to be aware of some information such as the rotational speed change, the final tilt angle, and the total time for the maneuver. The final tilt angle was set to be 24.5. This value was obtained from an experimental study conducted at the VKI [11]. A more difficult step was the choice of the rotational speed change. It had to be estimated from the same experimental study [11]. This prediction was done through the acoustics results presented in the paper.

When a propeller is rotating, its tonal noise will present several peaks at the so.called blades passing frequency (BPF) [1]. The drone used in this study is well balanced thus, during hovering all the propellers are rotating at the same rotational speed. This will result in an SPL graph with only one peak at each multiple of the BPF. Once the peaks are clearly identified, it is possible to retrieve the rotational speed from the BPF values. During forward flight of the drone, there will be two peaks: one for the forward propellers, and the other for the backward propellers (assuming that both backward and forward propellers are rotating at the same RPM). Therefore, it will be possible to estimate the actual values of the propeller's rotational speed during the maneuver. From the study cited [11], it was possible to retrieve a value of 5580 *rpm* as the final value for the decelerating rotor and a value of 6420 *rpm* for the accelerating one. Finally, it was necessary to determine the time for the maneuver. This was estimated to be 1 *s*. However, from a numerical point of view, this would have led to a long simulation. Hence, it was chosen to set the time to be 0.5 *s* thus the total number of rotations of the propeller during the maneuver was around 50.

Once all these values were determined, it was necessary to define a function describing these variations. Since the lack of experimental results, it has been decided a function that could resemble a real case, create the simulation and eventually use some experimental results once they are available. Therefore, the functions chosen are the ones in Equation 6.4. The function resembling tilt variation can be seen in Figure 6.1
From these concepts, it is clear that the aim of this thesis was to create and validate a methodology and not the simulation of a real scenario. However, whenever possible, it has been used data coming from experimental tests. The choice of the functions describ-

ing the maneuver was initially based on the work done by a former student at the VKI and it led to the definition of:

$$\theta(t) = \frac{24.5}{1 + e^{-70t+8.9}} \tag{6.1}$$

$$\dot{\theta}(t) = \frac{1715e^{-70t+8.9}}{(1 + e^{-70t+8.9})^2} \frac{2\pi}{360} \tag{6.2}$$

$$\omega_1(t) = \left(6000 - \frac{420}{1 + e^{-70t+8.9}}\right) \frac{2\pi}{60} \tag{6.3}$$

$$v(t) = \frac{4.5}{1 + e^{-70t+8.9}} \tag{6.4}$$

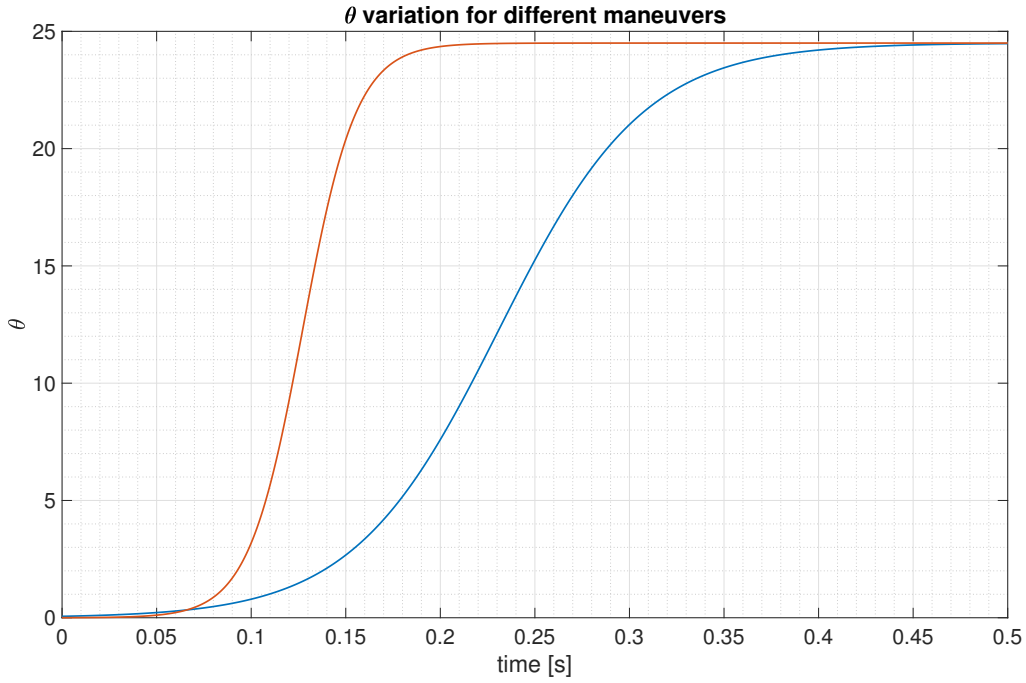

Figure 6.1: Two different functions used for the description of the maneuver.

Studying the work done at the VKI it was possible to notice that the maneuver time was reasonably estimated. However, the functions used were describing the phenomena too quickly. Therefore, the functions were changed to better describe the transition. In Figure 6.1 it is possible to see the new function used for the theta variation. The same

function has been used for the description of all other variables. In this way, the maneuver is actually happening in 0.5 s. It is still necessary to highlight that also in this case the maneuver description will have to be validated after a test campaign. However, this variation was intended to provide some results that made the acoustics methodology meaningful. Therefore, the new functions used in the simulation are:

$$\theta(t) = \frac{24.5}{1 + e^{-26t+6.5}} \tag{6.5}$$

$$\dot{\theta}(t) = \frac{637e^{-26t+6.5}}{(1 + e^{-26t+6.5})^2} \frac{2\pi}{360} \tag{6.6}$$

$$v(t) = \frac{4.5}{1 + e^{-26t+6.5}} \tag{6.7}$$

$$\omega_1(t) = \left(6000 - \frac{420}{1 + e^{-26t+6.5}}\right) \frac{2\pi}{60} \tag{6.8}$$

6.1.1 Loads in the transition maneuver

In order to better understand the phenomena occurring during the transition of a propeller from hovering to forward flight it is useful to introduce some concepts of propeller propulsion.

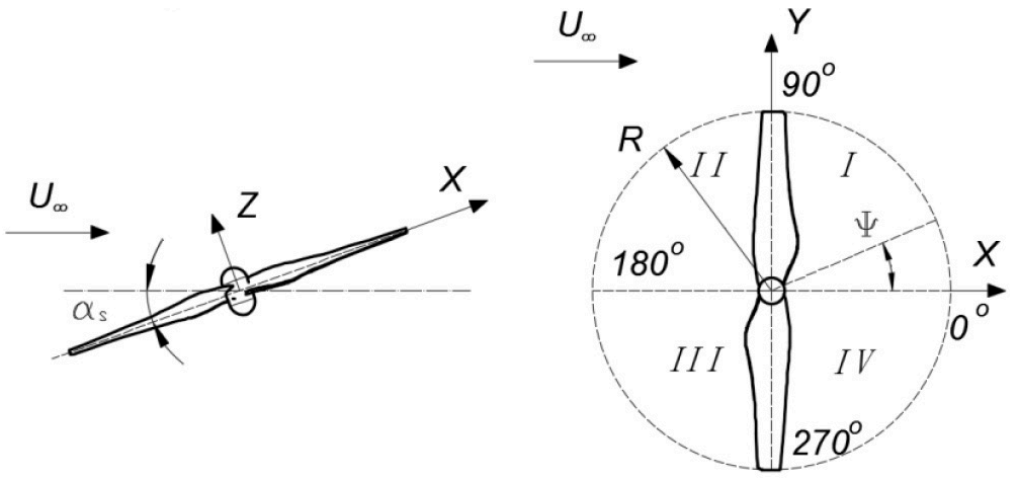

Figure 6.2: Propeller configuration during forward flight [5].

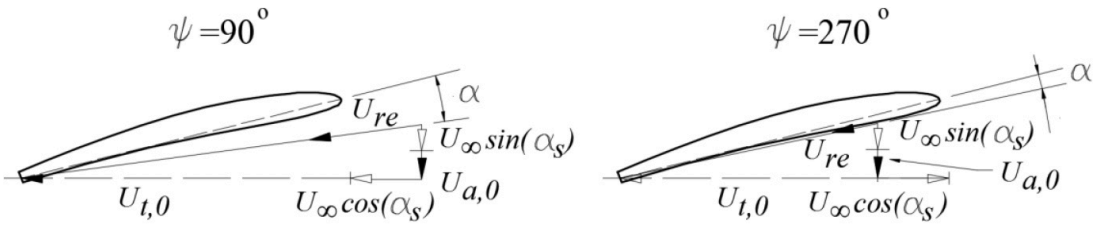

Figure 6.3: Propeller configuration during forward flight [5].

From Figure 6.2 and Figure 6.3 it is possible to understand that the main effect of the forward flight is to change the angle of attack. This change is due to the effect of U_∞ which is the advancing velocity (assuming an undisturbed environment) and the tilt angle [5]. However, it is important to note that the effect of these two phenomena is related to the azimuth position of the propeller [5]. Indeed, depending on the direction of U_∞ relative to the rotational speed U_t the angle of attack variation changes in magnitude. In particular, it is larger at $\varphi = 270°$ and smaller at $\varphi = 90°$. This load variation will result in a fluctuation of the Aerodynamic forces on the blade. The phenomena described above is present in both forward flight and transition maneuver. However, the latter is complicated by other effects which are:

1. variation in the tilt angle during the maneuver;
2. variation of the rotational speed and therefore the tangential velocity component;
3. variation in the incoming speed U_∞. Indeed, the propeller will reach the forward flight speed starting from hovering.

6.2 Analytical model

As mentioned at the beginning of this chapter, one of the main problems in this simulation was the validation of the results. Indeed, there is a lack of numerical simulations and experimental results when studying this phenomenon. Therefore, in order to better understand and validate the correctness of results coming from the CFD transient simulation it was useful to create a very simple analytical model that was able to describe the loads

variation on one blade with the change of tilt angle and the increase of advancing velocity. This has been accomplished by implementing the equations described in Figure 6.2 and Figure 6.3 for the DJI propeller.

In order to solve those equations it was necessary to compute the lift of the blade. This was accomplished through the use of Xfoil. Firstly, it was necessary to obtain different sections of the blade in order to use them in the panel method solver. This has been done by cutting the blade into 18 sections. Consequently, it has been used Xfoil in order to compute the values of C_l for the different propeller sections. The values used in Xfoil for the flow field have been computed considering the propeller in hovering. This approximation has been implemented in order to maintain the model as simple as possible. Indeed, the variations of *Re* and angle of attack are very limited. The most dominant variable variation is the change in U_∞. The complete set of data used in this model can be found in Chapter 10.
Once the C_l values have been obtained it has been possible to compute the lift variation during the maneuver $L = 0.5 \cdot \rho \cdot U^2 \cdot C_l \cdot Area$.

During the maneuver it has been computed the new velocity which is defined as $U_{\text{ref}} = \sqrt{(\omega \cdot R_i + U_\infty \cdot \cos(\alpha_S) \cdot \sin(\psi))^2 + (U_\infty \cdot \sin(\alpha_S))^2}$. Hence, it is possible to compute the new thrust with all the components just computed. In figure Figure 6.6 it is reported the result obtained.
As mentioned before, this model was intended to understand how the loads are going to change during the transition. Moreover, it was useful to understand if the CFD simulation was providing reasonable and meaningful results. However, it is necessary to highlight which are the main limits of this analytical model:

1. It is using the 2D ideal model;

2. There is no presence of induced velocity and 3D effects.

3. Here Lift and Thrust are used as synonyms thus it is a strong limitation. Indeed, the thrust should be accounting for the induced drug effects and for the inclination caused by the $U_\infty \cdot sin(\Phi)$. However, this last effect is negligible since the Y-component is much smaller than the tangential one. Therefore, the influence on the Lift direction is limited.

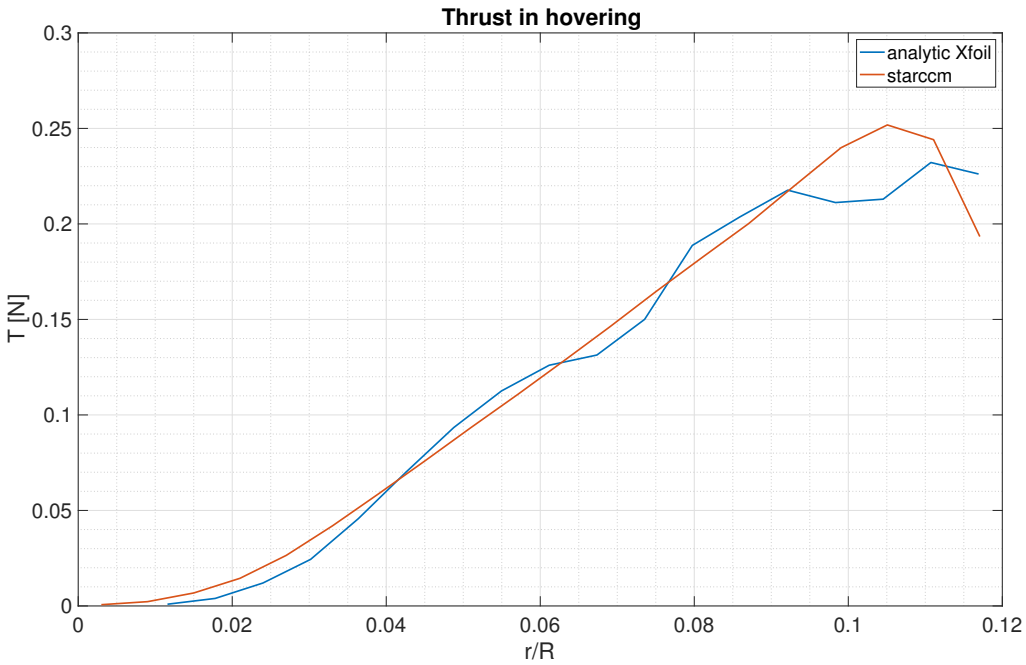

Figure 6.5: α and Lift distribution during hovering.

In order to compare the analytical model results with the ones coming from the CFD simulation it has been necessary to extract the thrust history from Starccm+ using the Force Accumulated tables. This extraction method required the definition of a number of strips and their direction of integration as reported in Figure 6.4.

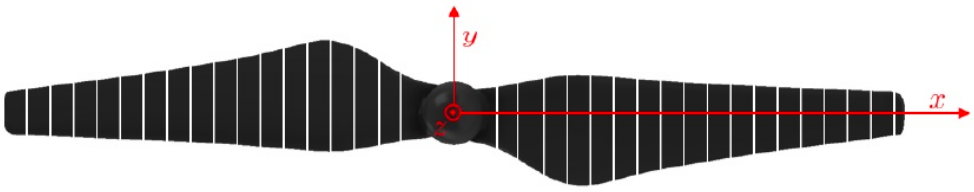

Figure 6.4: Example of blades stripping.

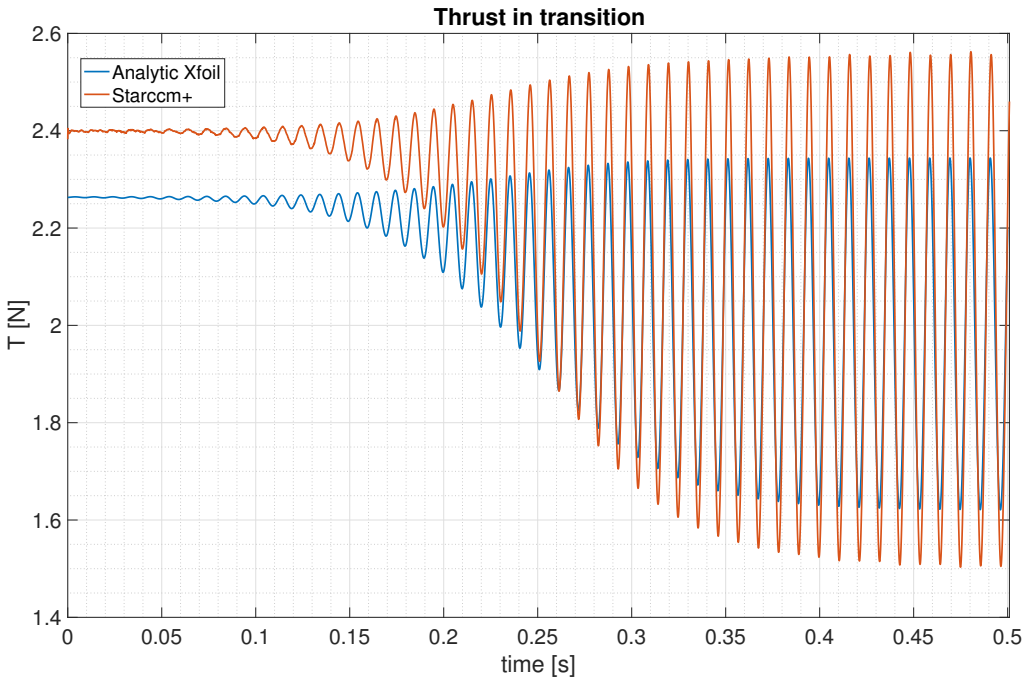

Figure 6.6: Thrust variation during the transition maneuver using both the analytical model and Starccm+

From Figure 6.6 and Figure 6.5 is clear that the approximation coming from the analytical model is well describing the overall pattern of thrust during the maneuver. Indeed, the maximum difference between the two results is around 13%. This is quite a noteworthy result considering that the analytical model is using a very simple 2D implementation, while, the result coming from CFD is based on a 3D. From Figure 6.5 it is evident that the main difference is close to the tip of the blade. Thus, confirming that the main difference is coming from unresolved 3D effects.
Another result confirming the good match between the two is the fact that the frequency of thrust variation is identical between the two sets of results. Indeed, the change in lift force is driven by the change in RPM.

6.3 CFD simulation

6.3.1 Simulation set-up

The simulation set-up was identical to the hovering configuration already described in the methodology. It was only necessary to introduce the motion definition. As explained ear-

lier the maneuver consists in the superimposition of three rigid body motions. Therefore, it was defined in Starccm+ considering the three different maneuvers. Starccm+ provides the possibility to define rigid body motions with several levels of dependency [31]. In particular, it was more convenient to start from the translation, define the tilt, and then the rotation of the propeller around its own axis. In this way, the software was handling the reference frames easier. Although this is not providing a real description of phenomena, since they are processed at the same instant of time, it is not relevant to the actual order. It is noteworthy the fact that this definition was done for both the propeller region and the wake region. However, in the case of the wake, there was no spin motion.

The definition of the maneuver in Starccm+ has been done following these steps:

1. Definition of the field functions describing the change of velocity, RPM, and tilt angle;

2. Definition of three different reference frames: each one of them is nested within the other one. Indeed, the first is the one used for the definition of the translation (equal to the Laboratory reference frame). Nested in this reference frame it has been defined one for the tilt of the propeller. This reference frame will be translated without any rotation. The last one is the set of axis used for the propeller rotation around the z-axis. This reference frame is both translating and tilting with the propeller.

3. The final step was the definition of three different maneuvers. As mentioned the first one was the translation followed by the tilt of the propeller and finally the change in RPM. In the definition of these maneuvers it was necessary to provide:

    (a) Functions describing the time domain variation of the maneuver;

    (b) Reference frame where the maneuver is happening;

    (c) Reference frame that had to be managed by that maneuver. This is defining which reference frames will have to change during the maneuver.

6.3.2 Simulation results

In this section, it will be presented the fluid dynamics results coming from the CFD simulation. Thrust variation history has already been provided for comparison with the analytical model thus, it will be presented the flow field resulting from the simulation.

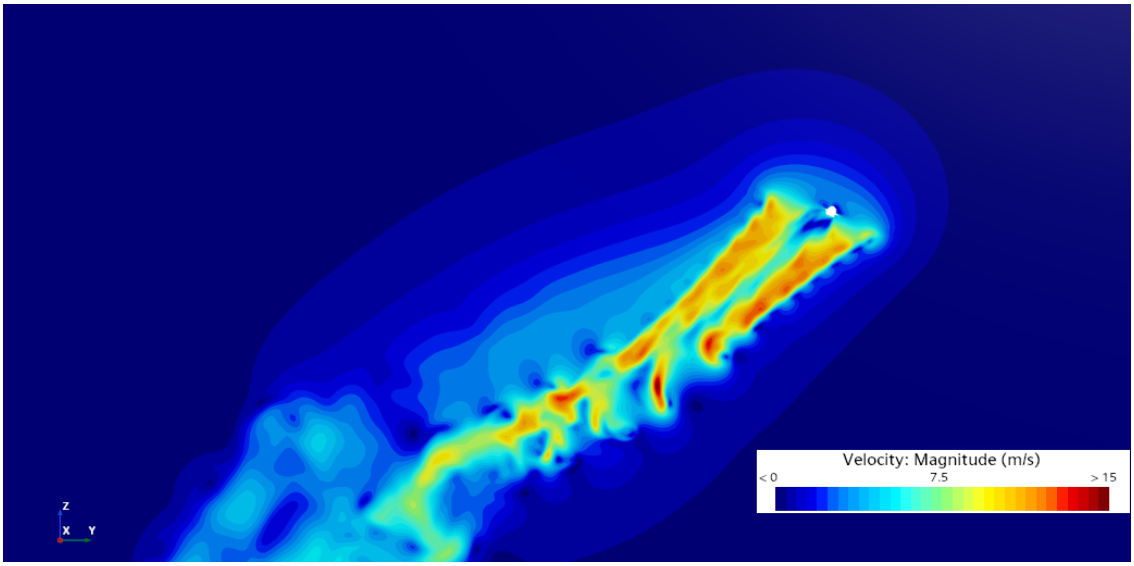

Figure 6.7: Velocity magnitude for the transition of the propeller.

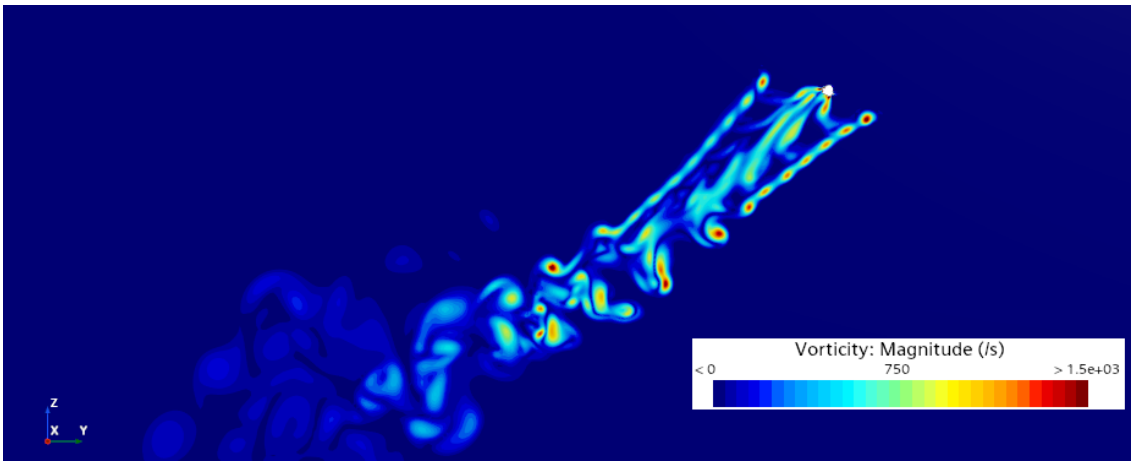

Figure 6.8: Vorticity magnitude for the transition of the propeller.

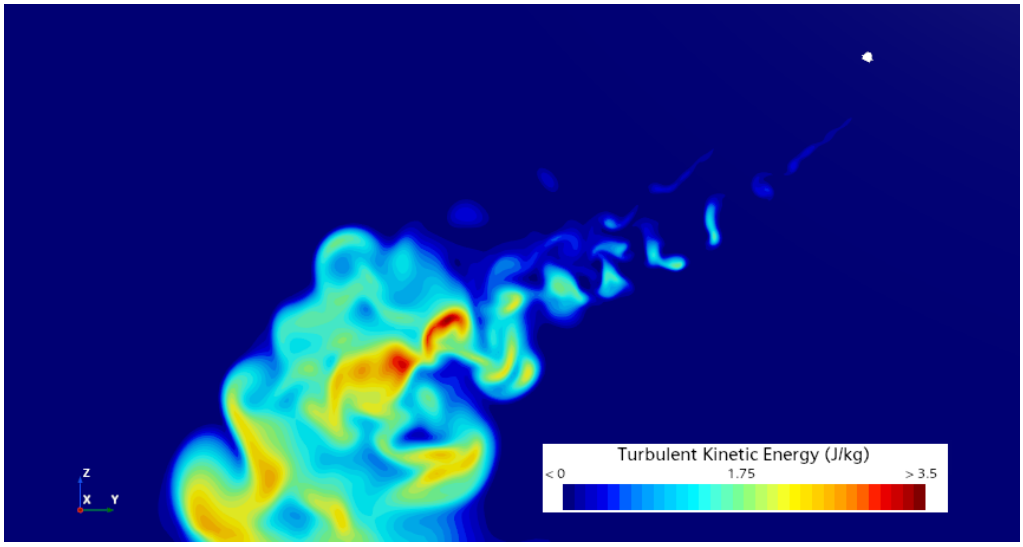

Figure 6.9: Turbulent kinetic energy for the transition of the propeller.

From Figure 6.7 it is possible to notice that there is still a considerable level of symmetry between the two blades. However, it is not as clear as in the hovering case. Indeed, blades are not facing the same flow condition. On the other hand, looking at Figure 6.8 it is clear a higher level of vorticity for the propeller in the advancing position. These peaks coincide with larger values of velocity magnitude. The Turbulent kinetic energy magnitude still dominates in the wake far away from the propeller and it is almost negligible in the proximity to the propeller.

6.3.3 Validation of CFD results

The first validation step was the comparison with the analytical model. Another validation analysis consisted of the simulation of the propeller in the forward motion. Consequently, the forward flight configuration was confronted with the last rotations of the transition in order to understand if the end of the maneuver and the forward flight are matching (see Figure 6.10). For the forward motion simulation, it was used the domain of the hovering with some changes:

1. Boundary conditions: It was used the ”Freestream” boundary condition as suggested in the Starccm+ manual. Here it was necessary to provide: Mach number, Temperature, and Pressure in order to impose the speed of $v = 4.5\ m/s$ in the -Y direction;

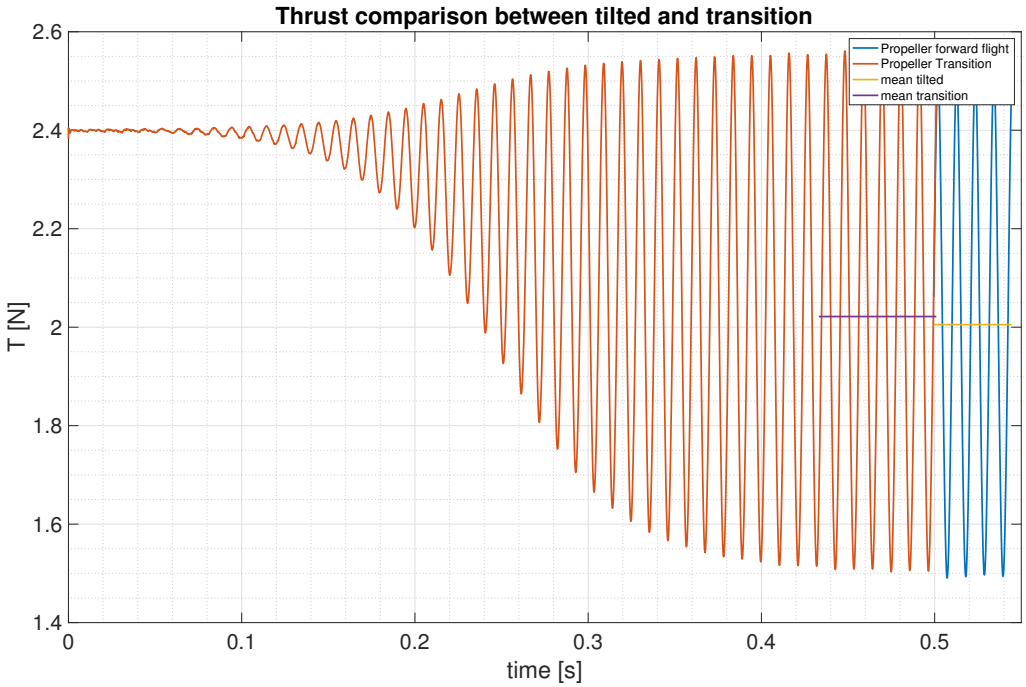

Figure 6.10: Thrust computed with the tilted propeller in forward motion and Thrust coming from the transient simulation.

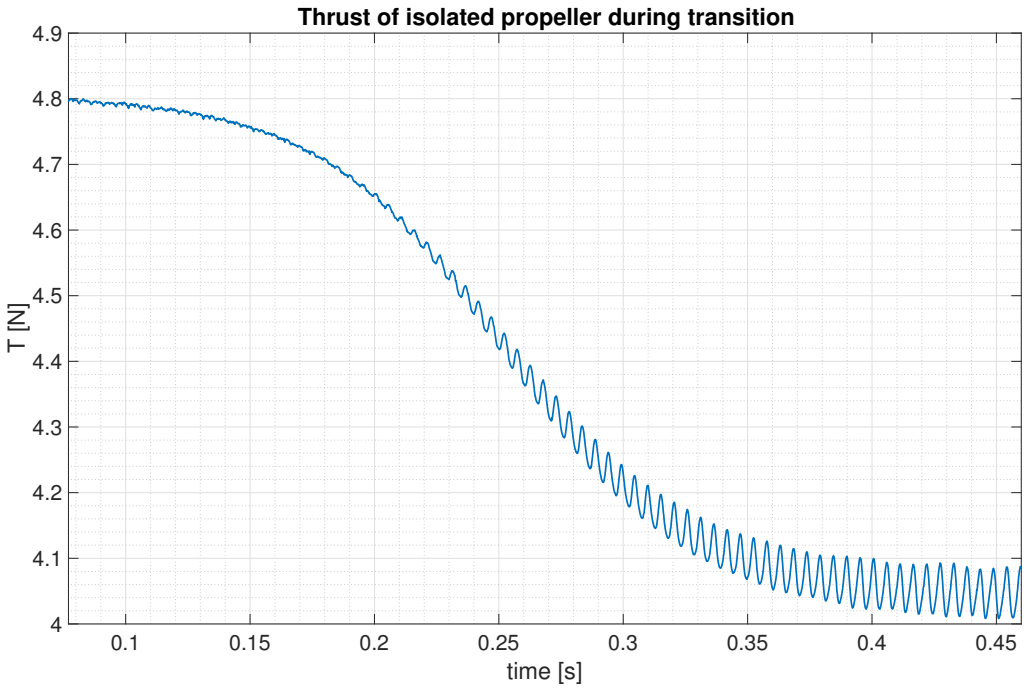

Figure 6.11: Turbulent kinetic energy for the transition of the propeller.

2. The propeller was tilted as well as the wake domain to the angle of 24.5 deg;

3. The propeller rotational speed was decreased to 5580 *rpm*.

All the other settings have been left identical to previous simulations. Since the comparison with the analytical model has already been made, it will be discussed only the comparison with the tilted simulation.

The transient simulation is providing the same results obtained with the tilted unsteady simulation. From Figure 6.10 it is clear that there is not a perfect match between the two cases. This difference is possibly due to the difference in boundary conditions applied. Moreover, in a transition maneuver, it is possible to have an accumulation of errors that in the end may cause the difference present in the figure [29]. In the tilted simulation the mean value computed is $T_{mean} = 1.9873\ N$ while for the transition it is $T_{mean} = 2.0217\ N$. Therefore, there is a difference of 1.7 $\%$. Thus, the difference although present is very limited. The frequency of thrust variation is identical.

In conclusion, it is possible to say that the unsteady maneuvering simulation seems to be well describing the transition. Indeed, it is providing results that are in good agreement with results obtained in different ways. Once more, it is important to highlight the fact that this is just a hypothetical maneuver and it was done in order to validate a methodology. So that, once the maneuver is properly defined, it is possible to perform a more accurate CFD simulation.

7

Drone's maneuver simulation

In this chapter, the fluid dynamics simulation for the maneuvering drone will be provided. It will be presented the simulation set-up and the discussion of the results.

7.1 Maneuver definition in Starccm+

In this section, it will be described the implementation of the maneuver in Starccm+. Indeed, the definition of this maneuver was crucial for the simulation and it will be necessary for future work on this project at the VKI, thus some time has to be spent on its description. The motion definition has to be implemented using two different paths in parallel. It will be slightly different than the one used for the single propeller because it has to be guaranteed the rigid body motion of all the regions. The first process concern the coordinate system definition. Indeed, in the Laboratory coordinate system (the main one) it has to be introduced a new coordinate system for the maneuver. This was defined in such a way that the drone was moving with the camera package on the back.

1. Reference frame for maneuver: this is centered in the laboratory frame and has to be rotated at 45 deg. In this way, the y-axis is now aligned in the transition direction. This will be useful in the transition definition.

    (a) Nested in this reference frame there is a local coordinate system that consist in one reference frame for each propeller and a reference frame for the wake and the body of the drone.

i. Nested in the wake and body frame reference system there is still a local coordinate systems that consists in: one reference frame for each propeller and a reference frame for the wake and the frame of the drone.

The necessity for nesting all these reference frames is due to the way in which Starccm+ operates during the motion definition. The second process consists on the definition of the motion. The motion has to be defined in the following way:

1. Firstly, it is defined as the transition. Here, it is introduced the velocity in the y direction Equation 6.4 with respect to the first reference frame defined. Moreover, it has to be defined a "Managed coordinate system". This consists of the coordinate systems that the software has to move during the motion-defined. Therefore, here it is necessary to introduce all the nested coordinate systems at point 1. In this way, during the transition, all the coordinate systems will be moved.

   (a) At this point, it is defined the tilt maneuver. It will be nested in the previous maneuver. Here, it is necessary to define the coordinate system that is the one in output from the previous motion, together with the managed coordinate system. Also here the managed coordinate system is the same as before. In this way, all the coordinate systems are tilted during the maneuver.

      i. Finally, it is defined as the spinning of the different propellers. Here, the reference coordinate systems are the one of each single propeller that has been carried during the previous maneuver. At this point, there are two main aspects to consider. Firstly, two propellers are rotating in a clockwise direction, thus the rotational speed has a minus sign in front. Secondly, two propellers are increasing the rotational speed while the other two are decreasing it. Therefore, it is necessary to change the sign in Equation 6.3.

7.2 Mesh study for the maneuver

Since the drone's maneuver is computationally demanding, it has been performed a first simulation with a very fast maneuver. This simulation was performed with a coarse mesh

in order to understand if it was possible to run the actual case with this mesh. In particular, the mesh was performed with a base size $2.5e-4\ m$. In this way, it was also possible to test if the maneuver was correctly described and in general if the simulation converged without divergence of residuals.

The functions used were the ones introduced for the single propeller but with a much faster speed. The simulation ran without any divergence of the residuals. However, here it will be reported only the Thrust history. Indeed, it is the one providing the most significant results.

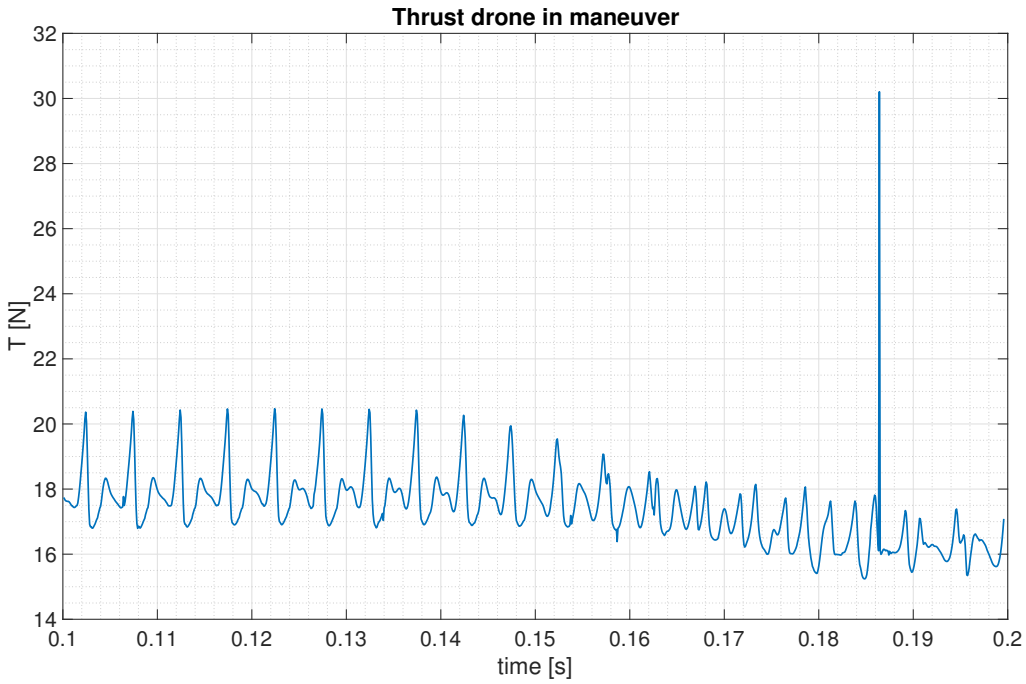

Figure 7.1: Overall thrust history for the drone during fast maneuver with a coarse mesh.

From Figure 7.1 it is possible to see some very interesting behaviors:

1. The overall thrust presents some strange peaks that have no physical meanings. This behavior is very similar to Table 5.5. Therefore, this explains the choice for a finer mesh in the case of the actual maneuver.

2. The frequency seems to lose any sort of periodicity after half of the maneuver.

3. The average value of thrust is decreasing. This behavior is quite surprising since it is not expected to have a decreasing overall thrust. Indeed, the implementation of

the motions and the settings of the thrust are correct, a possible explanation for the decrease is that the values used in the functions of the propeller's rotational speed are not correct. Indeed, a decrease in thrust would lead to a decrease in altitude of the drone.

At this point is was possible and meaningful to test the finer mesh. It has been used the same maneuver used for the coarse case. For this test the base size used was $2.5e-4\ m$

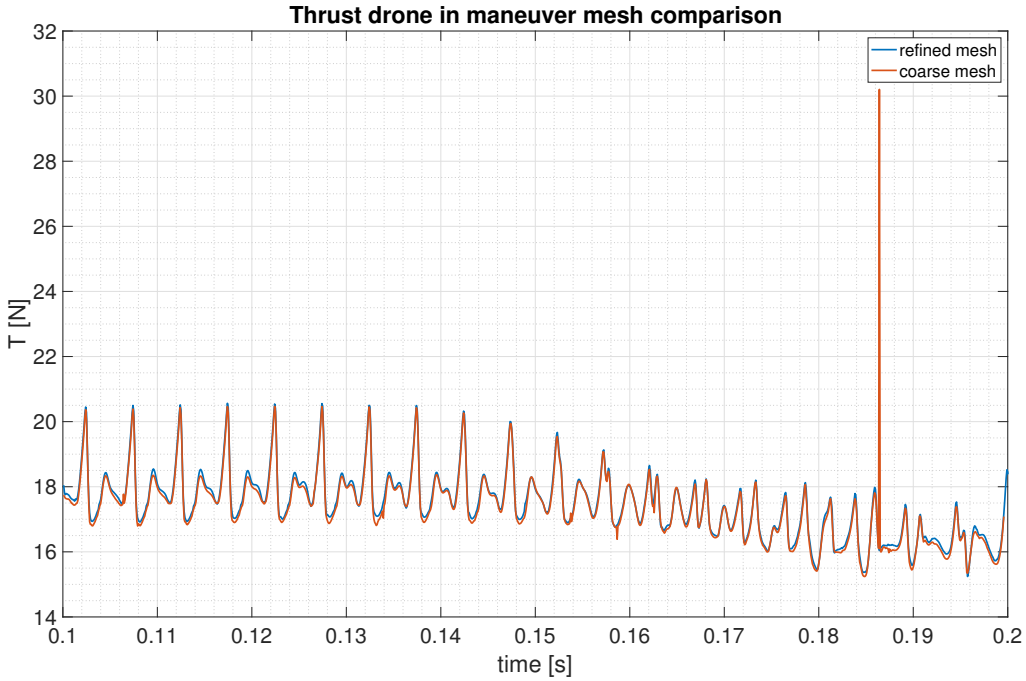

Figure 7.2: Thrust history comparison for the drone's maneuver using two different mesh refinement.

From Figure 7.2 it is clear that the mesh size is affecting the thrust results. However, the main effect is evident in the absence of the unique and dominating peak. On the other hand, it is evident that the overall thrust trend is very well described even using the coarser mesh. The actual maneuver will be left for future work since it is highly cost-effective from a computational point of view. Therefore, it will not be used for this thesis.

In the following, the analysis will be limited to this faster maneuver in order to underline the main results obtained. The number of cells for the two meshes is reported in the methodology description.

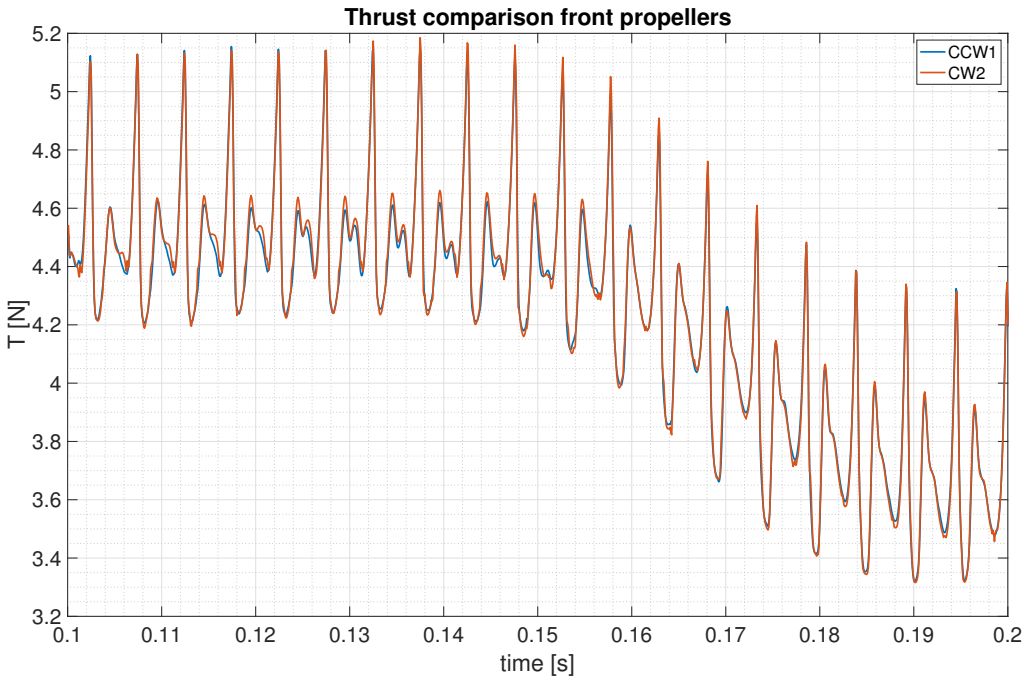

Figure 7.3: Thrust history comparison between two propellers in front of the drone. Therefore, the propellers that are reducing the rotational speeds.

7.3 Results presentation and discussion

In this section, there will be a presentation of the results obtained in the maneuvering analysis of the drone. All the following data are referred to the refined mesh with the use of a fast maneuver. Firstly, let us consider Figure 7.2. Here it is clear that there is no periodic pattern in the thrust history. In order to better understand this graph it is useful to analyze the thrust history of each single propeller. From Figure 7.3 there is a clear decrease in the thrust. It is possible to observe some noteworthy behaviors:

1. Both propellers are producing a very similar thrust history;
2. in the first half of the maneuver, there is no relevant variation in the thrust behavior with respect to the hovering condition. This almost unvaried behavior is really peculiar if considering that the main variables (forward velocity and tilt angle) are already at half of the variation. The main difference is located in the second and smaller peak of the thrust;
3. During the thrust reduction (starting from half of the maneuver) the peaks amplitude and frequency is not changing except for the smaller set of peaks that are increasing

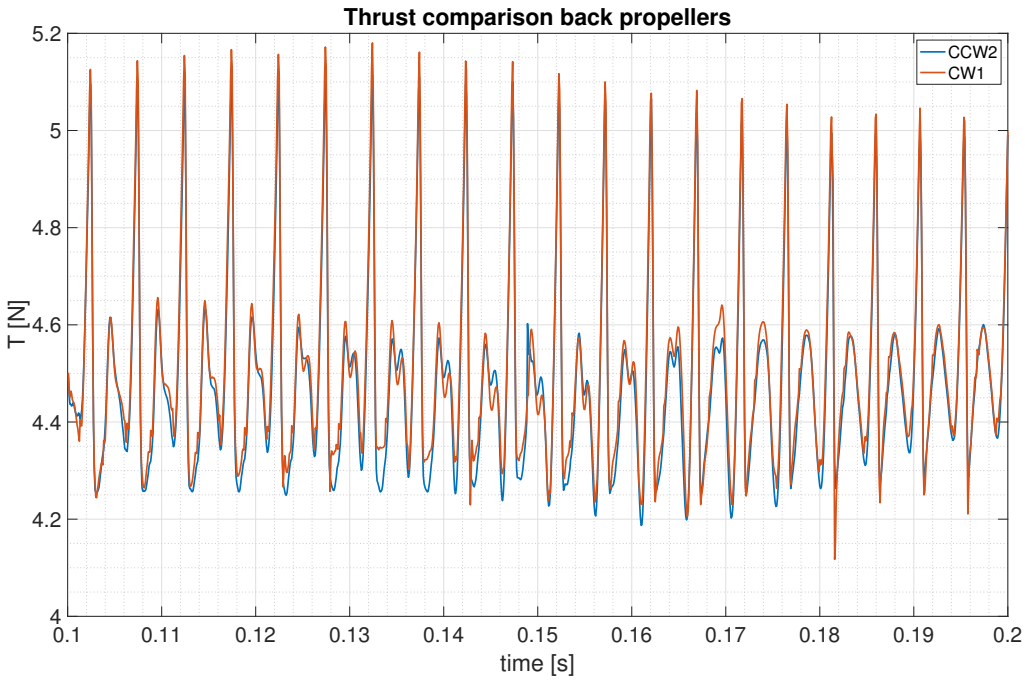

Figure 7.4: Thrust history comparison between two propellers in back of the drone. Therefore, the propellers that are increasing the rotational speeds.

in amplitude.

The second point is suggesting a relevant delay in the thrust variation of the front propellers. A completely different behavior is observed in Figure 7.4. Indeed, for the backward and accelerating propellers, it is possible to observe:

1. A larger difference between the two propellers;

2. An earlier variation of peaks during the maneuver.

3. The most interesting result is that the increase of the thrust on the back propeller is not visible. Indeed, it looks like there is a decrease in the thrust.

Another interesting way to investigate the last behavior described is to look at the average thrust on each propeller.

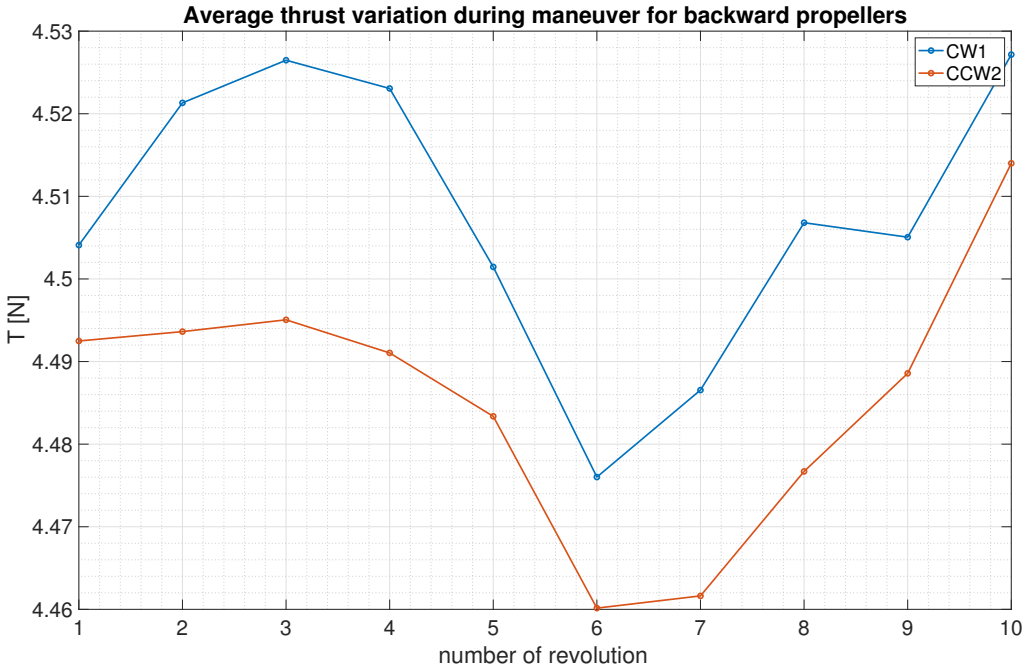

Figure 7.6: Average thrust of forward propellers.

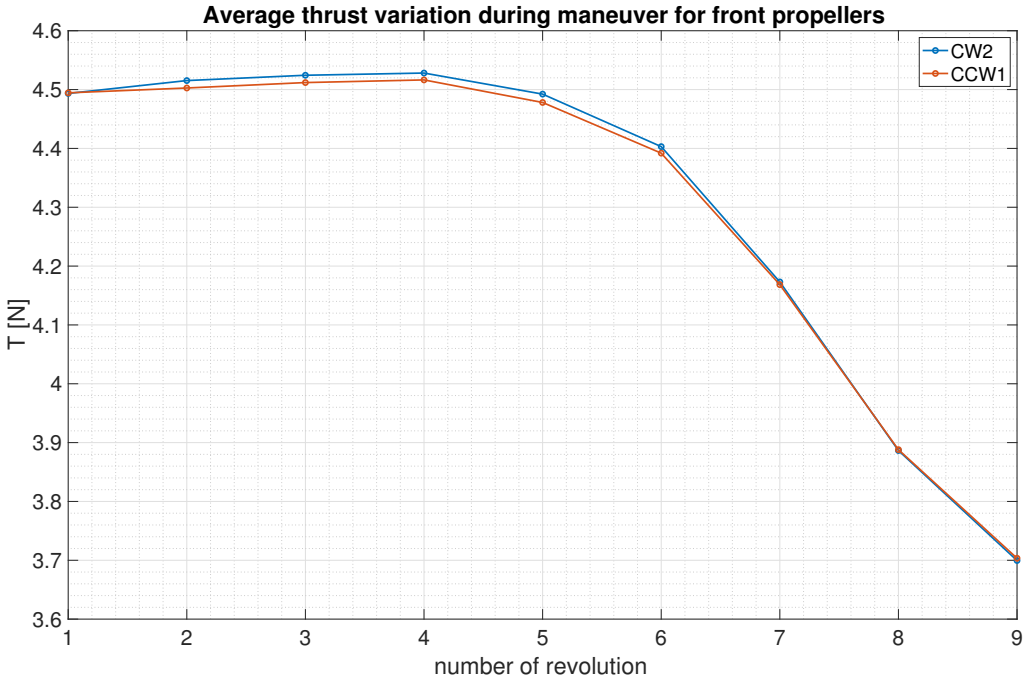

Figure 7.5: Average thrust of backward propellers.

From Figure 7.5 it is very evident the peculiarity of the thrust history on backward

propellers. Indeed, they are producing an initial increase in thrust, followed by a decrease and eventually another increase in thrust. This interesting result has to be investigated but it is probably related to some aerodynamic interactions between the flow field coming from the front propellers. Similar behavior has been observed in [38] in the study of a drone in forward flight.

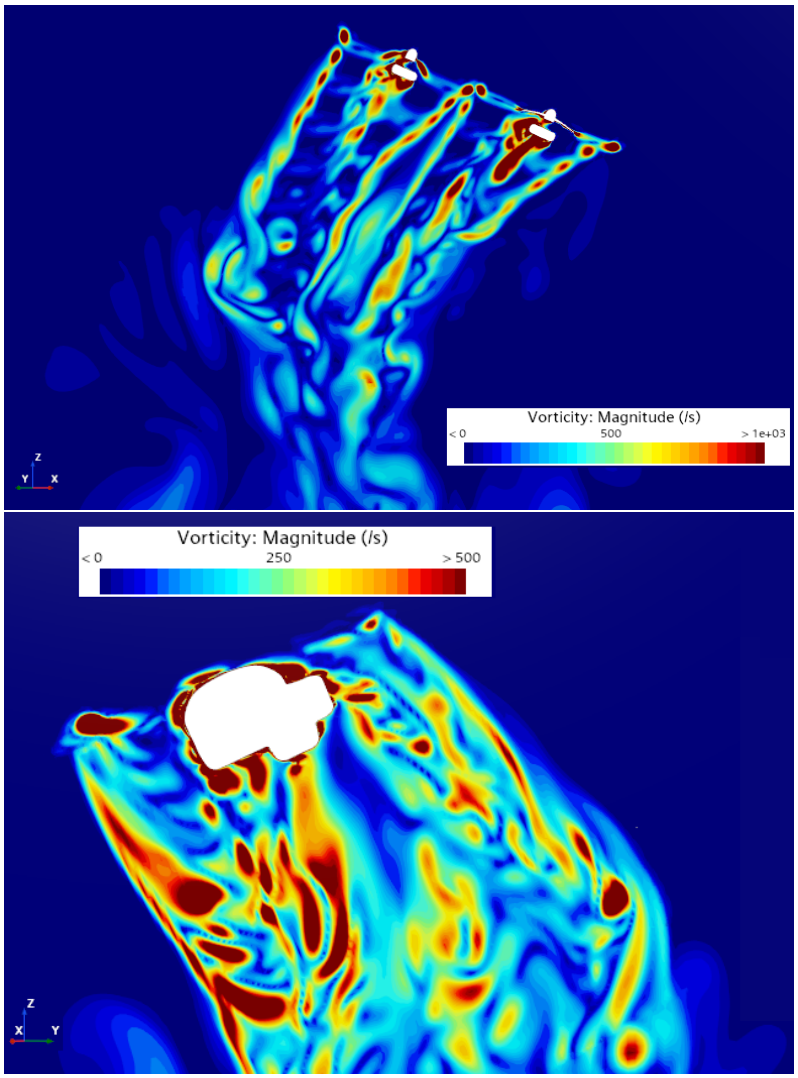

Figure 7.7: Vorticity magnitude of drone at the end of maneuver.

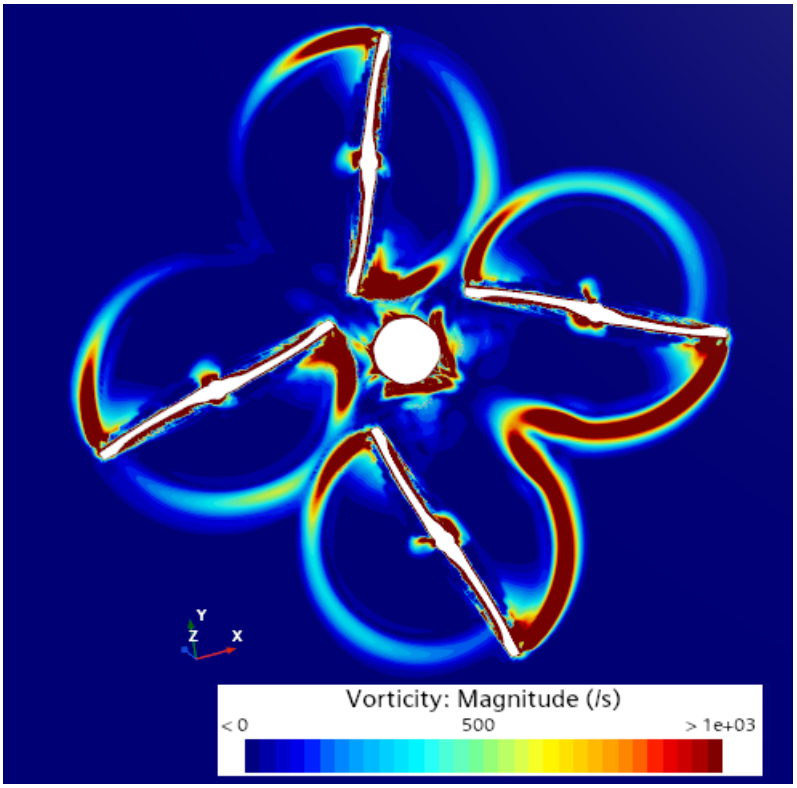

Figure 7.8: Vorticity magnitude of drone at the end of maneuver.

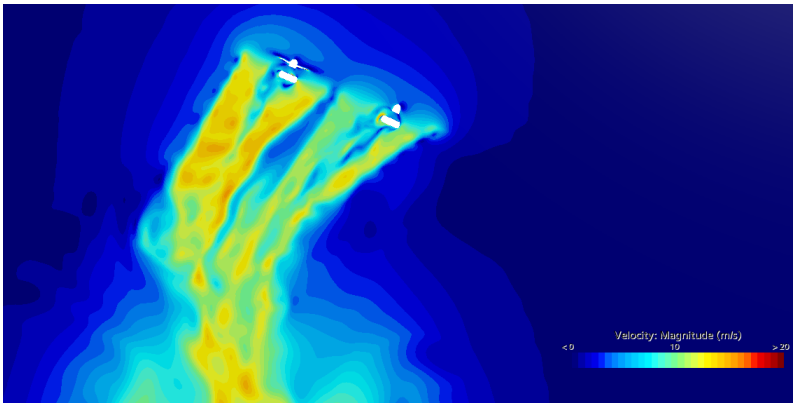

Figure 7.9: Velocity end of maneuver for the drone configuration.

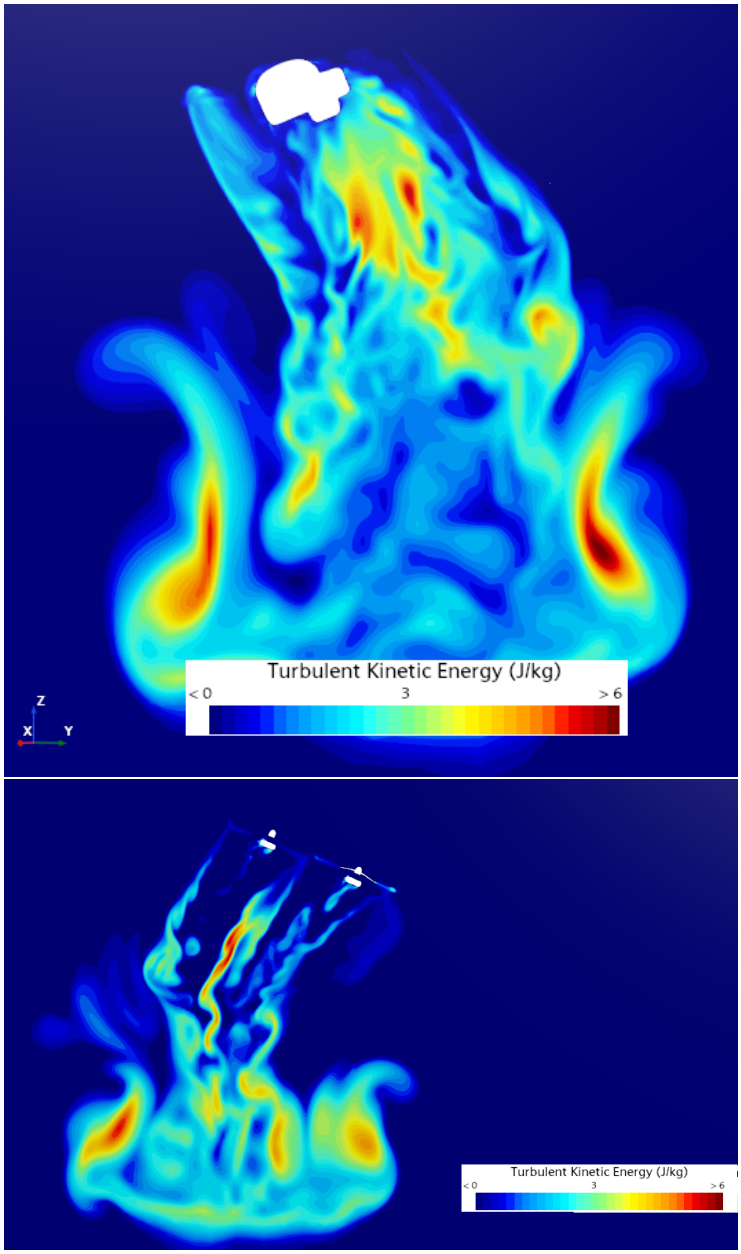

Figure 7.10: Turbulent kinetic energy end of maneuver for the drone configuration.

It is very interesting to compare the figures in Figure 7.10, Figure 7.9, and Figure 7.8 to the one for the hovering configurations. Very interesting information can be obtained from the vorticity images. Here it is noteworthy the increase in vorticity on the side of the drone that is moving toward the air. This is very clear in the image reporting two propellers. Indeed, under the body frame of the front propeller, it is possible to see

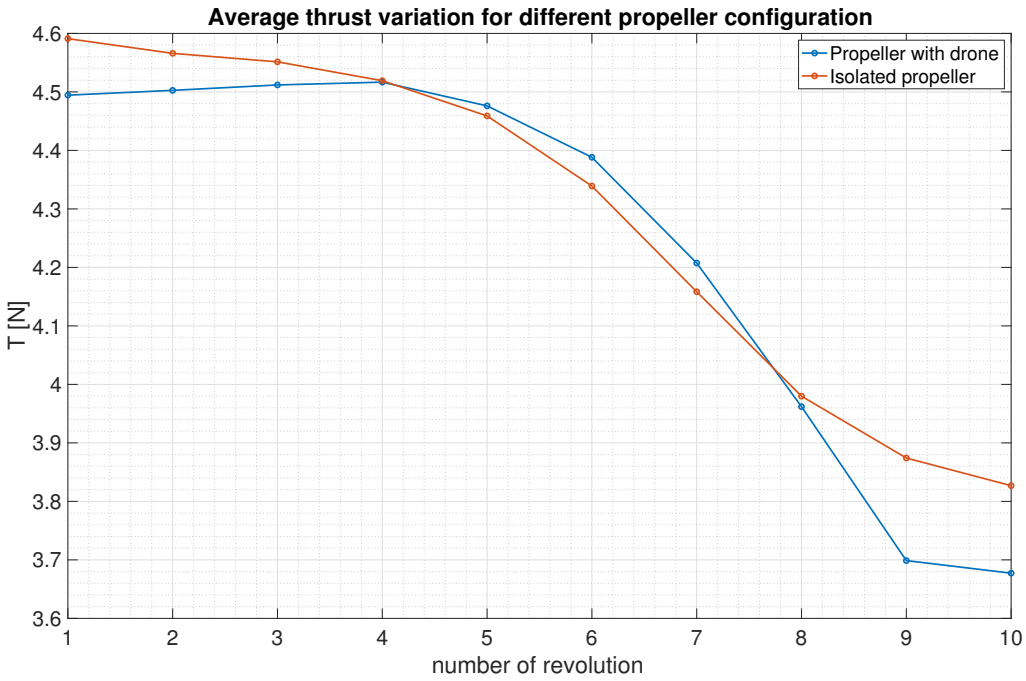

Figure 7.11: Average thrust comparison between single propeller and drone. The comparison is has been made for the decelerating propeller.

a larger vorticity area compared to the one on the back. Moving to the second set of figures Figure 7.8 it is possible to notice a larger turbulent zone under the two propellers that was not present in the isolated propeller. Therefore, the interaction of the propellers and body frame are causing a larger turbulence. Finally, it is interesting to see that the front propellers undergo a relevant fluid distortion with respect to the isolated propeller meaning that there is a loss in the symmetry between the two blades. On the other hand, the propeller in the back seems to be less affected by the maneuver.

7.3.1 Isolated propeller and drone comparison

In this section, it will be compared the results coming from the isolated propeller and the propellers in the drone. This was done considering the same quick maneuver and the same mesh configurations (Base Size=2e-5). It has already been stressed that this maneuver is not a real one. However, it is interesting to compare these results. From Figure 7.13 it is possible to notice that the average thrust changes in a very peculiar way. Indeed, during the initial and final steps of the maneuver, the behavior is consistent with [3]: the isolated

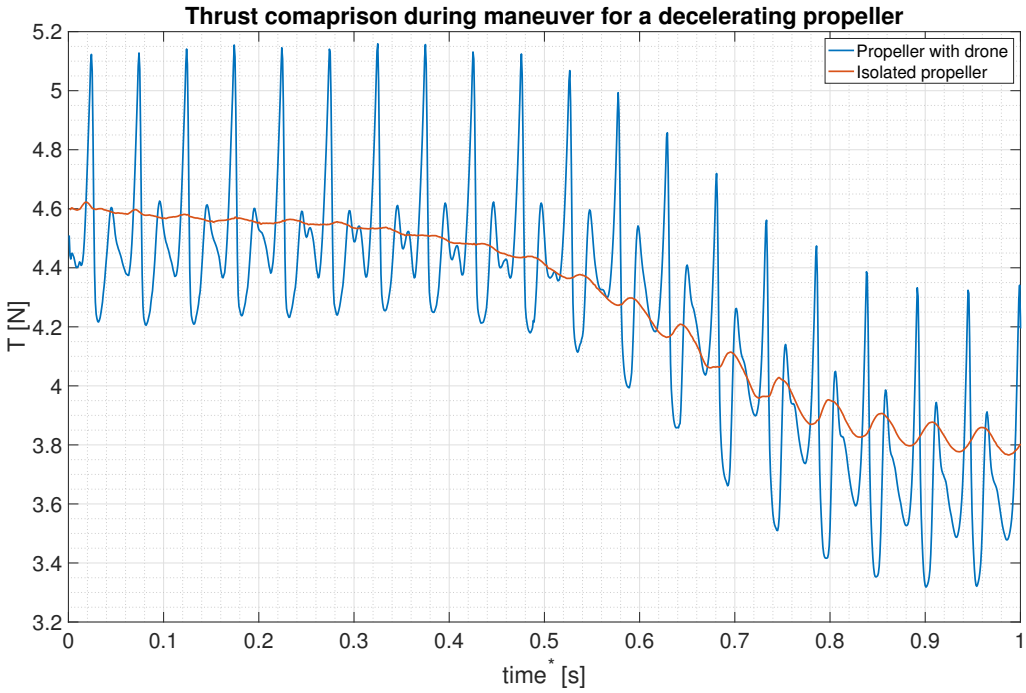

Figure 7.12: Thrust history comparison between single propeller and drone. The comparison is has been made for the decelerating propeller.

propeller is providing larger thrust with respect to the drone configuration. On the other hand, in the middle of the maneuver, the opposite is happening. In Figure 7.14 the thrust time history comparison is provided. The thrust coming from the isolated propeller undergo smaller fluctuations due to the absence of tip-tip and blade-body interactions [3]. The same comparison has been performed for the accelerating propeller. As expected, the behavior of the two propellers is completely different. Indeed, already from the previous discussion it emerged that considering the accelerating propeller in the drone configuration it was possible to witness a relevant influence from the front propellers.

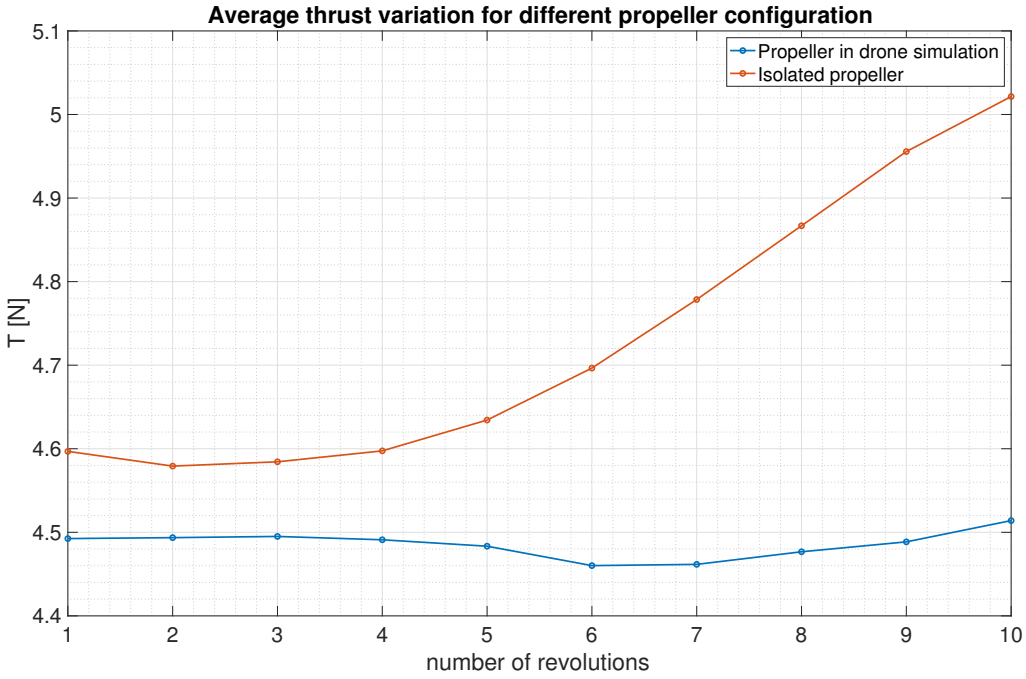

Figure 7.13: Average thrust comparison between single propeller and drone. The comparison is has been made for the accelerating propeller.

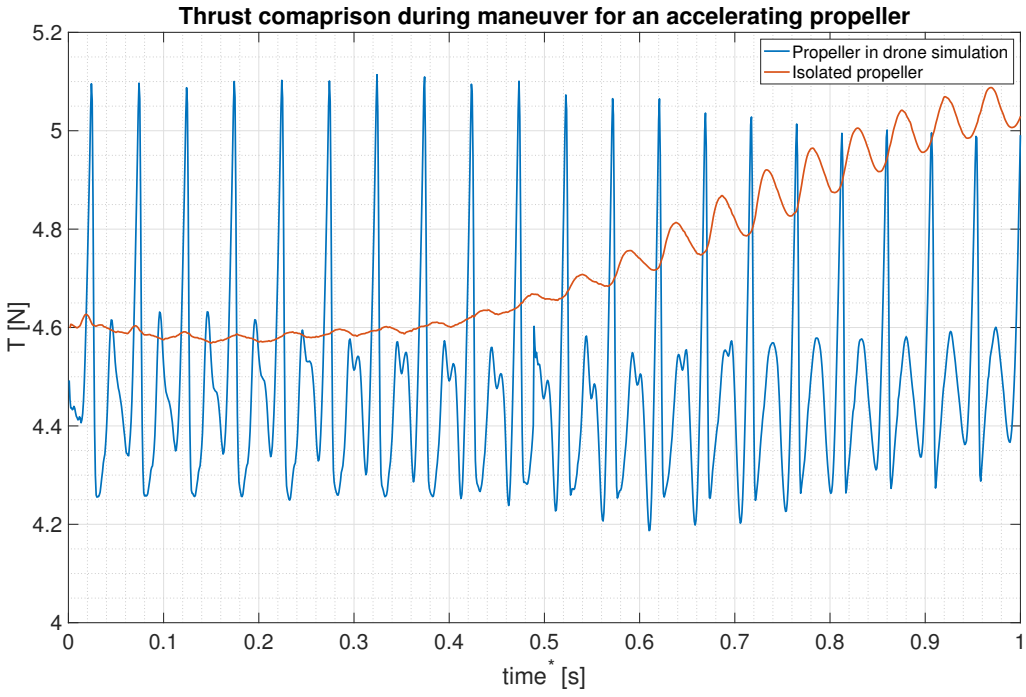

Figure 7.14: Thrust history comparison between single propeller and drone. The comparison is has been made for the accelerating propeller.

8

Aeroacoustics methodology

In this chapter, it will be described the methodology adopted for the aeroacoustic analysis of the maneuvering drone. As for the fluid dynamic part, we started studying the isolated propeller as a validation of the methodology that later has been applied to the drone itself. Due to time limitations, it has been possible to apply the methodology only to the isolated propeller. Therefore, the study of the maneuvering drone has been left for the future.
Usually, when solving aeroacoustic equations there are two possible approaches. One in the time domain and the other in the frequency domain. For this problem, it has been used the first one. In this chapter, there will be a description of the method used as well as the reasons for this choice. Moreover, there will be a discussion on the results obtained.

8.1 Time domain approach

The resolution of FW-H equations in the time domain has been done using Starccm+. The use of this approach is justified by the nature of the problem. Indeed, the propeller is undergoing a maneuver during which there is an unsteady variation of the loads, a change in RPM, and also the variation of the relative distance between the propeller and the microphone. All these aspects could be a source of problems during an FFT transformation [29]. Therefore, the time domain solution seemed to be the most solid. However, this approach needed complete validation since it has never been used at VKI.

8.1.1 Solution set-up

To use the aeroacoustic solver in Starccm+ it is necessary to define two different items:

1. The surface over which the solver had to obtain the acoustic pressure. This surface could be defined either as impermeable or permeable.

2. The microphone position.

To understand the choice of the surface it is better to explain the mathematical formulation of FW-H equations. The Ffowcs Williams-Hawkings (FW-H) formulation is based on Farassat's Formulation 1A and the Dunn Farassat Padula Formulation 1A. In these formulations it is possible to have both permeable and impermeable surfaces. The permeable surface coincides with the rigid body surface. Therefore, in this case, the software is solving the FW-H equations using all the variables values on the surface of the propeller. On the other hand, the use of the impermeable surface consists in choosing a surface that is enclosing the propeller (for example a cylinder), and the equations are solved considering pressure values on this surface. These two approaches come with their advantages and disadvantages. They can be briefly summarized in this way:

1. The use of a permeable surface guarantees the solution of all acoustic effects in the surface chosen. In the case of the drone, it could be useful to account also for the scattering effects [39]. For the single propeller, this advantage is less relevant. However, the main limit is related to the treatment of the wake. Indeed, the choice of a permeable surface is fundamental. If this surface is interacting with the wake, this will lead to a non-full description of the acoustic behavior. Therefore, to avoid this problem it is possible to choose geometries that are enclosing the whole region (propeller plus wake). Thus increasing the computational demand [40]. The use of such surfaces is widely spread for applications where transonic effects are present and need to be accounted for [40].

2. On the other hand, the use of the impermeable surface does not allow to solve for scattering effects. However, the computational cost is less demanding [40]. Therefore, this was the chosen approach. In addition to that, in our case the Mach number indicates a completely subsonic flow field.

Once the surface has been chosen, it was necessary to define the position of microphones. In order to better understand this it is useful to consider Figure 8.1:

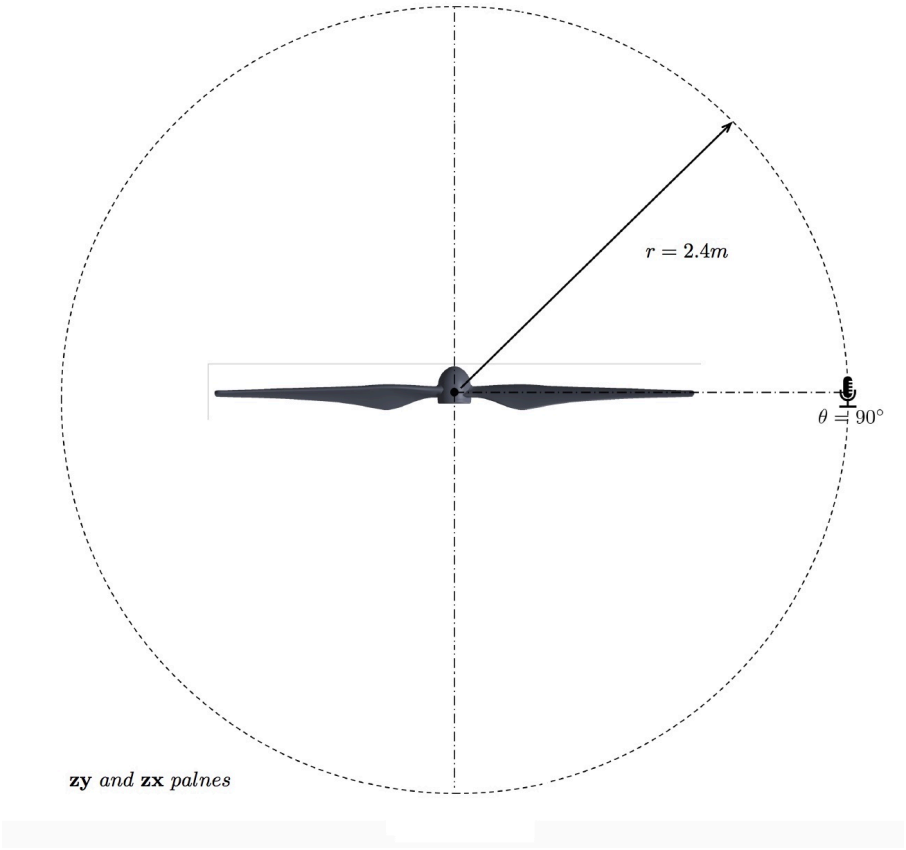

Figure 8.1: Microphone position.

The radius has been chosen to be 2.4 m because in this way the microphone is in the far-filed during the whole maneuver. Moreover, similar distances has been used in [3] and [4]. In this way at the end of the maneuver the radius is approximately 1.2 m.

8.2 Time domain results

Once the acoustic pressure at the microphone's location was obtained from Starccm+ it was possible to post-process it in order to obtain some useful quantity for the acoustic analysis. The quantity used is the SPL which is defined as:

$$SPL = 20log_{10}\left(\frac{p'_{rms}}{p_{ref}}\right) \tag{8.1}$$

where p_{ref} is chosen to be $2 \cdot 10^6$ Pa and p'_{rms} is the root mean square acoustic pressure computed from the microphone measurement in Starccm+ [3]. In order to obtain p'_{rms} it was necessary to move into the frequency domain. Therefore, it was defined the dimension "sub-step" which was the number of propeller complete rotations. This has been done in order to divide the total maneuver into a number of sub rotations. Indeed, when moving to the frequency domain it is necessary to define the period of time over which apply the transformation. Therefore, it was used the period of each sub-step. For this case it was used the pwelch function in order to move into the frequency domain. As mentioned in Chapter 2 when analyzing the tonal noise it is expected to have some peaks in the BPF multiples.

A relevant note has to be done at this point. Indeed, in the solution of FW-H equations there are no hypotheses concerning the maneuver. This means that the maneuver has not been discretized and therefore considered as a sum of different quasi-steady simulations. The flow field and the acoustic solution are applied to the actual maneuver implemented in Starccm+. Therefore, this methodology allows us to obtain a pressure in time domain solution which is the real one. On the other hand, if using a frequency domain analysis, it would have been necessary to make some additional hypotheses in the maneuver definition.

The first relevant validation step is the comparison of these acoustic results coming from the time approach for the first files (almost in hovering condition) to the proper hovering configuration studied by [3] and the experimental results. It is important to notice that the solution found in [3] is based on a frequency domain analysis. From Figure 8.2 it is possible to see that there is a very good match for the first 2 BPFs (lower than 3.5 dB) considering all the different methods. However, for higher frequencies, there is a larger difference in SPL values. This behavior has already been noticed in [3] and it seems to be related to the nature of uRANS [3].

Now it can be analyzed the variation of the SPL values for the different BPFs during the maneuver. From these two figures it is possible to distinguish several effects:

1. The decrease in BPF values. Indeed, since the propeller is decreasing its rotational speed, it is expected a decrease in the value of BPF [4]. The first BPF at the end of the maneuver is expected to be at 182 Hz which is the value obtained. This

Figure 8.2: Validation of the hovering configuration for the isolated propeller.

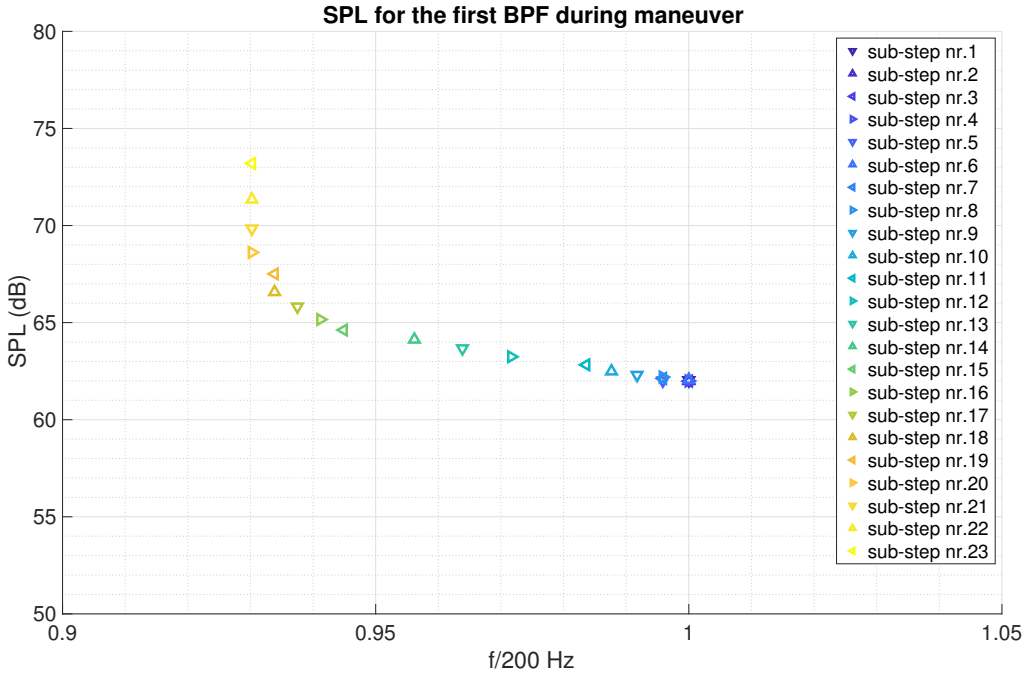

Figure 8.3: SPL variation for the first BPF during the single propeller maneuver for the microphone in front of the propeller.

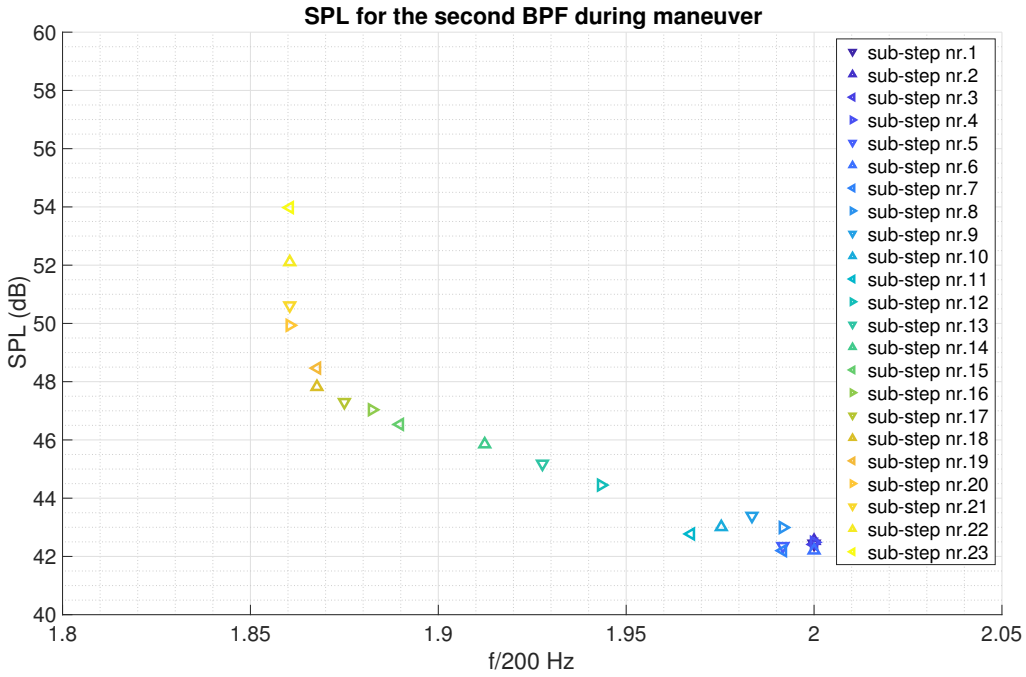

Figure 8.4: SPL variation for the second BPF during the single propeller maneuver for the microphone in front of the propeller.

behavior is happening for all the BPFs. In the case of an accelerating propeller the BPFs values are expected to increase.

2. An increase in the values of SPL. While all the considerations at the previous point are direct consequences of the BPF definition. In this case, any analysis is much more difficult. In the literature review, there has been a detailed explanation regarding the effects of RPM, flow stream velocity, and tilt on noise. However, as explained in [4] these have not been studied during a maneuver. Therefore, it cannot be applied directly to our case. However, the work done in [4] is useful to understand which are the most important effects during the study of a maneuvering propeller. In particular, it looks like the effect of velocity increase and reduction of distance from the microphone is dominant with respect to the effects coming from the increase of tilt angle and RPM reduction.

In Starccm+ when solving FW-H equations it is possible to account both for load noise and thickness noise. Since the Mach number in this application is < 0.3 it is expected to observe a dominance of load noise with respect to the thickness one [1]. In Figure 8.5 is reported the effect of thickness noise in the SPL.

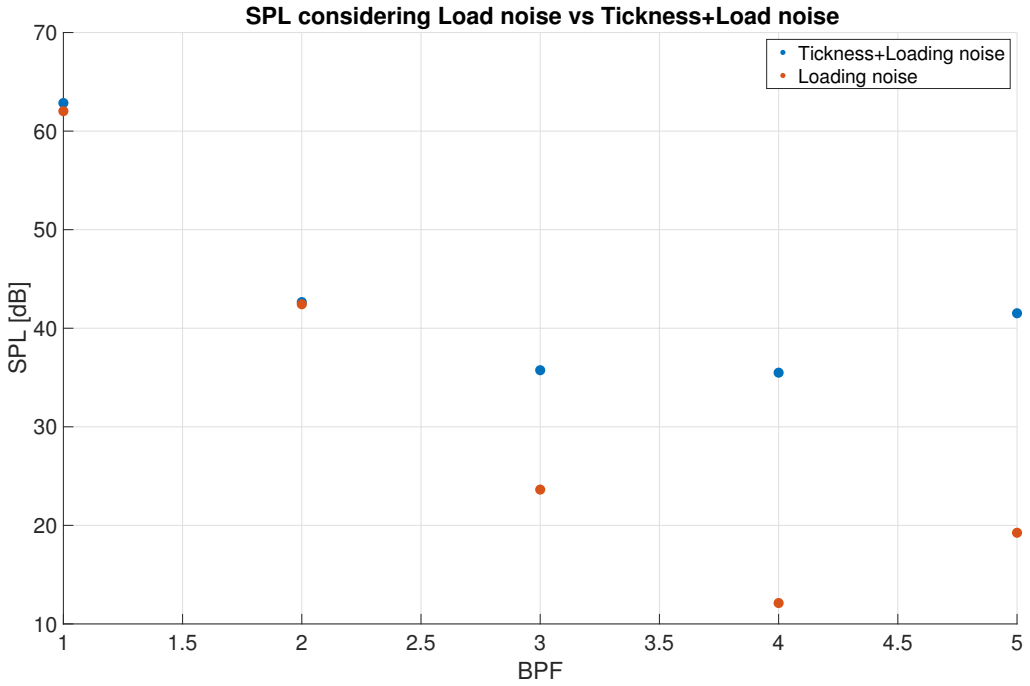

Figure 8.5: SPL difference in the isolated propeller considering considering only loading noise vs thickness plus loading noise.

From this figure, it is clear that the effect is completely negligible for the first two BPFs. On the other hand, it is quite relevant for higher frequencies.

During the post process of these data, it was found an unexpected phenomenon. Indeed, when analyzing the SPL values it was found that for low frequency (half of the first BPF) there was a peak in SPL levels. This phenomenon can be observed in Figure 8.6 From this figure it is clear that the peak of SPL is changing its frequency as the BPF changes.

Moreover, it has been found a relation between the frequency location of this peak and the number of sub-steps used. This relation is the following:

$$freq_{peak} = \frac{propeller\ rotational\ frequency}{number\ of\ roataions\ per\ sub-step} \tag{8.2}$$

During hovering the propeller rotational frequency is 100 Hz. The number of rotations per sub-step used in this case are two, thus the peak is expected to be at 50 Hz. This relation may suggest that these peaks at lower frequencies are related to the post-processing

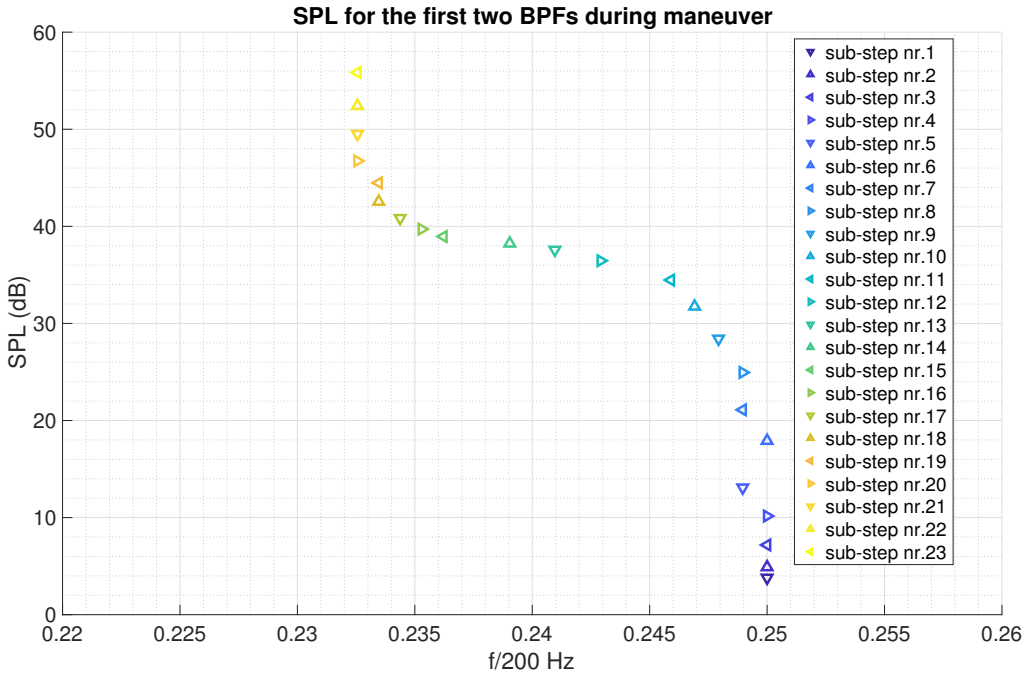

Figure 8.6: SPL at lower frequency for the isolated propeller.

process. The values of SPL reached are very high as the maneuver proceed. However, at the moment we do not have an explanation for these peaks. A more detailed study is needed in order to understand this behavior.

9

Conclusions and Future work

In recent years it has been possible to witness an increasing interest in the use of drones and other UAVs vehicles. They have been employed in the cinema industry, commerce purposes, leisure activities, search and rescue missions. Although their unique abilities such as vertical take-off and high maneuverability guarantee enormous success in these fields of application, there are still some problems that need to be understood and thus solved. The main one is probably the aeroacoustic noise generated by these devices.
Enormous efforts have been applied to the study of noise generated during hovering and forward flight maneuvers. However, it is well established that the noise generated during maneuvers is of enormous concern [11]. Therefore, in this thesis, it has been developed a methodology that has been proven to work for the study of the aeroacoustic of a maneuvering drone.

9.1 Conclusions

In the methodology definition, it has been fundamental the use of the overset mesh approach. This way of creating a mesh has been used for similar applications and has a robust implementation in Starccm+. A relevant amount of time has been invested in understanding this approach, its leading principles, and settings in order to be applied to the case of a maneuvering drone. Another fundamental aspect of this thesis was the maneu-

ver definition. Indeed, it has been defined as a possible maneuver based on some data available at the VKI. Finally, this methodology has been tested and validated with an increasing level of difficulty. Starting from an isolated drone and finishing with a complete drone case. The aerodynamic characterization of both the isolated propeller and the complete drone has obtained interesting results:

1. For the isolated drone it was possible to obtain the thrust history and compare its variation to a very simple analytical model;
2. In the case of a complete drone it was analyzed the thrust variation during a maneuver and studied the difference with the isolated propeller in the case of accelerating or decelerating propellers;
3. Finally, from a computational point of view it was interesting to observe that this overset method is more demanding than the sliding mesh approach.

After the validation of the aerodynamic part of the problem, it was possible to define a methodology for the acoustic part of the thesis. Unfortunately, it has been possible to study only the isolated propeller due to time constraints. It has been used a time domain solution for FW-H equations because of the unsteady nature of the problem. In the solution, it has been applied a permeable surface for the definition of the propeller source and it was possible to observe:

1. A correct variation of BPF due to the reduction in RPM;
2. An increase of SPL values as the propeller is performing the maneuver from hovering to forward flight and it is approaching the microphone.

9.2 Future work

In order to complete the work done in this thesis it would be interesting to proceed in the following directions:

1. Extend the aeroacoustic analysis to the drone configuration;
2. Understand if it is meaningful to use a frequency domain solution;
3. Define in a proper way the maneuver with the help of experimental data;

4. Use the analytical model as input to an acoustic solution. Since that model seems to predict the thrust variation with a moderate error (in the order of 10 %) with respect to the computational time and resources needed;

5. Simulate more complex maneuvers such as the passage from forward flight to hovering;

10 Appendix

10.1 Analytical model

In this Appendix it will be described in detail the method used in the analytical 2D solution. It will be provided all the input files and data used in the process of the analytical methodology. Firstly, there will be the presentation of the profiles used. It will be followed by all the input and parameters used in Xfoil and finally it will be reported the Cl and Cd values for all the profiles.

10.1.1 Airfoil profiles

In order to perform the aerodynamic simulation it was necessary to obtain the airfoil profiles for the blade that was used in the thesis. This was obtained cutting the 3D geometry of the blade and they were later prepared to be used by Xfoil. Indeed, this solver needed a specific input order for the airfoil points. Here the airfoil profiles will be given.

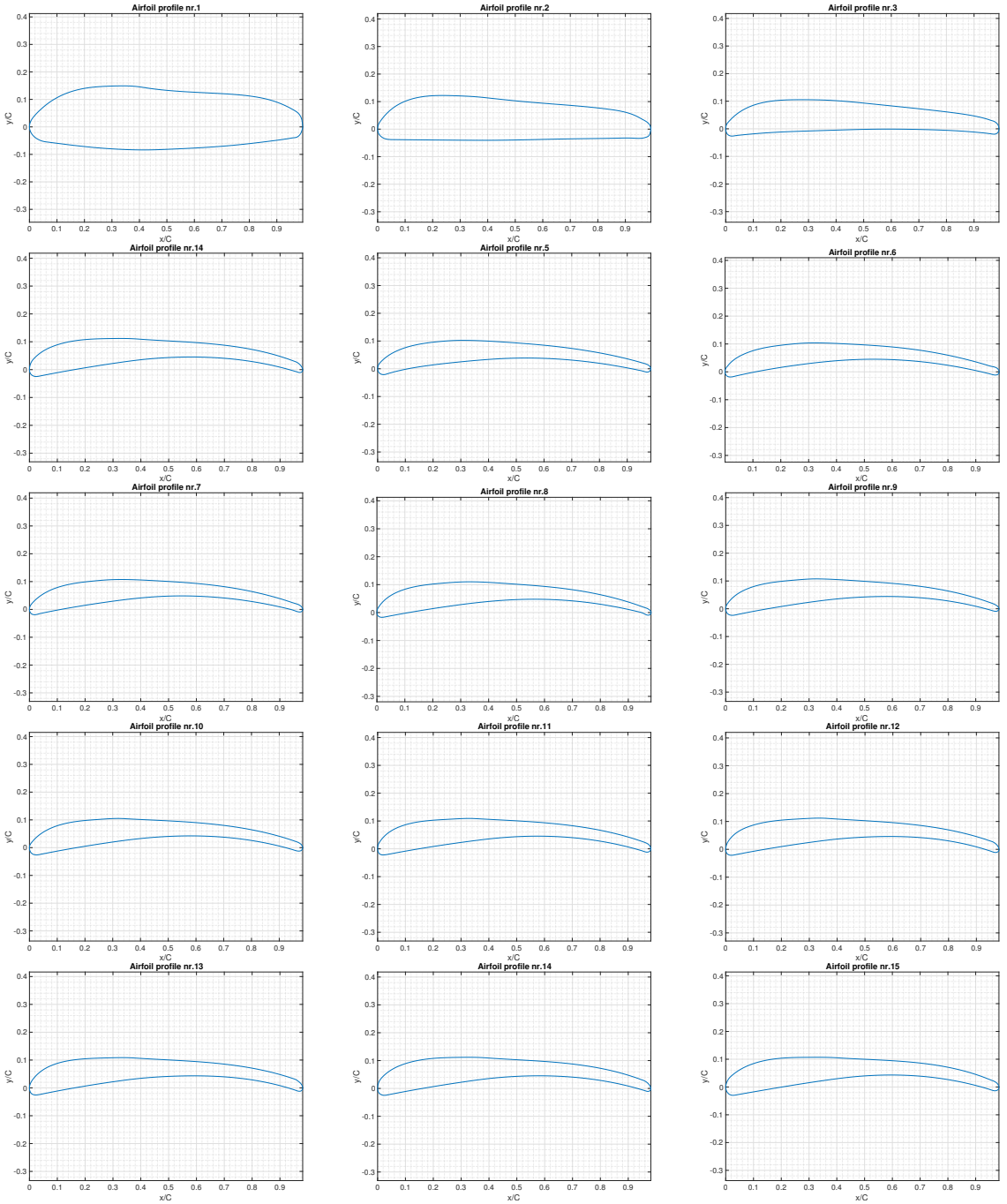
Airfoil profile nr.1
Airfoil profile nr.2
Airfoil profile nr.3
Airfoil profile nr.14
Airfoil profile nr.5
Airfoil profile nr.6
Airfoil profile nr.7
Airfoil profile nr.8
Airfoil profile nr.9
Airfoil profile nr.10
Airfoil profile nr.11
Airfoil profile nr.12
Airfoil profile nr.13
Airfoil profile nr.14
Airfoil profile nr.15
y/C
x/C

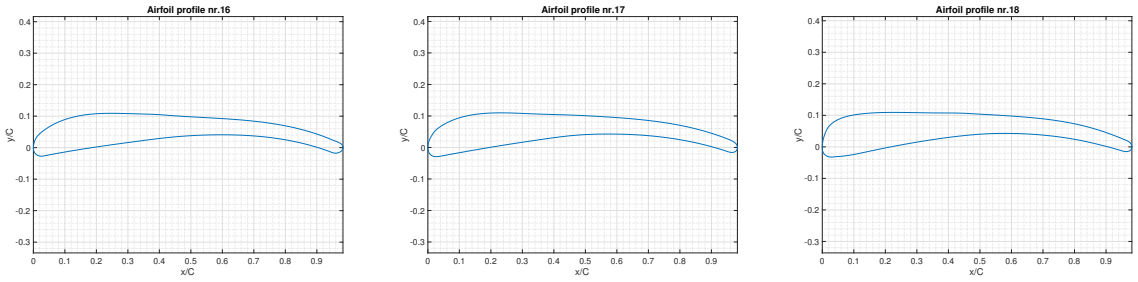

Figure 10.1: Airfoil images of the DJI propeller.

From these images it is clear that at the Trailing Edge (TE) there could be some problems related to the Kutta conditions. Thus, it could interfere with the convergence of the solver in Xfoil. Therefore, in order to overcome this problem it has been applied a technique that has already been used by my supervisor. It consisted in removing some points (20) at the TE. In this way the remaining surface could be more suited for the Kutta condition. It is noteworthy that the overall number of points is in the order of 7 hundreds. Therefore 30 points represent 4 % of the overall number of points.

10.1.2 Xfoil settings and inputs

In Xfoil it has been adopted the following settings:

1. number of panels : 500;
2. viscid mode. Therefore, it was necessary to define both Mach number and Reynolds number. These values will be provided later;
3. number of maximum iterations: 500;

The Mach number and Reynolds number have been computed considering the hovering configuration. This has been done for two main reasons:

1. Firstly, these variations where often very limited thus the effect on Cd and Cl was limited;
2. Second, the aim was to keep the model as simple as possible. Therefore, it was not worth the effort of computing the Cl for each time step varying both Re and Ma.

Re $[\cdot 10^5]$	1.4	2.1	3.2	4.5	5.7	6.3	6.3	6.3	6.4	6.5	6.5	6.5	6.4	6.3	6.2	6.0	6.0	6.0
Ma $[\cdot 10^{-1}]$	0.2	0.3	0.4	0.5	0.7	0.8	0.9	1.0	1.1	1.2	1.3	1.4	1.6	1.7	1.8	1.9	1.0	2.1

Table 10.1: Re and Ma numbers for each blade profile.

In Xfoil it has been computed both Cd and Cl for the airfoils provided. Thus, it is noteworthy to show the results obtained:

Cl	0.28	0.44	0.59	0.63	0.74	0.86	0.96	1.01	0.99	0.92	0.95	1.09	1.08	1.08	0.99	0.95	1.0	0.96
Cd	0.02	0.02	0.02	0.02	0.02	0.01	0.01	0.01	0.01	0.01	0.02	0.01	0.01	0.01	0.01	0.01	0.01	0.01

Table 10.2: Cd and Cl values for each blade profile.

These are the values used in the Lift computation and therefore in the Thrust definition.

References

[1] S. Glegg and W. Devenport, *Aeroacoustics of Low Mach Number Flows*. Academic Press, 2017.

[2] M. Carlsson, L. Davidson, S.-H. Peng, and S. Arvidson, "Turbulence injection methods at rans-les interfaces or inlets for scale-resolving simulations," 2022.

[3] A. Zarri, E. Dell'Erba, W. Munters, and C. Schram, "Aeroacoustic installation effects in multi-rotorcraft: Numerical investigations of a small-size drone model," *Aerospace Science and Technology*, vol. 128, 2022.

[4] N. S. Jamaluddin, A. Celik, K. Baskaran, D. Rezgui, and M. Azarpeyvand, "Aerodynamic and aeroacoustic characterisation of isolated rotor in hover and transition to forward flight," *AIAA AVIATION 2021 FORUM*, 2021.

[5] Y. Yang, Y. Liu, Y. Li, Y. Wang, B. Huang, and W. Li, "Aerodynamic and aeroacoustic characteristics of a multicopter propeller during forward flight," *AIAA Propulsion and Energy Forum*, 2018.

[6] S. A. H. Mohsan, M. A. Khan, F. Noor, I. Ullah, and M. H. Alsharif, "Towards the unmanned aerial vehicles (uavs). a comprehensive review," *Drones*, 2022.

[7] U. S. D. of Transportation, "Integration of civil unmanned aircraft systems (uas) in the national airspace system (nas) roadmap." 2013.

[8] C. Courtin and M. J. Burton, "Feasibility study of short takeoff and landing urban air mobility vehicles using geometric programming," *American Institute of Aeronautics and Astronautics*, 2018.

[9] O. Gur and A. Rosen, "Optimizing electric propulsion systems for unmanned aerial vehicles," *Journal of Aircraft*, 2009.

[10] M. Cherney, "Delivery drones cheer shoppers, annoy neighbors, scare dogs," *Wall Street Journal*, 2018.

[11] E. Gallo, G. Beaulieu, and C. F. Schram, "Annoyance factors of a maneuvering multicopter drone," *28th AIAA/CEAS Aeroacoustics 2022 Conference*.

[12] J. F. C. M. and O. D. L. M., "Simulation and validation of the aerodynamic performance of a quadcopter in hover condition using overset mesh," *AIAA*, 2019.

[13] L. Mejia, Omar, Mejia, Oscar, Escorcia, Karol, Suarez, Fabian, Lain, and Santiago, "Comparison of sliding and overset mesh techniques in the simulation of a vertical axis turbine for hydrokinetic applications," *Processes*, vol. 9, p. 1933, 10 2021.

[14] M. Jarkowski, M. A. Woodgate, G. N. Barakos, and J. Rokicki, "Towards consistent hybrid overset mesh methods for rotorcraft cfd," *INTERNATIONAL JOURNAL FOR NUMERICAL METHODS IN FLUIDS*, 2013.

[15] J. Maunus, S. M. Grace, , and D. L. Sondak‡, "Effect of rotor wake structure on fan interaction tone noise," *AIAA JOURNAL*, 2012.

[16] J. de Laborderie, L. Soulat, and S. Moreau‡, "Prediction of noise sources in axial compressor from urans simulation," *JOURNAL OF PROPULSION AND POWER*.

[17] S. Boij, "The influence of flow coupling on sound propagation in flow ducts," *Proceedings of the Tenth International Congress on Sound and Vibration*, 2003.

[18] N. Curle, *The influence of solid boundaries upon aerodynamic sound*. Proc. R. Soc. Lond. A Math. Phys. Sci., 1955.

[19] P. Doak, *Acoustic radiation froma turbulent fluid containing foreign bodies*. Proc. R. Soc. Lond. A Math. Phys. Sci., 1960.

[20] P. Candeloro, T. Pagliaroli, D. Ragni, and S. D. Francesco, "Small-scale rotor aeroacoustics for drone propulsion: A review of noise sources and control strategies," *Fluids*, 2022.

[21] F. Mendonça, R. Allen, J. de Charentenay, and D. Kirkham, "Cfd prediction of narrowband and broadband cavity acoustics at m=0.85," *AIAA*, 2003.

[22] F. Farassat, "Linear acoustic formulas for calculating rotor blade noise," *AIAA J.*, 2981.

[23] M. Roger and K. Kucukcoskun, "Near-and-far field modeling of advanced tail-rotor noise using source-mode expansions," *Journal of Sound and Vibration*, 2019.

[24] C. L..MORFEY, "Rotating pressure patterns in ducts: Their generation and transmission," *J. Sound Vib*, 1964.

[25] D. S.-K. Ting, *Basics of Engineering Turbulence*. U.K: Academic Press is an imprint of Elsevier, 2016.

[26] S. Pope and P. Eccles, *Turbulent Flows*. Cambridge University Press, 2000.

[27] D. D. Zawodny, Nikolas S.; Boyd, "Investigation of rotor–airframe interaction noise as-sociated with small-scale rotary-wing unmanned aircraft systems," *Journal of the American Helicopter Society*, 2020.

[28] R. de Vries, N. van Arnhem, T. Sinnige, R. Vos, and L. L. Veldhuis, "Aerodynamic interaction between propellers of a distributed-propulsion system in forward flight," *Aerospace Science and Technology*, vol. 118, 2021.

[29] G. Brès, K. Brentner, G. Perez, and H. Jones, "Maneuvering rotorcraft noise prediction," *Journal of Sound and Vibration*, vol. 275, pp. 719–738, 08 2004.

[30] Nathanael, J. C. Wang, J. C. Hung, and L. K. Huat, "Preliminary investigation of wake vortex generated by spinning quadrotor propellers using overset mesh," *American Institute of Aeronautics and Astronautics*, 2021.

[31] S. D. I. Software, "Starccm+ user guide. 2023," 2023.

[32] O. D. Lopez Mejia, O. E. Mejia, K. M. Escorcia, F. Suarez, and S. Laín, "Comparison of sliding and overset mesh techniques in the simulation of a vertical axis turbine for hydrokinetic applications," *Processes*, vol. 9, no. 11, 2021. [Online]. Available: https://www.mdpi.com/2227-9717/9/11/1933

[33] R. W. Deters, S. Kleinke, and M. S. Selig., "Static testing of propulsion elements for small multirotor unmanned aerial vehicles," *American Institute of Aeronautics and Astronautics*, vol. 9, p. 1933, June 2017.

[34] A. Berton, F. D'Orrico, and M. Sideri, "Overset grids for fluid dynamics analysis of internal combustion engines," *Energy Procedia*, vol. 126, pp. 979–986, 2017,

aTI 2017 - 72nd Conference of the Italian Thermal Machines Engineering Association. [Online]. Available: https://www.sciencedirect.com/science/article/pii/S1876610217337463

[35] Z. Zhang, C. Xie, W. Wang, and C. An, "An experimental and numerical evaluation of the aerodynamic performance of a uav propeller considering pitch motion," *Drones*, vol. 7, no. 7, 2023. [Online]. Available: https://www.mdpi.com/2504-446X/7/7/447

[36] Z. Zhang, C. Xie, K. Huang, and C. Yang, "Influence of aerodynamic interaction on performance of contrarotating propeller/wing system," *Aerospace*, 2022.

[37] NASA. Advanced air mobility: The science behind quadcopters reader student guide. [Online]. Available: https://www.nasa.gov/sites/default/files/atoms/files/aam-science-behind-quadcopters-reader-student-guide_0.pdf

[38] M. Misiorowski, F. Gandhi, and A. A. Oberai, "Computational study on rotor interactional effects for a quadcopter in edgewise flight," *AIAA*, 2019.

[39] D. Lockard and J. Casper, "Permeable surface corrections for ffowcs williams and hawkings integrals," *Collection of Technical Papers - 11th AIAA/CEAS Aeroacoustics Conference*, vol. 4, 05 2005.

[40] A. S. Morgans and A. P. Dowling, "The aeroacoustics of transonic helicopter blades," *AIAA*, 2002.

Acknowledgments

With this thesis, I mark the completion of one of the first and most significant steps in my professional journey. Throughout my Master's degree at the University of Padova, I had the privilege to deepen my academic knowledge of aeronautical engineering and cultivate essential skills for the professional career.
Countless people and experiences have left a lasting impression on me during this period, and though I can only mention a few, their impact is profound. I'll begin by expressing my deep gratitude to the THRUST team. With them, I shared unique experiences, acquired invaluable skills, and forged some wonderful friendships.
Moving chronologically, I am immensely thankful to all the professors who guided me along this exciting path. A special mention goes to Professor De Vanna Francesco for his unwavering support during my thesis and his course at the University.
A significant part of my journey was shaped by the von Karman Institute for Fluid Dynamics, and for that, I extend my sincere thanks. I am grateful to Prof. Schram for granting me the opportunity to study and work with the aeroacoustics team at VKI. Moreover, my sincere appreciation goes out to my advisor, Alessandro Zarri. His constant presence during my internship, along with his vast knowledge in fluid dynamics and aerocoustics, has been invaluable. I must also acknowledge Julien Christoph for his assistance and contributions. During this enriching experience, I had the pleasure of meeting incredible STP students with whom I shared unforgettable moments that will forever be cherished.
Last but not least, I want to express my gratitude to everyone who supported me throughout this journey - my girlfriend, family, and friends. Your encouragement and belief in me have been a constant source of strength.
As I conclude this chapter, I carry with me not only newfound knowledge but also a heart full of appreciation for everyone who played a role in my growth and success. Thank you all.